


Review

A Review of Third Generation Solar Cells

N. Shah ¹, A. A. Shah ^{1,*}, P. K. Leung ¹, S. Khan ² , K. Sun ¹, X. Zhu ¹ and Q. Liao ¹

¹ MOE Key Laboratory of Low-Grade Energy Utilization Technologies and Systems, Chongqing University, Chongqing 400030, China

² Department of Electrical Engineering, City University of Science and Information Technology, Peshawar 25000, KPK, Pakistan

* Correspondence: akeelshah@cqu.edu.cn

Abstract: Third-generation solar cells are designed to achieve high power-conversion efficiency while being low-cost to produce. These solar cells have the ability to surpass the Shockley–Queisser limit. This review focuses on different types of third-generation solar cells such as dye-sensitized solar cells, Perovskite-based cells, organic photovoltaics, quantum dot solar cells, and tandem solar cells, a stacked form of different materials utilizing a maximum solar spectrum to achieve high power conversion efficiency. Apart from these solar cells, other third-generation technologies are also discussed, including up-conversion, down-conversion, hot-carrier, and multiple exciton. This review provides an overview of the previous work in the field, alongside an introduction to the technologies, including their working principles and components. Advancements made in the different components and improvements in performance parameters such as the fill factor, open circuit voltage, conversion efficiency, and short-circuit current density are discussed. We also highlight the hurdles preventing these technologies from reaching commercialization.

Keywords: Shockley–Queisser limit; third generation; Perovskite; dye-sensitized; quantum dot; tandem solar cells; organic photovoltaics



Citation: Shah, N.; Shah, A.A.; Leung, P.K.; Khan, S.; Sun, K.; Zhu, X.; Liao, Q. A Review of Third Generation Solar Cells. *Processes* **2023**, *11*, 1852. <https://doi.org/10.3390/pr11061852>

Academic Editor: Ioannis Spanopoulos

Received: 25 March 2023

Revised: 25 April 2023

Accepted: 28 April 2023

Published: 20 June 2023



Copyright: © 2023 by the authors. Licensee MDPI, Basel, Switzerland. This article is an open access article distributed under the terms and conditions of the Creative Commons Attribution (CC BY) license (<https://creativecommons.org/licenses/by/4.0/>).

1. Introduction

To fulfill future energy needs, while reducing the reliance on fossil fuels [1], there has been a concerted effort worldwide to advance sustainable and clean energy resources [2]. Since it is abundant and clean, solar energy is seen as a significant fuel source for the production of electrical power [3]. Solar cells (SC), often called photovoltaic (PV) cells, use the PV effect to convert light energy into electricity and are considered one of the most significant environmentally friendly power sources, along with hydropower and wind/tidal power. PV technologies have been consistently evolving over the last two decades to improve the power conversion efficiencies (PCE) of solar cells [4].

SCs can be divided into different categories in terms of the timeline of their development as well as the materials they use. A broad categorization is as follows:

(1) First generation, which are of silicon (Si) type and are the most efficient [5], though decrease in efficiency as the temperature increases.

(2) Second generation, which are of thin film type, are cheaper than the Si type, and are already commercially available [6,7]

(3) Third generation, which are semiconducting-based solution-processed PV technologies [8,9].

According to Green [10], third-generation solar cells are defined as those capable of high power-conversion efficiency while maintaining a low cost of production. Their implementation with thin-film technologies could have a huge impact economically, making solar energy one of the most accessible and cheapest options for future energy production. Thin-film technologies have the benefit of a tunable bandgap, making them a better option for light harvesting. This innovation is seen as a possible game changer in PV technologies

since it would not only achieve improved device performance but also lower fabrication costs and extended device lifetimes [11–13]. As a result, third-generation solar cells such as dye-sensitized solar cells (DSSCs) [14], perovskite solar cells (PSC) [15–17], and quantum dot sensitized solar cells (QDSSCs) [18,19] are being widely explored and undergoing rapid development. In addition to these technologies, third-generation SCs also include organic photovoltaics (OPVs), up-conversion, down-conversion, hot-carrier, and multiple exciton cells.

Traditional Si-based solar cells achieved high efficiencies at high cost, which is what led to the introduction of third generation or emerging technologies, with flexible manufacturing techniques, low weights, low costs, and excellent efficiencies [10,20]. Organic solar cells have not yet been commercialized due to their lack of stability, and researchers are making efforts to increase the efficiency and stability of these solar cells through tandem solar cell architectures [21]. The sun provides a limitless source of energy, but solar cells need to be made with the best band gap possible to maximize the harvesting of energy from the solar spectrum [22]. Photon absorption and energy generation differ in silicon and organic solar cells, and Si has a lower exciton-binding energy. Organic solar cells generate a photocurrent at a greater rate due to multiple exciton production, which ultimately raises the fill factor and efficiency of solar cells [23].

After going through numerous improvement phases, DSSC technologies have achieved 14.2% PEC in 2020 [14], which was surpassed in 2022 by Ren et al. [24] who reported a figure of 15.2%. The first ever perovskite material-based solar cell had an efficiency of 3.8%, introduced by Kojima et al. [25] in 2009. After extensive research efforts, the latest recorded PCE of 25.7% was achieved by Ulsan National Institute of Science and Technology (UNIST)¹. The latest recorded efficiencies of QDSSC, TSC, and OPVs are 18.1% (UNIST), 32.5% by Helmholtz-Zentrum Berlin (HZB), and 19.2% [26], respectively (all of these value and others are available from <https://www.nrel.gov/pv/cell-efficiency.html> (accessed on 9 January 2023)).

Even though these technologies are showing promise, they still need to overcome some major limitations before mass production/commercialization can become a reality. Commercialization of these third-generation solar cells is limited by performance stability under different operational temperatures, module design, processing procedure, and the use of toxic materials [27]. In DSSC, substrates are often made of plastic and have a low thermal processing limit. Low-temperature processing with plastic substrates reduces semiconductor film adherence to the substrate and leads to poor electrical contact between semiconductor particles. Plastic-based DSSC technologies present a significant challenge in terms of device stability due to oxygen and moisture input from porous and permeable plastic substrates. PSCs have high PCEs compared to the other third-generation solar cells but are limited by the instability of the perovskite layer under high humidity conditions, lowering their lifespans and limiting their usage for outdoor applications [28].

QDSSCs have low PCEs and also suffer from instabilities associated with the different device components, such as the anode electrolyte and counter electrode [29]. The photoactive layers of OPV devices are processed from halogenated solvents such as dichlorobenzene and chlorobenzene [30]. As a result of their release into the air, these halogenated solvents will cause significant harm to the environment. Their volatilization during production of the device is also dangerous and may cause cancer. Therefore, it is necessary to replace these harmful halogenated solvents with environmentally friendly alternatives.

Review articles on third-generation solar cell technologies such as dye-sensitized, perovskite, quantum dot, tandem solar cells, and organic photovoltaics exist individually. However, we are not aware of any review that systematically explains and presents detailed information regarding the recent progress made in all of these technologies together. This review aims to provide a detailed study of different third-generation solar cells, namely DSSCs, PSCs, QDSSCs, tandem solar cells (TSC), OPVs, as well as other technologies such as up-conversion, down-conversion, hot-carrier, and multiple-exciton. It considerably

expands on previous reviews, in order to better grasp the operational methods, approaches, and recent improvements.

We discuss the working principles and different components, as well as the advances made in these components. Improvements in the different performance parameters through these advancements are detailed, including in the fill factor, open circuit voltage, conversion efficiency, and short-circuit current density. Hurdles and challenges facing these technologies in terms of reaching the market are highlighted for completeness. In contrast to previous reviews, all of the main third-generation technologies, their components, and open challenges are included in a single review. We point out that other generation technologies are not covered in this review since coverage of the third generation is already very broad. The review is divided into different sections according to a categorization of the technologies. Section 1 provides an introduction to PV technology and the basic parameters of SC, along with a discussion on the PV electricity market.

Section 2 introduces DSSCs, explains their working principles, different components, and challenges in terms of commercialization. Moreover, improvements in their efficiency using a number of techniques are discussed. In Section 3, PSCs are introduced, together with perovskite material properties, PSC structures, well-known film fabrication techniques, techniques for efficiency improvement, and challenges facing commercialization. In Section 4 on quantum dot solar cells (QDSC), the working mechanism of the QDSSC is explained, and factors affecting its stability are discussed, along with progress in terms of efficiency using different types of photoanodes and QD sensitizers. Application of QD technology in PSCs and challenges for QDSSC technology are also mentioned. The potential of TSC technology and Perovskite/Si-based TSC are explored in Section 5. In Section 6, the working mechanisms of OPVs, their main components, and challenges for these technologies are highlighted and discussed. In Section 7, we briefly review other third generation technologies, and in Section 8, we provide conclusions.

1.1. Basic SC Parameters

The performance of SCs is measured by the open circuit voltage (V_{oc}), short circuit current (J_{sc}), fill factor (FF), and power-conversion efficiency (PCE).

1.1.1. Open Circuit Voltage (V_{oc})

The maximum voltage that can be achieved from a solar cell with its terminals open, or the voltage that can be obtained from a cell with no current flowing through it [31].

1.1.2. Short Circuit Current Density (J_{sc})

When both terminals of a cell are shorted, the available amount of current, in that case, is called short circuit current. It is denoted by J_{sc} . When photons strike a solar cell and are absorbed in it, it generates an electron–hole pair (EHP) [32]. The separation of newly generated EHP takes place through the PN junction and is transmitted to the load. If this cycle is completed without recombination, the current will flow to the externally connected load.

1.1.3. Fill Factor (FF)

Fill Factor (FF) is the ratio of maximum power to the product of J_{sc} and V_{oc} . The FF of a solar cell depends on its resistive losses [33]. The FF of an ideal solar cell, having no losses, is 100%; however, achieving such value is not possible. A cell of such materials that has a high bandgap will have high FF.

1.1.4. Efficiency (PCE)

It is the ratio of output to input power. It is denoted by η [34] and can be calculated as the ratio of maximum power output P_{max} to power input P_{in} :

$$\eta = \frac{P_{max}}{P_{in}}$$

1.2. Solar Cell Electricity Market

In the last few decades, the development of solar cell power generation devices has been more rapid than was forecast [35]. The reasons for the growth are many, including aggressive policies and financial incentives, huge investments in production processes, and rapid technology development. In 2021, according to the Bloomberg NEF, 183 GW of solar photovoltaic systems (SPVs) were installed throughout the world, an increase of around 40 GW compared to the previous year. Due to this incredible growth in SPVs, experts in 2022 have revised the reports, expecting between 204 and 252 GW, and crossing the 200 GW mark for the first time in history [36] (The evolution of the efficiencies of solar cells with time is available from The National Renewable Energy Laboratory (NREL) Best research-cell efficiency chart. “<https://www.nrel.gov/pv/cell-efficiency.html> (accessed on 9 January 2023)”).

The conversion of solar energy into electrical energy via SCs has seen many developments over the last few decades. The first ever produced SC is termed a first-generation SC, achieving high efficiency with high cost. To reduce the cost of production, further improvements and materials were introduced, but the resulting efficiencies were low; such technologies are considered second-generation SCs. To obtain highly efficient and low-cost SCs, further techniques and materials were introduced, having the capacity or potential to surpass the Shockley–Queisser limit. These are termed third-generation solar cells and are the focus of this review.

A number of third-generation solar cells have indeed achieved high efficiencies at low cost. However, the stability of these SCs in different working conditions such as high humidity, high temperature, and continuous light illumination is a major challenge that has yet to be overcome. As can be seen in Figure 1 [37], one of the third-generation SCs (the perovskite SC) degrades when exposed to different relative humidity, with reduced film absorption. In only 4 h, the absorption reduces to half of its initial value, indicating a rapid degradation reaction at 98% RH. This is a major concern because solar cells will frequently have to operate in harsh environments with regularly changing weather. Thus, extensive research is required to improve the stability of these technologies.

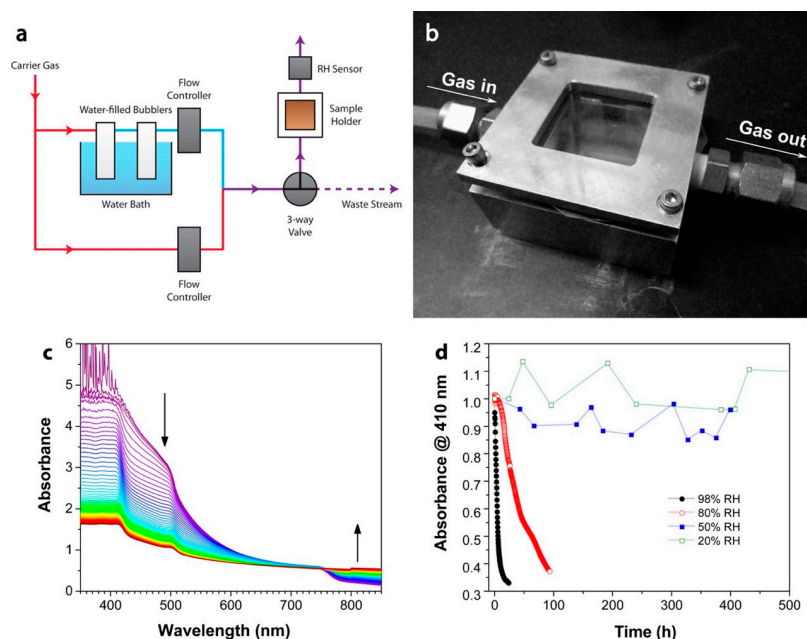


Figure 1. (a) Relative humidity control system schematic representation; (b) photo view of the sample holder; (c) $\text{CH}_3\text{NH}_3\text{PbI}_3$ in situ absorbance measurement at 98% relative humidity at 15 min time interval; (d) normalized absorbance measurements for $\text{CH}_3\text{NH}_3\text{PbI}_3$ films exposed to different relative humidity conditions [37]. Reproduced with permission from Yang et al., ACS Nano, American Chemical Society, 2015.

2. Dye-Sensitized Solar Cells

One of the most exciting technological advancements in the world of solar cells is the DSSC. It functions as a cell that mimics the method used by plant cells to produce energy. The electron moment produced by the combined influence of the photon energy and the chemical reactions is a photo-electrochemical cell [38]. The DSSC has the potential to be an energy source in the future because it is somewhat transparent and less expensive than traditional solar photovoltaics [39]. However, before claiming it to be a viable commercial product, some issues still need to be resolved. These issues and the significant advancements in DSSC technology in recent years are highlighted in this section. We provide a clear understanding of the most current upgrades made to DSSC in relation to the various components. In accordance with the various DSSC components, we divide this section into subsections and include a summary of the suggested improvements from various researchers.

The groundbreaking research on the possible uses of nano-sized TiO_2 (titanium dioxide) porous film electrodes in DSSCs was initially published by O'Regan and Gratzel [40]. The DSSC quickly developed into an active area of research since it was inexpensive and was thought to have a very high photon to electricity conversion efficiency. A significant quantity of work has since been reported.

The photoanode, sensitizer, electrolyte, and counter electrode are the essential elements of a DSSC [41,42]. The photoanode is developed using semiconductor nanostructures. On the transparent conductive glass, a variety of nanostructures, including nanorods, nanotubes, nanowires, nanocones, and nanoleaves, have been created [43]. The most effective materials for the photoanode have long been ruthenium-bipyridyl dye families such as N719, N3, and C101, which have supplanted extremely efficient solar cells [44,45]. Some researchers believe that ZnO (Zinc oxide) is the most suitable alternative for TiO_2 . According to numerous studies, the use of ZnO nanostructures for photo-electrodes can improve the photovoltaic performance of DSSCs. Some of the work involving the use of ZnO in DSSC includes the development of DSSC using the network structure of electron-spun ZnO nanofiber mats [46]; ZnO nano-sheets derived from growth mechanisms directed by surfactants [47]; the effects of annealing on the performance of DSSC using ZnO [48]; and the effects of the morphology of nanostructures of ZnO films on the efficiency of DSSCs and ZnO nanostructures for DSSC [49].

2.1. Working Mechanisms of DSSCs

Luo et al. reported 11.35% efficient DSSC, surpassing the 10.78% achieved using organic dye [50]. In 2020, Ji et al. [14] reported a 14.2% efficient cell by using an organic dye, while in 2022, Ren et al. [24] reported 15.2% efficiency using newly designed co-absorbed sensitizers, helping to harvest more sunlight. The photons excite electrons by striking the sensitizers, providing them enough energy to move from the valance band to the conduction band of a semiconductor material (TiO_2 , etc.) [51,52]. These electrons reach the flexible substrate through the porous thin semiconductor layer. The incoming light (photon) intensity and the trapping–de-trapping process can affect the flow of electrons [53]. The sensitizers regenerate the oxidized sensitizer molecules by absorbing electrons from the electrolyte (for instance, an I^-/I_3^-) in addition to oxidizing the mediators. Moreover, during the operation, the oxidized mediators at the CE (counter electrode) surface are regenerated by reduction, resulting electrons to reach the CE from an external circuit [54–56].

Chiba et al. [57] carried out studies on DSSCs by utilizing TiO_2 electrodes with varying degrees of haze. For DSSCs, it was discovered that as the haze of the TiO_2 electrodes increased, so did the efficiency in converting incident photons into a current. This was especially true in the near-infrared spectral range. By increasing the haze, a PCE of 11.1% was reached. To improve PCE, Seung et al. [58] proposed a “nanoforest” of high-density, long-branched “treelike” multigeneration hierarchical ZnO NW (nanowire) photoanodes. The increase in effectiveness is due to a large increase in the surface area, which allows for more dye loading and light harvesting, as well as a decrease in charge recombination

caused by direct conduction along the multigeneration branches of the crystalline ZnO nano trees. To capture more sunlight, this strategy imitates branching plant structures. The authors conducted a parametric analysis to combine length-wise growth (LG) and branching growth (BG) to increase the efficiency of ZnO NW photoanodes.

Han et al. [59] successfully developed an 11.4% efficient DSSC through the design and synthesis of donor-acceptor type co-adsorbents that efficiently overcame the competitive light absorption by I^-/I_3^- , avoided dye aggregation, and decreased charge recombination. In [60], a carboxy-anchor organic dye of LEG4 was demonstrated to work well as a collaborative sensitizer with the silyl-anchor dye of ADEKA-1 in DSSCs. The authors were able to produce a 14.3% efficient cell with an optimized cobalt(III/II) complex redox electrolyte solution and the GNP counter electrode. This demonstrates that silyl-anchor dyes are a viable option for use as photosensitizers in DSSCs, which is mostly attributable to the fact that ADEKA-1 has good adsorption characteristics to the TiO_2 electrode. Figure 2 provides a schematic of a DSSC.

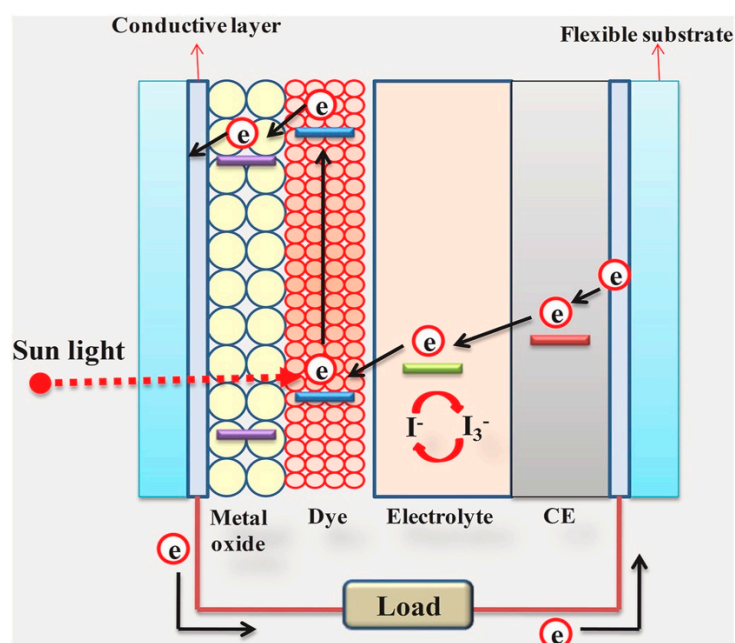


Figure 2. DSSC schematic [61]. Reproduced with permission from Devadiga et al., Renewable and Sustainable Energy Reviews, Elsevier, 2022.

2.2. Components of DSSCs

2.2.1. Photo-Anodes

The photo-anode is made up of semiconductor nanoparticles placed on a transparent conducting glass that has been dye-sensitized [62]. For the photo-anode, numerous semiconductor oxides such as ZnO, SnO_2 , WO_3 , and TiO_2 are used as a material. Among these semiconductor oxides, TiO_2 has received more attention due to its availability, low cost, compatibility, and lack of toxicity [62].

The morphology of a semiconductor plays a vital role in a DSSC, since it acts as a substrate for the absorption of dye and receives electrons from the dye [63]. The dye, upon photo-excitation, introduces the electron into the semiconductor's conduction band, where it is further transferred to the counter electrode, completing the circuit. TiO_2 nanoparticles are frequently utilized because of their excellent dispersion and crystallinity. Anatase, brookite, and rutile are the three most stable polymorphs of TiO_2 ; the complex synthesis process of the brookite makes it the least common among the mentioned polymorphs of TiO_2 . The solar energy conversion performance of anatase and rutile to some extent is the same; however, anatase is favored over rutile due to its superior charge transport, larger specific area, and higher electron Fermi level. In addition, anatase has a bandgap

of 3.2 eV compared to 3.0 eV for rutile, resulting in greater conduction-band energies for the anatase form [64]. Researchers are working hard to create different nanostructures for anatase such as nanorods, nanofibers, and nanowires using different synthesis techniques, including solvothermal, hydrothermal, micelle, inverse micelle, physical vapor deposition, and chemical vapor deposition. An efficient electrode has a compact layer of ca. 20 nm sized nanoparticles and has a thickness of 12–14 μm , while the scattering layer is of ca. 400 nm sized nanoparticles and has a thickness of 4–6 μm [65]. Screen printing [66,67], doctor blade [68], spin coating [69], and spray coating [70,71] are the different techniques used for coating TiO_2 on the conducting glass substrate.

2.2.2. Dye Sensitizers

The dye in a DSSC plays a very important role—that is, to absorb solar energy and convert it into electrical energy [72]. By keeping the role of a dye in DSSC in mind, some key conditions are required for a dye to be considered efficient, namely [62]:

1. it must be capable of maximum absorption from the visible region and near-infrared region;
2. it should have excellent binding with anode material;
3. the anode material conduction band must be low compared to the LUMO (Lowest Unoccupied Molecular Orbital) of a dye;
4. the anode material conduction band must be high compared to the HOMO (Highest Occupied Molecular Orbital) of a dye;
5. it must be durable.

Premetallized, natural, and metal-free synthetic organic are the three different types of dye sensitizers. Among the mentioned sensitizers, premetallized sensitizers exhibit the highest efficiency and greatest stability. However, manufacturing these dyes is difficult, costly, and harmful to the environment. Metal-free synthetic organic sensitizers such as premetallized sensitizers require a complicated production procedure. On the other hand, natural dyes can easily be extracted from seeds, leaves, fruits, stems, etc. [73]. Premetallized and metal-free synthetic organic dye-based DSSCs have high efficiency compared to natural dye based DSSCs. On the other hand, unlike the premetallized and metal-free synthetic organic dyes, natural dyes do not need any complex preparation process and are cheap, non-toxic, and environmentally friendly [74].

2.2.3. Electrolytes

In a DSSC, the electrolyte is another very important component as it can affect the stability and performance of a cell [75]. The redox couple, organic solvent, and additives are the essential components of an electrolyte. Liquid electrolytes, solid electrolytes, and quasi-solid electrolytes are the three different types [62]. Due to their better dielectric constant, donor number, and viscosity, 3-methoxy propionitrile, propylene carbonate, acetonitrile, butyrolactone, and valeronitrile are the most frequently used solvent in a liquid electrolyte [76]. In electrolytes, the component that behaves as a reducing and an oxidizing agent is the redox couple. The redox couples, I^-/I_3^- , $\text{Co(II)}/\text{Co(III)}$, due to their enhanced performance, are commonly used in DSSCs [77]. The purpose of additives is to prevent recombination reactions at the electrolyte interface, which is critical since these reactions reduce the J_{sc} and V_{oc} , lowering the overall cell performance. Heterocyclic nitrogen-containing substances, such as pyridine and its derivatives, are frequently utilized as additives. This results in a negative shift of the conduction band, which raises the V_{oc} while lowering the J_{sc} . The two additives that are most often employed are 4-tert-butyl pyridine (tBP) and N-methylbenzimidazole. The mechanism by which additives such as guanidinium and thiocyanate work is quite different from that of the aforementioned additives, since they provide a positive shift to the conduction band, causing an increase in V_{oc} [78,79]. Recently, it has been reported that DSSCs having polyaniline in their electrolyte are more efficient than those without polyaniline—6.56% and 5.00%, respectively [80].

2.2.4. Counter Electrodes

The counter electrode (CE) transfers electrons to the electrolyte from the outer circuit to regenerate the redox pair. Therefore, the CE must have low resistance and should have high stability. An efficient CE material should have a high surface area, good chemical stability, high conductivity, low resistance, high current density, and good corrosion stability [81]. Platinum (Pt) is considered an efficient CE material due to its high conductivity towards I^-/I^{3-} and excellent electrocatalytic activity [81,82]. The fabrication of Pt CE can be accomplished using chemical reduction, chemical vapor deposition, electrochemical deposition, hydrothermal reaction, thermal decomposition, or sputtering [83]. Despite the fact that Pt has excellent properties, it is very costly and cannot fit into a wide range of applications. Therefore, many researchers are investigating alternatives that have high efficiency, low cost, and good stability. A wide range of research has been carried out using numerous types of carbon, such as carbon nanotubes; carbon nanofibers and graphite [83–87]; Pt alloys such as $Pt_{0.02}Co$, NiPd, and PtPdNi [79,83]; alternative metals such as Ruthenium (Ru), Iridium (Ir), Gold (Au), Titanium (Ti), and Silver (Ag) [83]; bilayers such as Au/Pt, Cu/Pt, Ti/Ru, and Al/Ru [83,84]; and polymers such as Polyaniline and Polypyrrole [83,88].

In the cases of TiO_2 and ZnO, incorporating co-additives increases the efficiency of the cell. Significantly more effective solar cells were produced using a variety of other approaches, including the molecular engineering of sensitizers, different printing processes, and improvements with anchoring groups, as summarized in Table 1.

Table 1. The performance of cells with different designs in combination with liquid and solid-state electrolytes using different electrodes.

Cell Type	Dye	Photoanode/ Cathode	Electrolyte	CE	V_{oc} (V)	J_{sc} (mA_{cm}^{-2})	FF	η (%)	Refs.
Wine Daisy flower petals	Anthocyanin (Lv)	TiO_2/ITO	I^-/I^{3-}	Graphite C/ITO	0.52	0.38	0.26	0.79	[89]
Wine Daisy flower petals	Anthocyanin (Lv)	TiO_2/ITO	I^-/I^{3-}	Pt/ITO	0.52	0.42	0.27	0.87	[89]
Ru (II) complexes bearing diamine-based bidentate ligands	Ru (II) 8A	TiO_2/FTO	I^-/I^{3-}	Pt/FTO	0.64	5.13	0.68	2.25	[90]
Co-additive CDA	N719 + 7.5 mM CDA	TiO_2/FTO	I^-/I^{3-}	Graphite C-PEDOT: PSS/FTO	0.79	11.64	0.76	7.00	[91]
Co-additive CDA	RhB + 10 mM CDA	TiO_2/FTO	I^-/I^{3-}	Graphite C-PEDOT: PSS/FTO	0.61	4.19	0.69	1.75	[91]
Co-additive CDA	D149 + 10 mM CDA	TiO_2/FTO	I^-/I^{3-}	Graphite C-PEDOT: PSS/FTO	0.81	13.77	0.69	7.72	[91]
TiO_2/ZnO Blocking Layer	N719	TiO_2 NP/ $TiO_2/ZnO/FTO$	I^-/I^{3-}	Pt/FTO	0.73	16.63	0.59	7.10	[92]
2-cyanoacetani lide based organic dyes	Ru (II) complex HD-2 with SA1	TiO_2/FTO	I^-/I^{3-}	Pt/FTO	0.68	20.33	0.58	8.02	[93]
Catecholpyr ano-5,7,3',4'-tetrahydroxy flavylum pyranoflavylum salts	Pyrananthocyanin	TiO_2/FTO	I^-/I^{3-}	Pt/FTO	0.34	6.43	0.53	1.15	[94]
Natural liquid dye extract 12-hour immersion	PIW Leaf chlorophyll	TiO_2/ITO	I^-/I^{3-}	Candle soot C/ITO	0.42	0.14	0.41	0.02	[95]
Screen printing 0.25 cm^2	D35	TiO_2 NP/FTO	I^-/I^{3-}	Pt/FTO	0.76	10.03	0.72	5.48	[96]
Digital printing 0.25 cm^2	D35	TiO_2 NP/FTO	I^-/I^{3-}	Pt/FTO	0.78	12.65	0.75	7.40	[96]
(D-A- π -A) type zinc porphyrin sensitizers	TH-2F	TiO_2/FTO	0.1 M TBAPF6	Pt/FTO	0.68	16.07	0.64	6.98	[97]

Table 1. Cont.

Cell Type	Dye	Photoanode/ Cathode	Electrolyte	CE	V _{oc} (V)	J _{sc} (mAcm ⁻²)	FF	η (%)	Refs.
Gel polymer electrolyte based DSSCs	Black mulberry fruits juice	TiO ₂ /FTO	AMPS-IA-F-Cl-Br-An	Pt/FTO	0.40	0.02	0.49		[98]
Combination of natural red and green dyes	80% R +20% G	TiO ₂ /FTO	I ⁻ /I ³⁻	C (CNT)/FTO	0.30	4.65	0.55	0.99	[99]
Mixed one layer Pigment combination	Chlorophyll and anthocyanin volumetric proportion of 1:1	TiO ₂ /FTO	I ⁻ /I ³⁻	Pt/FTO	0.72	1.61	0.73	0.85	[100]
Two distinct layer Pigment combination	Chlorophyll and anthocyanin volumetric proportion of 1:1	TiO ₂ /FTO	I ⁻ /I ³⁻	Pt/FTO	0.71	1.38	0.74	0.74	[100]

An efficient dye is essential for the fabrication of an efficient DSSC. Zhang et al. [85] fabricated four different A'-π-A type dyes, ZS10–ZS13. To investigate the performance of these dyes, the authors constructed a DSSC on a 10 μm TiO₂ film using an I⁻/I³⁻ electrolyte. It was observed that ZS13 provided the best Voc value of 697 mV (see Figure 3a), while ZS12 provided the best Jsc and PCE values (see Figure 3b) of 14.96 mA cm⁻² and 6.75%. To study the effect of molecular size on the overall performance of a DSSC, co-sensitization experiments of these dyes with porphyrin dye YD2 were carried out. From these experiments, it was noted that the Voc of ZS13+ YD is still high, but ZS12+YD provided the highest Jsc and PCE values compared to the other dyes (see Figure 3c,d).

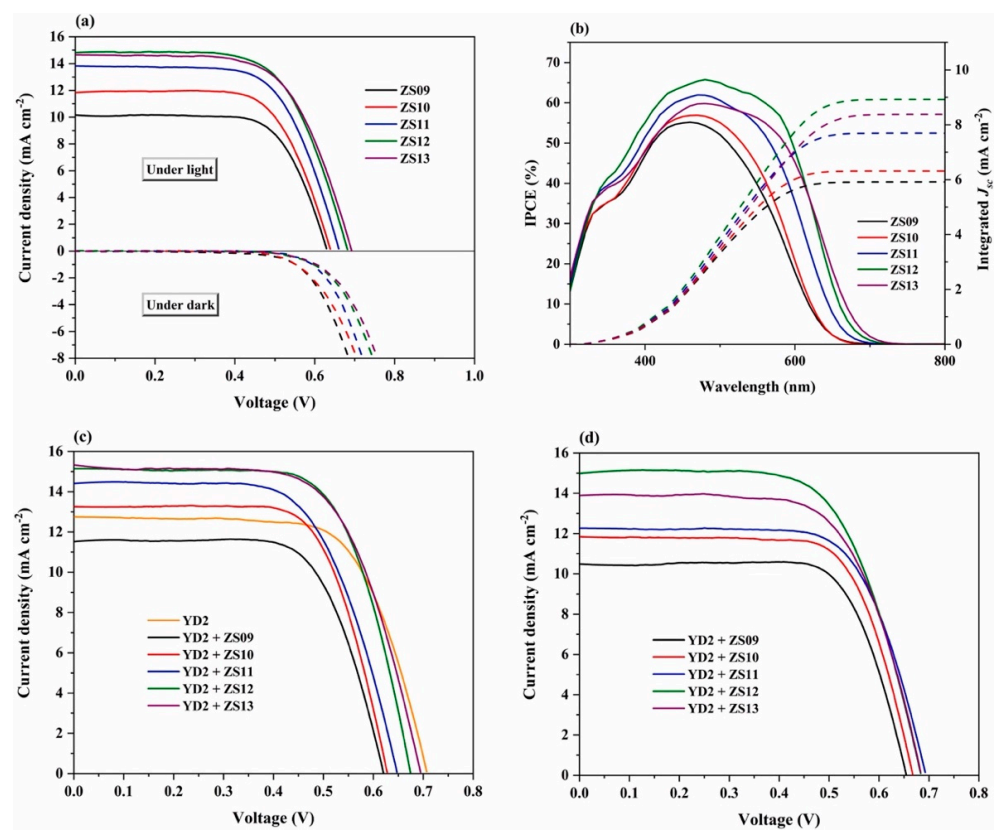


Figure 3. (a) J–V characteristic curves of DSSCs based on ZS09–ZS13; (b) IPCE of DSSCs based on ZS09–ZS13; (c) J–V characteristic curves of DSSCs sensitized with YD2 and ZS09–ZS13; (d) IPCE of DSSCs sensitized with YD2 and ZS09–ZS13 [85]. Reproduced with permission from Zhang et al., *Dyes and Pigments*, Elsevier, 2022.

2.3. Challenges in DSSCs

The substrates used in DSSC are mostly plastic, having a low thermal processing limit of around 150 °C, so for a working electrode, the coating of nano-crystalline film on plastic is the most significant problem. Organic binders are not used in the coating process due to their tendency to persist in semiconductor films processed under 400 °C.

Due to the lack of binders in semiconductor pastes, the film will break down as it dries, raising the electrical resistance. By using plastic substrates, low-temperature processing lowers semiconductor film adhesion to the substrate and causes poor electrical contact between semiconductor particles. Due to oxygen and moisture input from porous and permeable plastic substrates, plastic-based DSSC technologies pose a substantial problem in terms of device stability. These modules would need to go through a strict encapsulation procedure with low or no impact on production costs if they were to be commercialized. Plastic-based DSSC poor conversion efficiency is mostly due to their inability to withstand high-temperature heat treatments. For the fabrication of efficient plastic-based DSSCs, changes have to be introduced in making semiconductor paste and an alternative technique that can enhance the connection between the semiconductor film and the substrate.

3. Perovskite Solar Cells

The perovskite solar cell (PSC) is an emerging solar cell technology that has received a great deal of attention from researchers in the last few years [101]. These cells possess an active/absorber layer made of perovskite material [102]. PSCs have the potential to be an energy source in the future by virtue of properties that are discussed in this section. However, before claiming it to be a viable commercial product, some issues still need to be resolved. These issues and the significant advancements the PSC technology has made in recent years are highlighted in this section.

In 2009, Kojima et al. [25] first introduced a perovskite material-based solar cell having an efficiency of ca. 3.8%. In PSCs, methylammonium lead bromide ($\text{CH}_3\text{NH}_3\text{PbBr}_3$ or MAPbBr_3) and methylammonium lead iodide ($\text{CH}_3\text{NH}_3\text{PbI}_3$ or MAPbI_3) perovskite materials are used as an absorber layer, with bandgaps of 2.3 eV and 1.6 eV. In 2021, a 25.5% efficient PSC was reported by Green et al. [13] comparing favorably with traditional solar cells (crystalline silicon-based). Aside from solar cells, they can be used in photodetectors and light-emitting diodes [103,104]. A PSC having 25.7% power conversion efficiency was also reported by Ulsan National Institute of Science and Technology (UNIST) (The evolution of the efficiencies of solar cells with time is available from The National Renewable Energy Laboratory (NREL) Best research-cell efficiency chart. "<https://www.nrel.gov/pv/cell-efficiency.html> (accessed on 9 January 2023)").

Perovskite materials have some outstanding properties that match the requirements for photovoltaics applications, and these include a high diffusion length ($\sim 1 \mu\text{m}$), a high carrier mobility, strong absorption, and a low recombination rate. Single-crystalline MAPbI_3 has a defect density of 10^{10} cm^{-3} , which is significantly less than that for polycrystalline perovskites [102,105]. Single-crystalline $\text{CH}_3\text{NH}_3\text{PbI}_3$ perovskite has a carrier lifetime of a few hundred microseconds and a diffusion length of 175 nm [106]. Another outstanding feature of the $\text{CH}_3\text{NH}_3\text{PbI}_3$ perovskite material is its ambipolar transport capability, which allows it to function as a hole transport material [107]. Etgar et al. announced hole transport material (HTM) free PSC with a PCE of 5.5% for the first time in 2012 [108]. Several research groups have published experimental studies on perovskite materials [109–112]. In addition to practical research, several theoretical investigations have been conducted in order to comprehend the electrical characteristics, potential, and restrictions of perovskite materials for diverse device applications [113–115]. Some of the notable properties of perovskite materials such as high bandgap, binding energy, carrier mobility, and trap-state density are summarized in Table 2.

Table 2. Properties of perovskite materials.

Properties	Value Range
Bandgap	1.5–2.5 eV
Exciton binding energy	Less than 10 meV
Crystallization energy barrier	56.6–97.3 kJ mol ⁻¹
Relative permittivity	3
Charge carrier lifetime	Greater than 300 ns
PL quantum efficiency	70%
Trap-state density	10 ¹⁰ cm ⁻³ (single crystals), 10 ¹⁵ –10 ¹⁷ cm ⁻³ (polycrystalline)
Carrier mobility	800 cm ² /Vs

Figure 4 shows a schematic of a PSC. The basic components of a PSC structure are an electron transport layer (ETL), a hole transport layer (HTL), and a light absorber (perovskite) layer. The usual configuration of a device is glass, transparent conductive oxide (TCO), ETL, perovskite, HTL, and a metal electrode. This first n-i-p PSC structure was obtained from the DSSC [25]. In PSC, perovskite materials such as MAPbI₃ and MAPbBr₃ are used instead of the dye material. Both a one-step (single-step technique) and a two-step (sequential deposition method) approach may be used to deposit the active layer (perovskite layer) in these devices. Deposition of CH₃NH₃PbI₃ perovskite film lead iodide (PbI₂) and methylammonium iodide (CH₃NH₃I, MAI)-based solvent is used in a one-step approach, while in a two-step approach, CH₃NH₃I is deposited after PbI₂ to obtain CH₃NH₃PbI₃ perovskite [116–118].

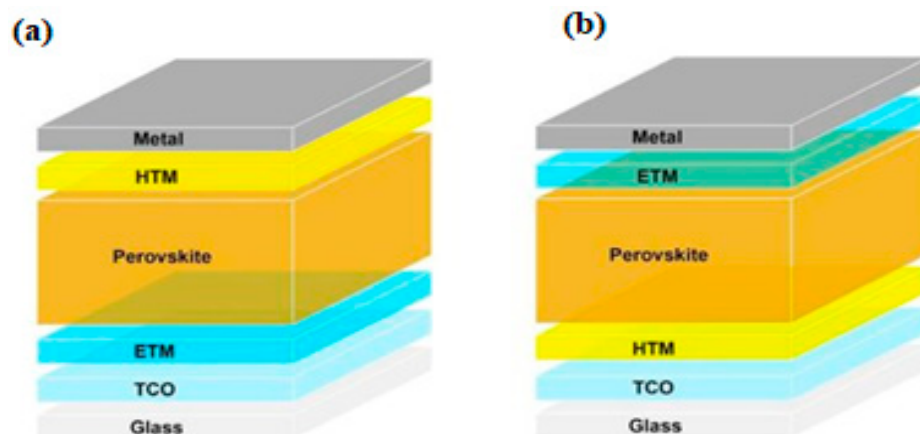


Figure 4. Perovskite solar cell device structure: (a) conventional and (b) inverted [119]. Reproduced with permission from Tonui et al., *Renewable and Sustainable Energy Reviews*, Elsevier, 2018.

3.1. Structure and Working Mechanisms of a PSC

The standard chemical formula for perovskite compounds is ABX₃, where “A” and “B” are cations of various sizes and “X” is an anion [120,121]. A basic perovskite compound unit cell equivalent structure is shown in Figure 5. Organometallic perovskites that have an organic cation (e.g., methyl-ammonium CH₃NH₃⁺, ethyl-ammonium CH₃CH₂NH₃⁺, formamidinium NH₂CH=NH₂⁺, and cesium Cs), a metal cation (e.g., Ge₂⁺, Sn₂⁺, Pb₂⁺), and a monovalent halogen anion (e.g., F⁻, Cl⁻, Br⁻, I⁻) are the most significant ones for PSCs [122].

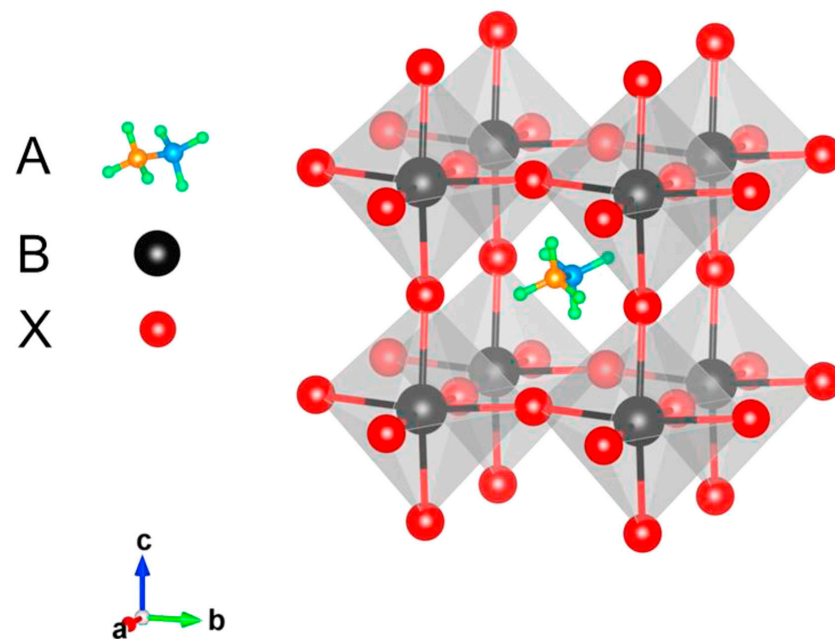


Figure 5. Crystal structure of ABX₃ perovskites material [123]. Reproduced with permission from Wang et al., *Solar Energy Materials and Solar Cells*, Elsevier, 2016.

For optoelectronic applications, the tuning of the perovskites CH₃NH₃PbI₃ and CH₃NH₃PbBr₃ exhibits bandgap tunability in the green-IR and blue-green regions of the spectrum [124]. In ABX₃ perovskite, the valence band and conduction bands are formed by antibonding of hybridization and π antibonding of the “B = Pb, Sn” s-state and the “X = Br, Cl, I” p-state, respectively. Moreover, “A = methyl-ammonium, formamidinium” does not directly contribute to the valence band maximum and conduction band minimum; however, it does affect the lattice constant. From studies, it is noted that by increasing the lattice constant, the bandgap increases [125]. Therefore, the selection of “A”, “B”, and “X” should be made very carefully, as it affects the stability and overall performance of a PSC.

Tsai et al. [126] presented a study on the implementation of thin films composed of nearly single-crystalline quality perovskite. The crystallographic planes of the inorganic perovskite component were found to exhibit a pronounced out-of-plane alignment for the contacts in planar solar cells, which was observed to enhance the efficiency of charge transport. The authors were able to attain an efficiency of 12.52% without hysteresis. Furthermore, the devices demonstrated significantly enhanced stability when subjected to light, humidity, and heat stress tests, as compared to their three-dimensional counterparts. The research findings indicated that two-dimensional perovskite devices, which lack encapsulation, can maintain their efficiency at a rate exceeding 60% for more than 2250 h under standard (AM1.5G) illumination. Additionally, these devices demonstrate a higher tolerance to 65% relative humidity in comparison to their three-dimensional counterparts. Encapsulation of the devices results in no sign of any degradation in the layered devices when exposed to constant AM1.5G illumination or humidity. In [127], a comprehensive methodology was presented for enhancing the efficiency of PSCs via optimized management of charge carriers. Initially, an electron transport layer is fabricated with optimal film coverage, thickness, and composition through the tuning of the chemical bath deposition process of SnO₂. Subsequently, a passivation strategy is implemented to dissociate the passivation process between the interface and bulk, resulting in enhanced properties, while simultaneously reducing the bandgap penalty. Under forward bias conditions, the devices demonstrate an external quantum efficiency for electroluminescence of up to 17.2% and an energy conversion efficiency for electroluminescence of up to 21.6%. These solar cells have been certified to attain a power conversion efficiency of 25.2%.

A systematic investigation was conducted by Jiang et al. [128] to examine the impact of the precise stoichiometry, with a particular focus on the PbI_2 contents, on the performance of the device. The properties evaluated included hysteresis, efficiency, and stability. The study revealed that a moderate amount of residual PbI_2 can result in stable and efficient SCs without hysteresis. Conversely, excessive residual PbI_2 can cause significant hysteresis and poor transit stability. SCs demonstrated efficiencies of 21.6% for small sizes (0.0737 cm^2) and 20.1% for large sizes (1 cm^2), while retaining moderate residual PbI_2 in the perovskite layer. The certified efficiency of small-sized planar structure PSCs was found to be 20.9%.

A commonly accepted simplified operating concept of PSC is as follows: when light strikes a PSC, the perovskite absorbs light and creates excitons. Thermal energy creates electron and hole pairs, which diffuse and separate through their contacts, respectively. When electrons and holes are present at the anode and cathode, respectively, an external load can be powered in a circuit. Comparable charge carrier diffusion lengths and optical absorption lengths result in optimum performance.

3.2. Techniques to Improve Efficiency

The efficiency of a PSC can be improved by improving light absorption, optimizing charge transport, and interface engineering. Since light absorption produces the carriers, the performance metrics of PSCs, such as PCE, open circuit voltage, and short circuit current, are greatly influenced by the quality of the light absorption layer. Methods for improving light absorption include additive engineering, component engineering, and defect passivation [129].

To increase the light harvesting capacity/efficiency of PSCs, different research groups used different additives with different perovskite compositions. Yang Yi et al. [130] used ammonium benzenesulfonate with MAPbI_3 perovskite composition and recorded an efficiency of 17.29%. For the same perovskite composition, Wang et al. [131], Kumar et al. [132], and Liu et al. [133] used 1-alkyl-4-amino-1,2,4-triazolium, dibutylhydroxytoluene, and pyrrole and reported efficiencies of 16.13%, 17.10%, and 18.58%, respectively. Li et al. [134], and Zhang et al. [135], on the other hand, used 1-propionate-4-amino-1,2,4-triazolium tetra fluoroborate (PATMBF_4) and a 6-aminoquinoline mono hydrochloride (AQCl) with $\text{Cs}_{0.05}(\text{FA}_{0.85}\text{MA}_{0.15})_{0.95}\text{Pb}(\text{I}_{0.85}\text{Br}_{0.15})_3$ composition, reporting efficiencies of 18.27%, and 19.24%, respectively. Studies using different additives are summarized in Table 3.

Table 3. Additives employed in PSCs to enhance device performance (PCE).

Perovskite Composition	Additive Name	V_{OC} (V)	J_{SC} (mA cm^{-2})	FF (%)	η (%)	Additive (%)	Refs.
MAPbI_3	ammonium benzenesulfonate	1.09	22.92	78.62	17.29	19.64	[130]
MAPbI_3	1-alkyl-4-amino-1,2,4-triazolium	1.10	23.39	77.84	16.13	20.03	[131]
MAPbI_3	dibutylhydroxytoluene	1.03	22.50	78.10	17.10	18.10	[132]
MAPbI_3	pyrrole	1.142	23.38	75.20	18.58	20.07	[133]
$\text{Cs}_{0.05}(\text{FA}_{0.85}\text{MA}_{0.15})_{0.95}\text{Pb}(\text{I}_{0.85}\text{Br}_{0.15})_3$	1-propionate-4-amino-1,2,4-triazolium tetrafluoroborate (PATMBF_4)	1.11	23.74	81.02	18.27	21.35	[134]
$\text{Cs}_{0.05}(\text{MA}_{0.12}\text{FA}_{0.88})_{0.95}\text{Pb}(\text{I}_{0.88}\text{Br}_{0.12})_3$	6-aminoquinoline monohydrochloride (AQCl)	1.18	22.74	80.73	19.24	21.66	[135]
$\text{CH}_3\text{NH}_3\text{PbI}_3$	carbon quantum dots(A-CQDs)	0.94	22.35	51.27	9.15	10.74	[136]
CsPbI_3	bis(pentafluorophenyl)zinc [$\text{Zn}(\text{C}_6\text{F}_5)_2$]	1.12	20.67	81.98	16.97	19.00	[137]
CsPbI_2Br	2-hydroxyethyl methacrylate (HEMA)	1.23	15.81	82.98	14.10	16.13	[138]
CsPbI_3	ethanol/MACI (Et-M)	0.928	20.75	68.43	9.49	13.18	[139]

The light absorption layer absorbs light to create holes and electrons, which flow to the external circuit through the HTL and ETL, respectively. ETL and HTL material optimization can effectively transfer photo-generated charges and can reduce optical and electrical losses in the device [140–142]. As summarized in Table 4, various efforts have been made to develop transmitting materials to minimize losses. Han et al. [143] used ZTO-ZnS as an ETL with a $\text{Cs}_{0.05}(\text{FA}_{0.85}\text{MA}_{0.15})_{0.95}\text{Pb}(\text{Br}_{0.15}\text{I}_{0.85})_3$ perovskite composition, recording an efficiency of 21.30%. Wang et al. [144] used MPA-BTTI as the HTL with CsFAMA and achieved an efficiency of 21.17%, while Pham et al. [145] used 2,3-bis(4'-(bis(4-methoxyphenyl) amino)-[1,1'-biphenyl]-4-yl)fumaronitrile(TPA-BPFN-TPA) as the HTL with a $\text{CH}_3\text{NH}_3\text{PbI}_3$ perovskite composition and recorded an efficiency of 18.40%.

Table 4. Optimization of transmission materials in PSCs to enhance device performance (PCE).

Perovskite Composition	Transmission Material	V_{oc} (V)	J_{sc} (mA cm^{-2})	FF (%)	η (%)	Refs.
$\text{Cs}_{0.05}(\text{FA}_{0.85}\text{MA}_{0.15})_{0.95}\text{Pb}(\text{Br}_{0.15}\text{I}_{0.85})_3$	ZTO-ZnS(ETL)	1.15	23.80	77.70	21.30	[143]
CsFAMA	MPA-BTTI(HTL)	1.12	23.23	81.40	21.17	[144]
$\text{CH}_3\text{NH}_3\text{PbI}_3$	2,3-bis(4'-(bis(4-methoxyphenyl)amino)-[1,1'-biphenyl]-4-yl)fumaronitrile(TPA-BPFN-TPA)(HTL)	1.04	22.70	78.00	18.40	[145]
CsPbBr_3	Nb_2O_5 (a- Nb_2O_5)(ETL)	1.45	5.64	70.00	5.74	[146]
$\text{Cs}_{0.05}(\text{FA}_{0.85}\text{MA}_{0.15})_{0.95}\text{Pb}(\text{I}_{0.85}\text{Br}_{0.15})_3$	Cu_2OCuSCN nanocomposite (HTL)	1.05	23.23	78.40	19.20	[147]
$\text{CH}_3\text{NH}_3\text{PbI}_3$	$\text{BaTiO}_3/\text{TiO}_2$ (ETL)	0.97	20.50	65.00	13.00	[148]
$(\text{FAPbI}_3)_{0.85}(\text{MAPbBr}_3)_{0.15}$	3,6-N(HTL)	1.08	22.65	78.00	19.25	[149]
$\text{Cs}_{0.05}(\text{MA}_{0.13}\text{FA}_{0.87})_{0.95}\text{Pb}(\text{I}_{0.87}\text{Br}_{0.13})_3$	PdPrPc (HTL)	1.08	23.49	71.11	18.09	[150]
$(\text{CsPbI}_3)_{0.05}(\text{FA}_{0.85}\text{MA}_{0.15}\text{Pb}[\text{I}_{0.85}\text{Br}_{0.15}]_3)_{0.95}$	$\text{NH}_2\text{-ZnO@SnO}_2$ (ETL)	1.14	25.11	78.68	22.52	[151]
CsPbIBr_2	In_2S_3 (ETL)	1.09	7.76	65.94	5.59	[152]

For improving the performance of PSCs, apart from additives and optimized transmitting materials, the device interface can also be tuned. The interface has a direct impact on electrical charge extraction, transportation, recombination, and photon transfer [153,154]. Therefore, by using optimized interface techniques, efficient cells can be obtained. Zhang et al. [155] used a FTO/ TiO_2 /perovskite/(Me-PDA) Pb_2I_6 /Spiro-OMETAD/Au interface and reported 22.0% efficiency. Li et al. [156] and Liu et al. [157] used FTO/PCBM/perovskite/Spiro-OMETAD/Au and ITO/ SnO_2 /perovskite/PTAA/Metal interfaces and recorded efficiencies of 20.12% and 20.30%, respectively.

Table 5 summarizes the performances of PSCs with various interface materials. What is noticeable is the remarkable similarity in all performance metrics with the various materials, and that they use gold and silver. The interface has a direct impact on charge extraction, transport, recombination, and photon transport. Perovskite solar cells (PSCs) typically feature a perovskite active layer, a charge transport layer for electrons and holes, and a current collector electrode in a stacked multi-layer configuration. There are four main interfaces between the layer, i.e., the ETL, perovskite, HTL, and electrode. By adjusting the interface, energy levels can be rearranged, and the surface morphology can be improved. Enforcing better contact between the perovskite and ETL/HTL can enhance the efficiency of electron and hole transport.

Table 5. Interface modification employed in PSCs to enhance device performance (PCE).

Device Structure	V _{OC} (V)	J _{SC} (mA cm ⁻²)	FF (%)	η (%)	Refs.
FTO/TiO ₂ /perovskite/(Me-PDA)Pb ₂ I ₆ /Spiro-OMETAD/Au	1.13	24.61	79.00	22.00	[155]
FTO/PCBM/perovskite/Spiro-OMETAD/Au	1.12	22.77	79.00	20.12	[156]
ITO/SnO ₂ /perovskite/PTAA/Metal	1.11	24.06	75.81	20.30	[157]
ITO/NiO _x /PTAA/(MAPbI ₃) _{0.95} (MAPbBr ₂ Cl) _{0.05} /PCBM/BCP/Ag	1.19	22.23	81.71	21.56	[158]
FTO/c-TiO ₂ /perovskite/PTABr/PTAA:LAD/Au	1.09	23.28	79.13	20.13	[159]
FTO/bl-RiO ₂ /MAPbI ₃ /PbS/Spiro-OMETAD/Au	1.14	23.17	72.83	19.24	[160]
ITO/SnO ₂ /MAPbI ₃ /4-CIBA Spiro-OMETAD/Ag	1.16	22.76	74.00	20.99	[161]
FTO/SnO ₂ /BCP/Spiro-OMETAD/Ag	1.14	23.50	77.10	20.60	[162]

To enhance the PCE of PSC, alongside finding new ETMs, controlling the morphology of the perovskite layer plays a vital role as it is significantly related to charge transport and dissociation [163,164]. Efficient PSCs require highly crystalline, surface smooth, and pin-hole free perovskite films. The processing conditions have a great effect on the perovskite layer morphology [165,166]. Huang et al. [167] employed fluorinated perylene diimide (FPDI) as an organic ETM in PSCs. The perovskite film was produced via sequential vacuum vapor deposition, and the morphology of the film was able to be modified by optimizing the FPDI film morphology using either solvent vapor annealing (SVA) or short-time solvent spin-coating. The fill factor (FF) of the perovskite solar cell improved from 30.44% to 55.20%, boosting PCE from 3.23% to 7.44%, after treating the FPDI film with chloroform SVA for 30 min. In 2014, Jeon et al. [168] show that high-performance PSCs may be fabricated with excellent consistency by including N-cyclohexyl-2-pyrrolidone as a morphological controller in N,N-dimethylformamide in very low concentrations. A PCE of 10% and a performance deviation of less than 0.14% were accomplished with film morphology that was highly homogeneous, similar to that attained using vacuum-deposition techniques.

Due to their excellent properties, such as low cost, flexibility, solution-processability, and compatibility with large-area fabrication, PSCs are viewed as the strongest candidates for third-generation efficient SCs. Bandgap engineering is crucial for light harvesting and conversion, but most perovskites have a high or indirect bandgap compared to the optimal bandgap range (1.3–1.4 eV) for single-junction solar cells. Ergen et al. constructed a novel structure for PSCs that achieved a steady-state average PCE of 18.4%, with a best recorded steady-state PCE of 21.7%, while the peak PCE was 26% [169]. Two different mixtures were created: one with lead and iodine doped with bromine; and the other with methyl, ammonia, tin, and iodine. Infrared light of 2 eV was absorbed by the first mixture, while light of 1 eV was absorbed by the second [170].

3.3. Film Fabrication Techniques

PSC fabrication has advanced to the point where the commercialization of PSCs is possible. In 2021, SAULE TECHNOLOGIES, a Poland-based company, launched the world's first production line of solar panel based on perovskite technology by using a novel inkjet printing technique presented by Olga Malinkiewicz et al. [171]. The authors achieved an efficient thin-film SC by sandwiching a printed CH₃NH₃PbI₃ perovskite layer between two thin organic charge transporting layers acting as a hole and electron blocker and connecting them through indium tin oxide (ITO)/PEDOT:PSS and Au as hole and electron extracting contacts, respectively. By using this architecture, the authors were able to produce a 12% efficient SC. Some widely used film fabrication techniques are highlighted in this section.

3.3.1. Spin Coating

A liquid layer is spread over a rotating substrate using the batch technique known as spin coating [172]. The technique has been widely employed in the production of smaller

PSCs with an area of approximately 0.1 cm^2 , as well as in the fabrication of expansive devices with an area of 1 cm^2 . It is classified as either a one-step or a two-step process. Perovskite-based devices produced using spin coating have demonstrated PCEs exceeding 9.4% [173]. In [174], the authors generated a large-area perovskite film with a diameter of 57 cm^2 , demonstrating the possibility for the spin coating to produce reasonably large-area PSCs, provided that evaporation of the solvent can be properly managed. Perovskite deposition is improved with two-step sequential processing compared to the one-step technique. Furthermore, it is possible to improve the quality of films by regulating the crystal growth [174].

3.3.2. Inkjet Printing Method

The inkjet technique is a printing technique that enables direct ink deposition control and significantly lowers material use and waste. Multipass inkjet-printed PSCs have been successfully fabricated and optimized by Mathies et al. [175]. The authors were able to obtain 11.3% efficient PSCs using MAPbI_3 ink in the multipass inkjet printing technique. Using printed $\text{CH}_3\text{NH}_3\text{PbI}_3$, the authors in [176] were able to create PSCs having a PCE of 13.27% with an effective area of 4.0 cm^2 . Li et al. developed large-area PSCs using advances in the inkjet printing technique. Before combining lead-iodide-based ink with MAI vapor for producing MAPbI_3 , the authors employed a two-step technique to chemically modify the lead-iodide ink. The resulting PSC device having an area of 2.02 cm^2 achieved 17.74% efficiency [177].

3.3.3. Spray Coating Methods

Spray coating is a low-temperature and low-ink-concentration technique that is a widely used in the industry for deposition [178]. It is highly scalable, making it suitable for producing large-area thin perovskite sheets. The perovskite film made with this technique exhibits high uniformity over vast areas. The process of spray coating involves four distinct steps, namely the generation of ink droplets, their deposition onto the substrate, combining them into a wet film, and then the drying of the film. Spray coating is quite versatile in comparison to other scalable technologies. It includes one-step and two-step methods of deposition. Aprotic solvents are used in one-step film deposition solutions [178,179]. In the two-step processes, metal salts are deposited in an aprotic solvent using either a spray coating or a spin coating.

The authors in [180] produced high-efficiency large-area PSCs with NiO-based HTLs that were synthesized using a spray pyrolysis technique. In different studies, PSCs that had active areas measuring 1 cm^2 have demonstrated average PCEs of 17.6% [180], 18.21% [181], and 19.19% [182]. A photovoltaic device with a greater surface area, specifically 5 cm^2 , achieved an average PCE of 15.5%, as reported in [183]. $\text{TiO}_2/\text{Al}_2\text{O}_3/\text{NiO}/\text{carbon}$ framework-based PSCs have demonstrated PCEs of up to 15.03% [184]. PSCs showed good device stability and a mean PCE of 17.6% when using a recent simple spray deposition approach for a CuI film [185].

3.3.4. Blade-Coating Method

Blade coating, referred to as doctor-blading and knife-over-edge coating, is a process in which a blade slides across a surface, or vice versa in the case of roll-to-roll coating [186]. Pre-dispensed ink is spread with the blade to create a film of fluid. The film is subsequently dried, resulting in a thin, solid film. This is the most common synthesis method for large-area perovskite films. It has been employed in multiple PSC investigations to create high-performance cells with surface areas greater than 10 cm^2 . Different investigations have shown that by adjusting the processing temperature, the quality of the perovskite film can be improved [187]. Recent work has focused on using additives to produce thick perovskite films with uniform crystal shapes and fewer pinholes [188]. For perovskite films [189,190], and more recently for perovskite PVs with a 20% scalable solution technique [190,191], blade coating has been widely employed as a single-step deposition approach.

This technique was employed by Razza et al. to construct a PSC module that had an active area of 10.1 cm² and a PCE of 10.4% [192]. By inserting a nitrogen knife after a predetermined distance and applying a nitrogen flow, Huang et al. accelerated liquid-layer drying at room temperature. As a result of this breakthrough, a verified PSC module was created with an effective area of 63.7 cm² and a PCE of 16.4% [193]. An average efficiency of 20.49% was reached by a PbI₂-TBP-PS device made using a two-step sequential blade-coating process [194].

3.3.5. Slot-Die Coating Method

In slot-die coating, ink is measured using a microfluidic metal die machine. The machine-structured die features a narrow channel for ink distribution across a revolving substrate [176]. The surface is often composed of a bendable substrate, such as plastic. To prevent the fluid in the head from being affected by gravity and to keep wet film formation under control during high-speed coating, the head is typically positioned horizontally on a roller. The head is arranged in a vertical position on top of a glass substrate or other surface that is flattened. The formation of the wet film is determined by the geometry, web velocities, and fluid feeding rate. Coating procedures are, consequently, geometry- and microfluidics-dependent, as well as dependent on the thickness, chemistry, and microfluidic boundary conditions of the wet film [195]. Due to the lack of viscosity and low boiling point, which is the result of completely enclosed environmental deposition, slot-die coating is usually a preferred approach in the organic PV community. It is possible to reduce composition changes brought on by solvent evaporation loss. Using a thin slit in an ink reservoir, slot-die coating can uniformly spread ink across a substrate while allowing for precise regulation of film thickness [196]. The authors in [197] employed this method, which is suitable for roll-to-roll manufacturing and potentially for large-scale commercialization, and obtained an average power PCE of 15.57%.

3.4. Challenges towards Commercialization

Even though PSCs have achieved great efficiency, the key hurdle in commercializing this technology is producing large-area cells with stability similar to that of traditional inorganic solar cells. A significant barrier to commercialization is the perovskite layer stability. Solar cells are typically used in tough environments with regularly changing weather, including high humidity, high temperatures, and full solar spectrum. PSCs, on the other hand, have a relatively limited lifespan due to the instability of the perovskite layer under high humidity conditions, limiting its usage in outdoor applications. Prior to scaling up PSC manufacture and commercialization, it is important to evaluate the cost and reliability of the operating process.

4. Quantum Dot Solar Cells

A quantum dot (QD) is a semiconductor nanoparticle with a diameter of a few nanometers [198], typically 2 to 10 nm [199], exhibiting electrical and optical characteristics that are distinct from those of bigger particles. A quantum-dot solar cell (QDSC) is a type of solar cell in which QDs are used as the light absorbing material [200]. An effort is made to swap bulk components such as silicon, cadmium telluride (CdTe), or copper indium gallium selenide (CIGS). By varying their size, QDs bandgaps may be made programmable across a broad range of energy levels, while the band gap in bulk materials is determined by the substance being used [201]. Due to this feature, QDs are appealing for multi-junction solar cells, which utilize a range of materials to increase efficiency by collecting several regions of the solar spectrum.

In this section, we mainly focus on QD sensitized solar cells (QDSSC) due to their high conversion efficiency capability. We discuss the basic configuration and working mechanism in this section. Moreover, the factors that affect the stability of these cells, which is a significant barrier to commercialization of this technology, are highlighted. Progress in terms of efficiency using different configurations such as using different types

of photoanodes and QD sensitizers, the applications of QD in PSC, and challenges in QDSSC are also discussed.

In recent years, there has been an increase in research interest in QDSSCs on a world-wide scale, attracting researchers from several fields. These researchers include (1) physicists who are developing novel materials for QDSSC manufacturing and investigating the photophysical process of QDSSCs; (2) chemists who are producing appropriate light-harvesting materials; and (3) engineers who are creating unique device designs for QDSSCs. Future breakthroughs in QDSSCs could be made more likely with a synergy between these efforts [18]. High-performance solar cells need materials that can effectively convert light into electricity as well as materials that can effectively capture a broad spectrum of solar energy. The use of QDSSCs can offer several advantages, including greater charge creation, charge separation, and charge extraction within the same material, making them excellent candidates for future solar cells [202,203]. Typically, the charge creation process occurs in QDs, and the charge is quickly transported into two separate transport mediums, reducing the electron–hole recombination process.

The first QDSC was created in 2010 by Luther et al. [204] using a bilayer of PbS/ZnO QDs, which exhibited good stability and an efficiency of 2.94%. To increase the efficiency of QDSSCs, researchers have used a range of quantum dot materials. Hao et al. [205] achieved a 16.6% efficient DSSC by using perovskite QD materials; this was the highest recorded efficiency for DSSC until 2020, when UNIST achieved an efficiency of 18.1%, according to the latest NREL update (The evolution of the efficiencies of solar cells with time is available from The National Renewable Energy Laboratory (NREL) Best research-cell efficiency chart. “<https://www.nrel.gov/pv/cell-efficiency.html> (accessed on 9 January 2023)”). According to the Shockley–Queisser model, this still falls short of the 30% theoretically achievable efficiency limit [206]. Several reviews on QDSCs have been published in recent years, with the majority of them focusing on device characterization, manufacturing methodologies, and component optimization [207].

QDSCs are an improved form of DSSCs in which dye-sensitized materials are substituted by different QD materials. Transparent conducting oxides (TCO), a semiconducting wide-bandgap mesoporous material for the photoanode, an electrolyte with a redox couple, a counter electrode (CE), and QDs as a sensitizer are the components of QDSCs. Figure 6 shows a schematic of the architecture of a QDSC.

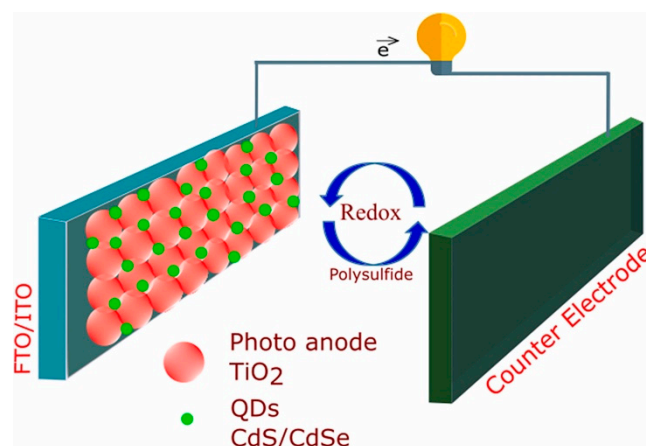


Figure 6. Schematic of a QDSC [200]. Reproduced with permission from J.H. Markana et al., *Dyes and Pigments*, Elsevier, 2022.

4.1. Working Principles of a QDSSC

The working of QDSSCs consists of the following major steps (illustrated in Figure 6, with charge transfer illustrated in Figure 7).

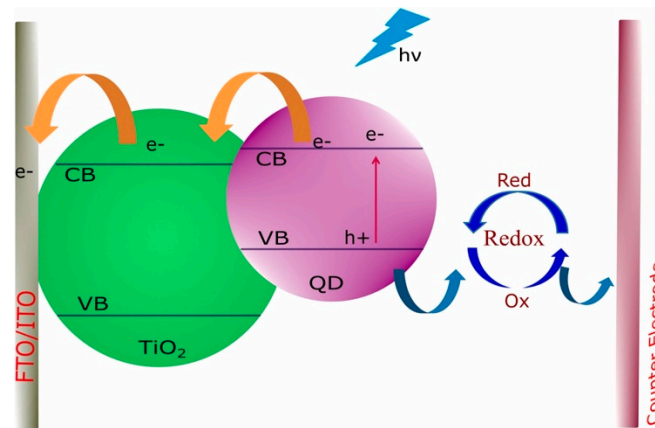
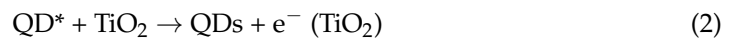


Figure 7. Illustration of charge transfer in a QDSC [200]. Reproduced with permission from Markana et al., *Dyes and Pigments*, Elsevier, 2022.

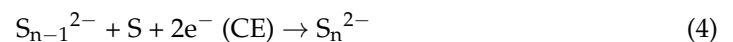
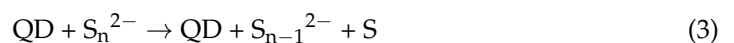
Charge-separation. QDs are used as light absorbing materials in QSSC which by exposure to sunlight create electron–hole pairs, also called the charge-separation process presented in Equation (1).



Electron injection. Secondly, these newly generated electrons and holes are then transferred to their respective ends/terminals, i.e., electrons are transferred into the semiconductor metal oxide (acting as an electron acceptor) while the holes are moved to the electrolyte or CE. The CE could be either metal or semiconductor electrodes with greater catalytic activity toward the redox couple (e.g., Au or Pt) accepting holes from the QDs. Meanwhile, electrons in the metal oxide are transferred to a transparent conductive oxide substrate and then to the CE (Equation (2)).



Hole injection. The electrolyte, which mainly consists of a reversible redox couple, receives holes from the QDs. A polysulfide electrolyte with a reversible redox couple $\text{S}_n^{2-}/\text{S}^{2-}$ is typically used for QDSSC operation.



Diffusion of polysulfide redox couple. Subsequently, the electrons in the electrolyte are collected by the oxidized S_n^{2-} and are converted to S^{2-} . This process is called the diffusion process or redox reaction.



Currently, despite significant advancements in QDSSCs, the issue of reduced device performance stability has yet to be successfully addressed. The key factor prohibiting QDSSCs devices from being used on a large scale is their difficulty in maintaining stability. Aside from environmental stabilities (light, moisture, and oxygen in the atmosphere), the most difficult hurdles to overcome in the future are intrinsic and component stabilities, which include photochemical instability of QDs, as well as degradation of the adhesive materials and sealing. Other issues include the substrate type, the electrocatalytic activity of the CE material, and evaporation or volatilization of the electrolyte.

4.2. Developments in the Efficiency of QDSSCs

4.2.1. Based on the Photoanode

TiO₂ [208,209], SnO₂ [210], ZnO [211], NiO [212], BaSnO₃ [213], Nb₂O₅ [214], and other wide bandgap semiconducting metal oxides are employed as photoanodes, which serve to create excitons by absorbing photons and transporting electrons to the counter electrode. The photoanode is placed on a TCO substrate, which is transparent, has low resistance, and can withstand high temperatures, all of which contribute towards the efficiency of these solar cells [213,215]. To further improve the efficiency of QDSSCs, attempts have been made to employ other materials, doping, surface modification, and composite arrangements, amongst other modifications. Nevertheless, TiO₂ remains a strong candidate when compared to other materials and arrangements. Archana et al. [216] and Maiti et al. [215,217] developed a QDSSC using TiO₂ as the photoanode, with CdS and CdSe as a sensitizer, achieving efficiencies of 0.75% and 5.01%, respectively. An extensive amount of research has been conducted by various research groups, as summarized in Table 6.

Table 6. Photovoltaic parameters of QDSSCs based on different photoanodes.

Photoanodes	Sensitizer	V _{OC} (V)	J _{SC} (mA/cm ²)	FF	η (%)	Refs.
TiO ₂	CdS	0.37	6.24	0.33	0.75	[216]
TiO ₂	CdSeS	0.68	16.8	0.44	5.01	[217]
TiO ₂	ZClSe	0.59	11.58	0.63	4.25	[218]
TiO ₂	CdS/CdSe	0.53	12.5	0.60	3.96	[219]
TiO ₂	CdSe/CdS	0.62	14.4	0.49	4.41	[220]
TiO ₂	CdS/CdSe	0.56	16.1	0.337	3.06	[221]
TiO ₂	CsPbI ₃	1.20	14.37	0.78	13.4	[222]
TiO ₂	PbS	0.59	8.92	0.56	2.94	[204]
TiO ₂	PbS	0.52	18.14	0.46	4.4	[223]
TiO ₂	PbSe	0.52	23.4	0.52	6.2	[224]
TiO ₂	PbSe	0.53	24	0.51	6.47	[225]
TiO ₂	CdS/CdSe: Mn (2%)	0.56	20.7	0.47	5.42	[226]
TiO ₂	CdS: Graphene (1.6%)	0.54	5.9	0.38	1.2	[227]
TiO ₂ NF	CdSe	0.42	9.21	0.56	2.15	[228]
TiO ₂ NFs	CZTSe	0.47	13.65	0.56	3.61	[229]
TiO ₂ NFs	Ag ₂ Se	0.41	11.12	0.55	2.5	[230]
TiO ₂ /C- TiO ₂ /TiO ₂	CdS	0.27	4.80	0.13	0.17	[208]
TiO ₂ /QD/TiCl ₄	CdSeTe	0.70	20.69	0.62	9.01	[231]
TiO ₂ /ZnO NR why different?	CdS	0.41	2.37	0.35	0.33	[232]
TiO ₂ /ZnO NR	CdS	0.48	13.34	0.42	2.71	
TiO ₂ : B/S ^a co-doped	CdS	1.22	3.35	0.88	3.60	[233]
TiO ₂ :TiCl ₄	CdSe	0.56	15.54	0.61	5.53	[234]
TiO ₂ wth SrTiO ₃ (10%)	CdS	0.60	6	0.48	1.80	[235]
N doped TiO ₂	CdS	0.84	10.40	0.53	4.58	[236]
P- TiO ₂ NF	Cu ₂ AgInSe ₄ (CAISe)	0.52	12.86	0.63	4.24	[237]
BaTiO ₃	CdS	0.61	3.74	0.56	1.26	[238]
NiO	CuInS _x Se _{2-x} :Zn ⁺²	0.35	9.13	0.39	1.25	[211]
SnO ₂	CdS	0.45	1.47	0.34	0.22	[210]

Table 6. Cont.

Photoanodes	Sensitizer	V_{OC} (V)	J_{SC} (mA/cm ²)	FF	η (%)	Refs.
SnO ₂ NF	CdS	0.61	11.56	0.43	3	[239]
SnO ₂ with TiCl ₄	PbS/CdS	0.30	19.12	0.28	1.60	[240]
ZnO	CdS/CdSe	0.67	4.77	0.39	1.26	[241]
ZnO	PbS-TBAI /PbS-EDT	24.2	0.55	0.64	8.55	[242]
ZnO	CdS/CdSe	0.61	9.93	0.52	3.14	[243]
ZnO	CdS/CdSe	0.68	10.48	0.62	4.46	[244]
ZnO (Al doped)	CdS/CdSe	0.60	12.86	0.69	5.32	[209]
ZnO NP	CdS/CdSe	0.50	15.40	0.44	3.35	[245]
ZnO/TiO ₂	CdS	0.46	7.80	0.68	2.44	[246]
ZnTi	CdS	0.63	10.14	0.61	3.92	[247]
ZnTiO ₃	CdS/CdSe	0.59	5.96	0.56	1.95	[248]

Sanehira et al. [222] developed a QDSC using CsPI₃ as a sensitizer, based on AX (A-site cation halide salt) treatments to improve the electronic coupling between perovskite QDs. The authors used a variety of AX salts such as FAI, FABr, MAI, CsI, and Neat EtoAc and recorded different solar cell performance parameters, observing that among the mentioned AX salts, FAI performed well and recorded the highest efficiency of 13.43%. This suggests that various AX salt treatments can affect the coupling between QDs and can be used for tuning the electronic properties of QD films. Ren et al. [231] made efforts to lower the rate of recombination in an electrode, one of the key factors responsible for lowering the PCE of a cell. The authors used a unique and very simple approach to inhibit charge recombination by coating electrodes combined with a blocking layer, ZnS/SiO₂. The exposed surface of TiO₂ particles and QDs are modified with an amorphous TiO₂ layer using a classical TiCl₄ hydrolysis procedure to improve the effectiveness of a ZnS/SiO₂ barrier layer. This strategy makes it possible to achieve a 9.01% efficient CdSeTe-based QD solar cell. In [232], TiO₂ NAs were synthesized using anodic oxidation, and the TiO₂/ZnO nanocomposite was obtained through a hydrothermal reaction. The SILAR method was used to create TiO₂/ZnO/CdS photoanodes as the photoelectrode. The TiO₂/ZnO photoanode yielded excellent interfacial charge separation. As the SILAR cycle number of CdS increased from 2 to 10, a clear upward and downward trend in QDSSC efficiency with TiO₂/ZnO/CdS photoanodes can be seen. For 3 and 6 h, the recorded efficiencies were 0.33% and 2.71%, respectively, as highlighted in Table 6.

A promising method for achieving low-cost, large-area, flexible, and lightweight photovoltaic systems with quick energy payback times and high specific power is solution processing. However, the organic, inorganic, and hybrid solution-processed materials used in solar cells reported up to this point typically have poor air stability, require processing in an inert atmosphere, or require processing at high temperatures, all of which add to the complexity and cost of manufacturing. The development of room-temperature solution-processed ZnO/PbS quantum dot (QD) solar cells offer a potential answer to the technical difficulty of simultaneously achieving the requirements of low-temperature fabrication conditions, high efficiency, and good atmospheric stability. A verified efficiency of 8.55% has been achieved by Chuang et al. by modifying the band alignment of the QD layers using various ligand treatments [242]. TiO₂, SnO₂, ZnO, NiO, BaSnO₃, Nb₂O₅, and other wide bandgap semiconducting metal oxides are employed as photoanodes, which serve to create excitons by absorbing photons and transporting electrons to the counter electrode.

4.2.2. Based on QD Sensitizers

QD sensitizers are one of the most important components of QDSSCs, responsible not only for absorbing photons from sunlight but also transferring the excited electrons into the CB of a material. QD sensitizers must possess certain qualities to increase the QDSC efficiency, including a high absorption coefficient to absorb photons from a wide spectrum, an appropriate energy bandgap, rapid electron transfers, a simple production process, low cost, good stability and durability, and not to mention low toxicity.

In order to capture a significant amount of light, commonly used materials for QD sensitizers are CdTe [249], PbSe [250], InP [251], ZnSe [252], CdS, CdSe [253], PbS [254,255], Ag₂S [256], Bi₂S₃ [257], CuInS₂ [258], InAs [259], and CuBiS₂ [260]. Furthermore, combinations of different QDs, such as Cd_{1-x}Zn_xZTe/CdS [261], Ag₂S/ZnS [262], Bi₂S₃/Sb₂S₃ [263], CdTe/CdTeSe/CdSe [264], CdS/PbS [253,265], CdS/CdSe [253,266], CdS/CdTe [267], and InP/ZnS [268] have shown impressive performance for the light absorption purposes. In order to obtain an efficient solar cell, different research groups used different types of QD sensitizers, mostly with TiO₂-based photoanodes, with the recorded efficiencies listed in Table 7.

Table 7. Efficiency details of QDSCs based on different QDs.

QD Sensitizer	Photoanode	Counter Electrodes	η (%)	Refs.
CdSe/CdS	TiO ₂	Au	4.8	[269]
CdSe	TiO ₂ -SeO ₂	CoS ₂	3.45	[270]
PbS/CdS/CdSe	TiO ₂	CuS	4.58	[271]
CdSe	TiO ₂	Cu ₂ S	2	[272]
CdSe	TiO ₂	Pt-coated FTO	1.7	[273]
CdSe	TiO ₂ : Mg ⁺²	Cu ₂ S/brass	6.9	[274]
Zn-Cu-In-Se (ZCISE)	TiO ₂ : Mg ⁺²	Cu ₂ S/brass	9.02	
CdS	TiO ₂	CuS/PbS	1.13	
PbS/CdS	TiO ₂	CuS/PbS	1.84	[253]
CdSe	TiO ₂	CuS/PbS	2.84	
CdS/CdSe	TiO ₂	CuS/PbS	3.63	
CdTe/CdS	TiO ₂	CuSNP	2.5	[249]
PbS CQD with PBDB-T(F)	ZnO	MoO ₃ /Ag	11.2	[255]
PbSE CQD	SnO ₂	Au	10.4	[250]
CIS-CuInS ₂	TiO ₂	Au	0.75	[258]
CdS-Bi ₂ S ₃	TiO ₂	CuI	1.01	[257]
CuBiS ₂	TiO ₂	Cu ₂ S	0.62	[260]
CdS/CdSe	ZnTi MMO	Cu ₂ S	2.85	[266]
CdS/Ag ₂ S-ZnS	TiO ₂	CuS	3	[262]
Bi ₂ S ₃ /Sb ₂ S ₃	TiO ₂	Pt	0.67	[263]
ZnS coated InP	TiO ₂	Brass	0.351	[268]
Cd _{1-x} Zn _x Te/CdS	TiO ₂	Cu ₂ S	3.27	[261]
Co ⁺² (3%) doped CdS	TiO ₂	Pt	1.21	[275]
Mn ⁺² doped CdS	ZnO	Al	2.09	[276]
PbS:Hg	TiO ₂ (NP/NF)	Cu ₂ S	4.72	[277]
CdSe:Ag ⁺	TiO ₂	Cu ₂ S	2.72	[278]

Table 7. Cont.

QD Sensitizer	Photoanode	Counter Electrodes	η (%)	Refs.
Cu–CdS	TiO ₂	Pt	1.04	[279]
In–CdS	TiO ₂	Pt	0.65	
Mg-doped CdSe	TiO ₂	Pt-ITO	0.67	[280]
CdS/CdSe	TiO ₂ (NCs)	CuS	6.80	[281]
CdS/CdSe	TiO ₂	CuS	5.07	[282]
PbS	ZnO	Au	9.40	[283]
Gradient-band-gap PbS	TiO ₂	–	4.08	[284]
CdS	TiO ₂	Au	0.80	[285]
CdS/CdSe/ZnS	TiO ₂	CoO	6.02	[286]
CdTe/CdS	TiO ₂	Cu ₂ S	2.44	[287]
CIS-Z and (CuInS ₂ (CIS) QDs)	TiO ₂	Cu ₂ S on brass foil	7.04	[288]
CIS	TiO ₂	Cu ₂ S on brass foil	5.05	
CuInSe _x S _{2-x}	TiO ₂	CuS	5.51	[289]
ZCISe	TiO ₂	MC/Ti	12.65	[290]
ZCISe/ZnSe	TiO ₂	MC/Ti	13.84	
CISe	TiO ₂	Cu ₂ S/brass	7.56	[291]
CIGSe	TiO ₂	Cu ₂ S/brass	9.30	
CISe	TiO ₂	MC/Ti	9.18	
CIGSe	TiO ₂	MC/Ti	11.30	
Cu ₂ ZnSnS ₄ (CZTS)	TiO ₂	Cu ₂ S	3.29	[292]
CAIS(Cu ₂ AgInS ₄)	TiO ₂	Cu ₂ S/FTO	4.89	[293]
ZCISe	TiO ₂	–	14.70	[294]
N ₂ -CQDs	TiO ₂	Pt	0.45	[295]
CAISe (Cu ₂ AgInSe ₄)	TiO ₂	Cu ₂ S	4.24	[236]

Xue et al. [255] suggested different conjugated polymers such as PBDB-T, PBDB-T(s), PBDB-T(F), and PBDB-T(S) as HTMs in PbS CQD solar cells. The authors adjusted energy levels, optimized solid-state ordering, and improved hole mobility and carrier density by optimizing PBTB-T model polymers through side-chain engineering. Using modified PBDB-T(F) polymers in CQD solar cells, an 11.2% efficiency was recorded. The photovoltaic performance of the resulting QDSCs is influenced greatly by the crystalline quality and intrinsic electronic structure of the QD light-harvesting materials. Undoubtedly, one of the most effective ways to raise the efficiency of QDSCs is to utilize suitable, high-quality QDs. In [290] Zn-Cu-In-Selenide (ZCISe) alloy QDs are surrounded by a ZnSe shell layer with a larger bandgap, creating a type-I core/shell structure that helps to lower the trap state defect density. The average power conversion efficiency (PCE) of QDSCs was increased through this QD material engineering from 9.54%, which corresponds to pure CuInSe₂, to 12.65% and 13.84% for ZCISe and ZCISe/ZnSe QDs, respectively.

To increase the photoelectronic conversion, Peng et al. [291] used CIGSe QDs as sensitizers in QDSSCs, possessing a light-harvesting range of up to 1000 nm. Through multiple tests such as X-ray photoelectron spectroscopy and X-ray diffraction, the authors confirmed that the guest Ga element is alloyed in the host CISe, which fits well with the TiO₂ substrate and can optimize the electronic structure of CIGSe QDs, lowering the intrinsic recombination in CIGSe QDSCs. As a result, mesoporous carbon counter electrodes supported with titanium mesh used in CIGSe-based QDSCs achieved an efficiency of

11.49%. Similarly, Song et al. [294] designed a ZCISSe-alloy QD-based QDSC and achieved 14.70% efficiency.

4.3. Application of QD in PSCs

PSCs have a lower environmental stability than that of conventional Silicon-based cells [296]. The difference in energy level and hysteresis effects in PSC not only affect the charge transportation but also its photovoltaic properties [297–299]. Enhancing PSC performance has been a focus of academic research for the last decade. QDs having outstanding properties, helping to enhance the electron and hole transportation and also optimizing the energy level arrangement within PSCs [300–302]. As a result, QDs are seen as viable materials for optimizing PSCs. Below, we examine the role of QDs in PSCs as additives for ETLs and HTLs, discussing different ETMs and HTMs as well as associated issues.

4.3.1. QDs as Additives in ETLs

The ETL collects and transfers electrons to the conductive glass while successfully inhibiting the recombination of holes. The following attributes should be present in an ideal ETM:

(1) Proper arrangement of energy levels for effective electron extraction.

(2) High electron mobility for quicker transmission of electrons to external circuits. Unfortunately, electron transport and extraction in PSC ETLs are not optimal, exhibiting instability and hysteresis.

The use of various types of QDs in ETLs provided an efficient way of optimizing the ETM. To reduce the UV-induced degradation of perovskite films, Jin et al. [303] added CQDs to the mesoporous TiO₂ layer via a modified hydrothermal technique. CQDs considerably improved the light stability of PSCs by efficiently converting UV light into blue light, achieving 16.40% efficiency. Apart from CQDs, various research groups have used different types of QDs such as GQDs and CdSeQD to improve the performance. Notable results on the use of these QDs as additives in ETLs are summarized in Table 8.

Table 8. Details of QDs as additives in ETLs.

QDs	Device Structure	V _{OC} (V)	J _{SC} (mA cm ⁻²)	FF (%)	η (%)	Refs.
CQDs	FTO/c-TiO ₂ /m-TiO ₂ :CQDs/MAPbCl _x I _{3-x} /Spiro-OMeTAD/Au	1.02	22.64	71.6	16.40	[303]
CQDs	ITO/TiO ₂ :CQDs/MAPbI ₃ Cl _{3-x} /Spiro-OMeTAD/Au	1.14	21.36	78	18.89	[304]
CQDs	FTO/PEDOT:PSS/MAPbI ₃ /PCBM:CQDs/BCP/Ag	0.97	22.30	79.6	18.10	[305]
g-C ₃ N ₄ QDs	ITO/SnO ₂ :g-C ₃ N ₄ QDs/CsFAMA/Spiro-OMeTAD/Au	1.18	24.03	78.3	22.13	[306]
Red CQDs	ITO/SnO ₂ :RCQs/Cs _{0.05} FA _{0.81} MA _{0.14} PbI _{2.25} Br _{0.45} /Spiro-OMeTAD/MoO ₃ /Au	1.14	24.1	82.9	22.77	[307]
GQDs	FTO/Au/SnO ₂ :GQDs/ZnO/Perovskite/Spiro-OMeTAD/Au	1.17	22.85	74	19.81	[308]
GQDs	ITO/SnO ₂ :GQDs/MAPbI ₃ /Spiro-OMeTAD/Au	1.13	23.05	78	20.31	[309]
GQDs	FTO/SnO ₂ :GQDs/CsFAMA/Spiro-OMeTAD/Ag	1.10	21.62	78	18.55	[310]
GQDs	ITO/c-TiO ₂ /m-TiO ₂ :GQDs/Cs _{0.05} (MA _{0.17} FA _{0.83}) _{0.95} Pb(I _{0.83} Br _{0.17}) ₃ /Spiro-OMeTAD/Au	0.97	21.92	67	14.36	[311]
GQDs	ITO/PCBM:GQDs/MAPbI ₃ /Spiro-OMeTAD/Au	1.09	22.03	73	17.56	[312]
GQDs	ITO/SnO ₂ :GQDs/MAFAPbI _x Cl _{3-x} /Spiro-OMeTAD/Ag	1.11	24.40	78	21.10	[313]

Table 8. Cont.

QDs	Device Structure	V _{OC} (V)	J _{SC} (mA cm ⁻²)	FF (%)	η (%)	Refs.
QDs	FTO/c-TiO ₂ /m-TiO ₂ :GQDs/Perovskite/Spiro-OMeTAD/Ag	1.08	24.92	76	20.45	[314]
GQDs	FTO/SnO ₂ :GQDs/CsFAMA/Spiro-OMeTAD/Au	1.08	23.5	77	19.6	[315]
CdSe QDs	ITO/PEDOT:PSS/CH ₃ NH ₃ PbI _{3-x} Cl _x /PCBM:CdSe QDs/LiF/Ag	0.90	20.96	73.16	13.73	[316]
CdS QDs	FTO/TiO ₂ :CdS QDs/CH ₃ NH ₃ PbI ₃ /Spiro-OMeTAD/Au	0.94	16.7	64	10.52	[317]
PbS QDs	FTO/TNTs:PbS QDs/Cs _{0.05} (FA _{0.85} MA _{0.15}) _{0.95} Pb(I _{0.85} Br _{0.15}) ₃ /Spiro-OMeTAD/Au	1.14	23.38	56.03	14.95	[318]
PbS QDs	ITO/ZnO:PbS QDs-TBAI-80/MAPbI ₃ /PCBM/Ag	1.14	22.80	78.99	20.53	[319]
BP QDs	Glass/FTO/SnO ₂ :BP QDs/BP QDs@A-CsFAMA/Spiro-OMeTAD/Ag	1.22	23.53	79.6	22.85	[320]
BP QDs	FTO/SnO ₂ :BP QDs/(FAPbI ₃) _{0.97} (MAPbBr ₃) _{0.03} /Spiro-OMeTAD/Ag	1.13	24.4	76.1	21.0	[321]
SnO ₂ QDs	FTO/c-TiO ₂ /m-TiO ₂ :SnO ₂ QDs/MAPbI ₃ /Spiro-OMeTAD/Ag	1.13	22.36	75.67	19.09	[322]

A TiO₂ ETL has low electron mobility, oxygen vacancies, and high photocatalytic activity towards perovskite material. To resolve this issue, Zhou et al. [322] successfully demonstrated SnO₂ QDs and modified m-TiO₂ (mesoporous-TiO₂)-based ETLs for PSCs. It was observed that with the use of the newly constructed ETL, not only did electron extraction improve, but charge recombination was also lowered, resulting in an increase in the conductivity of the ETL and enhancing the overall PCE, achieving 19.09% efficiency. Gu et al. [321] used black phosphorus (BP) QDs combined with SnO₂ nanoparticles, which can improve the performance of SnO₂-based ETL. The authors used SnO₂/BPQD alloy-based ETL for PSC and achieved an efficiency of 21%. Zhang et al. [320] incorporated BPQDs into both the ETL and perovskite layers using a layer optimization technique. To increase the electron mobility of SnO₂, its electron traps are effectively filled by the doping of BPQDs, which have a higher conductivity. At the same time, 3-aminopropyltriethoxysilane-modified BPQDs were introduced into the perovskite bulk to moderately tailor its intrinsic characteristics, which simultaneously promotes the perovskite nucleation and growth, passivates defects, and enhances the moisture-resistance of the perovskite film. By capitalizing on these synergistic effects, a power conversion efficiency of up to 22.85% was attained.

In [313], Pang et al. enriched the SnO₂ ETL with the Graphene (G) QDs. Using SnO₂ and GQDs together, the authors were able to achieve a PCE of 21.1%. The PCE of SnO₂/GQDs-based devices is significantly higher than that of SnO₂-only ETL devices (18.6%) and provides a more stable performance. To increase the electron extraction and carrier separation, an efficient ETL plays a very important role. In [307], an efficient composite ETL was constructed by doping low-temperature solution-processed SnO₂ with red-carbon quantum dots (RCQs), which greatly boosts electron mobility by a factor of around 20, enhancing long-term stability against humidified environments and increasing the efficiency to 22.77%. The use of various nano-particles (TiO₂, SnO₂, ZnO, etc.) with different QDs such as CdS, PbS, CdSe, G, BP, and RC is under active investigation and provides a promising route to highly efficient and stable PSC devices, though whether the resulting devices can be manufactured at low costs and in bulk will be determined by the materials used and the preparation methods.

4.3.2. QDs as Additives in HTLs

In PSCs, the HTL extracts, collects, and transports the holes to the metal electrode, while preventing electron injection. It has a significant impact on PSC photoelectric performance and stability. It should thus have good cavity transport. To reduce energy barriers,

the ideal HTL should have a HOMO energy level that is consistent with the energy level of the valence band edge of perovskites. Various research groups used different types of QD as additives in HTLs with different PSC structures and recorded various cell performance parameters. Table 9 provides a summary of significant results for QDs as additives in HTL.

Table 9. Details of QDs as additives in HTLs.

QDs	Device Structure	V _{OC} (V)	J _{sc} (mA cm ⁻²)	FF (%)	η (%)	Refs.
CQDs	FTO/SnO ₂ /(FAPbI ₃) _{0.95} (MAPbBr ₃) _{0.05} /Spiro-OMeTAD:GQDs/Ag	1.06	24.17	79.41	20.41	[323]
CQDs	ITO/GO:CQDs/CH ₃ NH ₃ PbI ₃ /PCBM/BCP/Ag	0.95	21.0	80.1	16.2	[324]
CQDs	ITO/NiO:CQDs/CH ₃ NH ₃ PbI ₃ /PCBM/BCP/Ag	1.08	20.22	77.15	16.91	[325]
GQDs	FTO/PEDOT:PSS/GQDs/CH ₃ NH ₃ PbI ₃ /PCBM/BCP/Ag	1.00	21.41	75.31	16.16	[326]
AGQDs	ITO/NiO:AGQDs/(FA _{0.83} MA _{0.17}) _{0.95} Cs _{0.05} Pb(I _{0.9} Br _{0.1}) ₃ /PCBM/BCP/Ag	1.07	22.5	81.5	19.55	[327]
Graphdiyne QDs	FTO/TiO ₂ /GD QDs/CH ₃ NH ₃ PbI ₃ :GD QDs/Spiro-OMeTAD:GD QDs/Au	1.12	22.48	78.7	19.89	[328]
Graphdiyne QDs	FTO/TiO ₂ /CH ₃ NH ₃ PbI ₃ /P3HT:GD QDs/Au	0.94	21.7	71.3	14.58	[329]
PbSO ₄ (PbO) ₄ QDs	ITO/SnO ₂ /CsFAMA/Spiro-OMeTAD:PbSO ₄ (PbO) ₄ QDs/Au	1.14	24.80	80	22.66	[330]

To overcome the deficiencies in Spiro-OMeTAD (one of the most widely used HTMs in PSC) such as poor long-term conductivity, little room for improvement in PCE, stability, and moisture absorption, Zheng et al. [330] incorporated the inorganic salt PbSO₄(PbO)₄ QDs in the Spiro-OMeTAD to form the HTL and observed that the long-term conductivity and moisture stability (up to 50 days at room temperature) were greatly improved. As a result of improved conductivity and lower charge recombination, the PSC achieved an efficiency of 22.66%. In [328], Xisheng et al. used Graphdiyne (G) QDs in PSC as a dopant to TiO₂, Spiro-OMeTAD, and CH₃NH₃PbI₃ to improve carrier transport and overall performance. The presence of GQDs on the TiO₂ surface offered several advantages: improving the fill factor and current density through enlarging/enhancing the perovskite grain size, lowering charge recombination to obtain a high Voc, and increasing the device stability by improving hydrophobicity in the Spiro-OMeTAD film. As a result, the PCE was increased to 19.89%.

To develop efficient and flexible PSCs, Wang et al. [327] introduced a technique for tuning a NiO_x ETL by using Amino-functionalized graphene (G) QDs. The NiO_x film uses AGQDs as a multipurpose additive. Firstly, adding AGQDs provides a large number of N atoms to the improved NiO_x layer surface, which can enhance the crystallization of the perovskite film through Lewis base-acid interaction. Secondly, the AGQDs can improve the band structure alignment between the NiO_x and perovskite layers, which enhances hole harvesting at the NiO_x/perovskite interface. This resulted in a high PCE of 19.55% for the inverted PSCs. In [323], Liu et al. used carbon (C) QDs to modify a Spiro-OMeTAD-based HTL, exhibiting outstanding characteristics, such as a low charge recombination, passivated interfacial trap states, and appropriate energy levels for hole extraction. By using the modified HTL, a 20.41% efficient PSC was developed.

By varying the QD size, bandgaps can be made programmable across a broad range of energy levels, while the band gap in bulk materials is determined by the substance being used. Due to this feature, QDs are appealing for multi-junction solar cells, which utilize a range of materials to increase efficiency by collecting several regions of the solar spectrum.

4.3.3. QDs as ETMs

In addition to being employed as additives, QDs can be utilized as ETMs and HTMs. Researchers are currently using metal oxide QDs as ETMs for PSCs since they have superior qualities compared to conventional metal oxide materials. QDs have been used as ETMs for different PSC structures, and different cell performance parameters have been recorded.

Ameen et al. [331] used ZnO QDs, recording an efficiency of 9.73%, which was low but set the future direction for QDs. Tavakoli et al. [332] prepared ZnO/rGO QDs with a special core shell structure, improving the PCE to 15.2%. Further notable research has been carried out by different research groups using various QDs as ETMs, as summarized in Table 10.

Table 10. Details of QDs as ETMs.

QDs	Device Structure	V_{OC} (V)	J_{SC} (mA cm^{-2})	FF (%)	η (%)	Refs.
ZnO QDs	ITO-PET/Graphene/ZnO QDs (Apjet)/ $\text{CH}_3\text{NH}_3\text{PbI}_3$ /Spiro-OMeTAD/Ag	0.94	16.80	62	9.73	[331]
ZnO/rGO QDs	FTO/ZnO/rGO QDs/ $\text{CH}_3\text{NH}_3\text{PbI}_3$ /Spiro-OMeTAD/Au	1.03	21.7	68	15.2	[332]
TiO ₂ QDs	FTO/TiO ₂ QDs/m-TiO ₂ / $\text{CH}_3\text{NH}_3\text{PbI}_3$ /Spiro-OMeTAD/Au	1.06	22.48	71	16.97	[333]
SnO ₂ QDs	ITO/SnO ₂ QDs/MAPbI ₃ /Spiro-OMeTAD/Ag	1.08	21.85	74.28	17.66	[334]
SnO ₂ QDs	FTO/SnO ₂ QDs/ $\text{MA}_{0.7}\text{FA}_{0.3}\text{PbI}_3$ /Spiro-OMeTAD/Au	1.08	23.40	74	20.1	[335]
SnO ₂ QDs	FTO/Al:SnO ₂ QDs/MAPbI ₃ /Spiro-OMeTAD/Ag	1.06	22.78	75.41	18.20	[336]
SnO ₂ QDs	FTO/SnO ₂ QDs/ $\text{Cs}_{0.05}(\text{MA}_{0.17}\text{FA}_{0.83})_{0.95}\text{Pb}(\text{I}_{0.83}\text{Br}_{0.17})_3$ /Spiro-OMeTAD/Ag	1.13	23.05	79.8	20.79	[337]
SnO ₂ QDs	ITO/SnO ₂ QDs/MAPbI ₃ /Li-doped Spiro-OMeTAD/Au	1.12	21.61	77	18.71	[338]
SnO ₂ QDs	ITO/SnO ₂ QDs/ $\text{Cs}_{0.05}\text{FA}_{0.81}\text{MA}_{0.14}\text{PbI}_{2.25}\text{Br}_{0.45}$ /Spiro-OMeTAD/Carbon	1.08	22.19	56.64	13.64	[339]
BP QDs	ITO-PEN/BP QDs/ $\text{FA}_{0.85}\text{MA}_{0.15}\text{PbI}_{0.25}\text{Br}_{0.5}$ /Spiro-OMeTAD/Au	1.03	16.77	65.2	11.26	[340]

Hole and electron transmitting materials can greatly affect the efficiency of a PSC. To control the carrier concentration of a SnO₂ QD ETL and achieve a higher PCE, Yang et al. [337] introduced a two-step mechanism: room temperature colloidal synthesis and a lower temperature removal of the additive. Through optimizing the electron density of a SnO₂ ETL, the authors were able to achieve a 20.79% efficient PSC. For large-scale production of flexible and cheaper Halide (H) perovskites, one of the main challenges for PSCs is the low-temperature processed oxide layer. In [338], a reverse micelle-water technique for producing highly dispersed ligand-capped ultra-fine SnO₂ QDs was presented. It was found that the ligands responsible for the uniform growth of SnO₂ QD thin films readily exchange for halide via a perovskite solution, allowing for the creation of a junction between the two materials and leading to a PCE of 18.71%.

Liu et al. [335], using an alcohol-based solvent and deionized water, presented a simple approach for synthesizing a colloidal solution of SnO₂ QDs at room temperature. Spin coating the QD colloidal solution followed by post-deposition annealing yielded a superior homogenous ETL. The resulting ETL in a PSC led to an efficiency of 20.1%. This excellent performance is due to the enhanced electronic and optical properties of the SnO₂ QDs based-ETL. The experimental results showed that the cell performance improves by decreasing the rate of charge recombination and increasing the rate of electron extraction.

4.3.4. QDs as HTMs

The two most commonly used HTMs are Spiro-OMeTAD and PEDOT:PSS. However, additives are required when Spiro-OMeTAD is employed. Additives raise production costs, while also making Spiro-OMeTAD hydrophilic. PEDOT:PSS is essentially hydrophilic and is particularly prone to absorbing moisture from air, reducing the stability of the PSCs and degrading the indium-doped tin oxide (ITO). As a result, the search for novel HTMs is critical. By manipulating the particle size of PbS QDs employed as a HTM, Hu et al. [341] were able to produce a wide range of PCEs. A maximum PCE of 7.5% was achieved, with an absorption peak at 890 nm and an energy band at 1.4 eV. Li et al. [342] achieved a PCE of 7.88% by producing OA-coated PbS QD through thermal injection, which retards the rate of charge recombination. The details of various QDs as HTMs are summarized in Table 11.

Table 11. Details of QDs as HTMs. Reproduced with permission from MDPI.

QDs	Device Structure	V _{OC} (V)	J _{sc} (mA cm ⁻²)	FF (%)	η (%)	Refs.
PbS QDs	ITO/PbS QDs/MAPbI ₃ /PCBM/AI	0.86	12.10	72	7.5	[341]
PbS QDs	FTO/c-TiO ₂ /m-TiO ₂ /CH ₃ NH ₃ PbI ₃ /PbS QDs/Au	0.87	18.69	49	7.88	[342]
CQDs	FTO/c-TiO ₂ /m-TiO ₂ /MAPbI ₃ /CQDs/Au	0.52	7.83	74	3	[343]
PbS QDs	FTO/c-TiO ₂ /m-TiO ₂ /CH ₃ NH ₃ PbI ₃ /PbS QDs/Au	0.97	19.03	61.34	11.32	[344]
PbS QDs	FTO/TiO ₂ /m-TiO ₂ /CH ₃ NH ₃ PbI ₃ /PbS QDs/Au	0.80	29.3	83	19.52	[345]
CuInS ₂ QDs	FTO/c-TiO ₂ /m-TiO ₂ /MAPbI ₃ /CuInS ₂ /ZnS QDs/Au	0.92	18.6	48.7	8.38	[346]
CuIn _{1.5} Se ₃ QDs	ITO/SnO ₂ /MAPbBr ₃ /CuIn _{1.5} Se ₃ QDs/Au	0.98	20.46	68.5	13.72	[347]
CuInSe ₂ QDs	ITO/SnO ₂ /FAMAPbI ₃ BrCl/CuInSe ₂ QDs/Au	0.86	22.5	66	12.8	[348]
SnS QDs	FTO/c-TiO ₂ /(CsPbI ₃) _{0.05} (FAPbI ₃) _{0.79} (MAPbI ₃) _{0.16} /SnS QDs/Au	0.94	22.96	63.3	13.72	[349]
MoS ₂ QDs	FTO/c-TiO ₂ /m-TiO ₂ /CsPbBr ₃ /MoS ₂ QDs/Carbon	1.31	6.55	79.4	6.80	[350]
Cu ₂ O QDs	FTO/c-TiO ₂ /m-TiO ₂ /Cs _{0.05} FA _{0.81} MA _{0.14} PbI _{2.55} Br _{0.45} /Cu ₂ O QDs/Au	1.15	22.2	74.2	18.90	[351]
CsSnBr ₃ QDs	FTO/SnO ₂ QDs/CsPbBr ₃ /CsSnBr ₃ QDs/Carbon	1.61	7.8	84.4	10.60	[352]
Ag-In-Ga-S QDs	FTO/c-TiO ₂ /m-TiO ₂ /CsPbBr ₃ /AIGS QDs/Carbon	1.46	7.43	80.31	8.46	[353]
Cu ₁₂ Sb ₄ S ₁₃ QDs	FTO/c-TiO ₂ /CH ₃ NH ₃ PbI ₃ /Cu ₁₂ Sb ₄ S ₁₃ QDs/Au	1.05	21.85	61.6	14.13	[354]
Cu ₁₂ Sb ₄ S ₁₃ QDS	FTO/c-TiO ₂ /m-TiO ₂ /CsPbI ₃ QDs/Cu ₁₂ Sb ₄ S ₁₃ QDs/Au	1.04	18.28	52.9	10.02	[355]
Cu ₁₂ Sb ₄ S ₁₃ QDs	FTO/c-TiO ₂ /CH ₃ NH ₃ PbI ₃ /Cu ₁₂ Sb ₄ S ₁₃ QDs/Au	0.80	18.08	45	6.50	[356]
Cu ₂ ZnSnS ₄ QDs	FTO/c-TiO ₂ /CH ₃ NH ₃ PbI ₃ /Cu ₂ ZnSnS ₄ QDs/Au	1.06	20.54	58.7	12.75	[357]
Cu ₂ ZnSnS ₄ QDs	FTO/m-TiO ₂ /c-TiO ₂ /CsPbBr ₃ /Cu ₂ ZnSnS ₄ QDs/Ag	0.94	7.36	70.01	4.84	[358]
Cu ₂ ZnSnS ₄ QDs	ITO/Cu ₂ ZnSnS ₄ -LF QDs/Perovskite/PCBM/Ag	0.92	20.7	81	15.40	[359]
Cu ₂ ZnSnSe ₄ QDs	FTO/TiO ₂ /CH ₃ NH ₃ PbI ₃ /Cu ₂ ZnSnSe ₄ QDs/Au	0.81	19.37	62.1	9.72	[360]
CuIn _{0.1} Ga _{0.9} (S _{0.9} Se _{0.1}) ₂ QDs	FTO/c-TiO ₂ /m-TiO ₂ /CH ₃ NH ₃ PbI ₃ /CIGSSe QDs/Au	0.94	17.66	54.88	9.15	[361]
CsSnBr ₂ I QDs	FTO/c-TiO ₂ /m-TiO ₂ /CsPbBr ₃ /CsSnBr ₂ I QDs/Carbon	1.39	8.70	76	9.13	[362]

In [345], a finite element method-based 3D model was developed to simulate the optoelectronic properties of an HTM-free CH₃NH₃PbI₃/PbS-CQD solar cell. Compared to a planar PSC with a bare perovskite absorbing layer, the performance of the perovskite/PbS-CQD solar cell was found to be superior in the simulation. To boost the structure's efficiency, the authors optimized the thickness of the PbS-CQD layers, leading to a predicted optimal thickness of 200 nm. In addition, the active layer's light-trapping and carrier-generation abilities were enhanced by employing a pyramidal texture. The idea of texturization is to modify surfaces so that light entering the ALs is reflected several times, thereby raising the probability of electron-hole pair formation. Increasing the texture height led to a PCE of 19.52%. In [351], Liu et al. proposed a facile surface modification technique employing a silane coupling agent for stable and inexpensive cuprous oxide (Cu₂O) QDs. Without breaking the perovskite n-i-p structure, the Cu₂O can be deposited directly on the film as the top HTL. PSCs using modified Cu₂O as the HTL showed a much higher efficiency (18.9%) than those using unmodified Cu₂O (11.9%).

In [359], low-temperature solution-processed SCs with a photoactive layer composed of Cu₂ZnSnS₄ (CZTS) nanocrystals were reported. These high-purity nanocrystals are produced by modifying the surface ligands. CZTS nanocrystals exhibit a significant increase in mobility and photoconductivity after ligand removal, as well as a noticeable photoresponse in a standard heterojunction solar cell structure. A PCE of 15.40% was achieved, alongside a fill factor (FF) of 81% when CZTS nanocrystals were used. Liu et al. [354] used Cu₁₂Sb₄S₁₃ QDs as an inorganic HTM in a PSC. A PCE of 14.13% was obtained for 5.7 nm sized QDs by carefully designing the bandgap alignment of the QDs to speed up the hole transport from

the perovskite layer to the QDs. QDs as HTMs exhibit better stability but, nevertheless, have low PCEs as compared to conventional HTMs. Further research and development are therefore necessary.

In 2011, Im et al. [363] fabricated a 6.5% efficient QDSSC using perovskite (CH_3NH_3) PbI_3 nanocrystals. (CH_3NH_3) PbI_3 CDs on the surface of TiO_2 nanocrystal are obtained as a result of spin-coating a perovskite precursor solution that contains equal volumes of $\text{CH}_3\text{NH}_3\text{I}$ and PbI_2 . Bang et al. [364] designed a QDSSC using two different nanocrystals, namely CdSe and CdTe, linked with TiO_2 via 3-mercaptopropionic acid to establish inter charge transfer. From the experiments, the authors found that these QDs are able to sensitize TiO_2 films and generate photocurrents in QDSCs. To achieve efficient QDSSCs, González-Pedro et al. [365] produced CdSe QDs directly on a TiO_2 surface through repeated ionic layer adsorption and reaction. Both the ZnS coating and the CdS growth history were examined. FF and photocurrents were improved by employing a polysulfide electrolyte with Cu_2S counter electrodes. Under full 1-sun illumination, an incident photon to current efficiency of up to 82% was attained, thereby overcoming the photocurrent limitation frequently seen in QDSCs. Moreover, a PCE of 3.84%, a V_{oc} of 0.538 V, a J_{sc} of 13.9 mA/cm^2 , and a FF of 0.51% under full 1 sun illumination were attained.

4.4. Challenges in QDSSCs

Due to limited conversion efficiency, advances in QDSSC technology have decreased in frequency, hampering its commercial adoption. Aside from efficiency, another difficulty impeding the commercialization of QDSSCs is their low-performance stability. QDSSC performance stability may be defined as the physical, chemical, mechanical, thermal, photochemical, electrochemical, and environmental stabilities that impact the device's performance over time. However, these stabilities are closely related to the stabilities of other device components, such as the type of QD employed, the photoanode, the reactivity of the electrolyte, and the behavior of the CE during electrocatalysis. It is difficult to quantify the processes that impact the performance stability of QDSSCs due to the many degradation mechanisms connected with the different device components. QDSSC technologies must thus be able to sustain their performance for a number of years under standard working environments in order to be practical and economically feasible.

5. Tandem Solar Cells

A Tandem solar cell (TSC) is a type of solar cell having different materials of different bandgaps stacked together in a single structure to utilize sunlight as much as possible for the production of electrical power [366], as illustrated in Figure 8. TSC can utilize around 86% of the solar spectrum [367], which is made possible by connecting cells of different bandgaps. In order to utilize the solar spectrum as much as possible, different materials having different properties can be connected to form a new structure having the combined properties of the stacked materials, with an improved PCE compared to the individual materials. For manufacturing, the most important consideration is to maintain a temperature below 150 °C [368,369]. The perovskite solar cell with a better exciton generation rate with 1.15 V open circuit voltage is the best candidate for tandem cells [370], with the reconfigurable band gap of 1.48–2.23 eV depending upon the halide synthesis. Due to the high band gap energy of perovskite, it is reasonable to harvest the high energy photons of wide-band and with lower silicon levels or CIGS solar material used to harvest the infrared and near-infrared spectrum. In recent work with perovskite and silicon tandem cells, more than 30% PCE has been achieved [368,371].

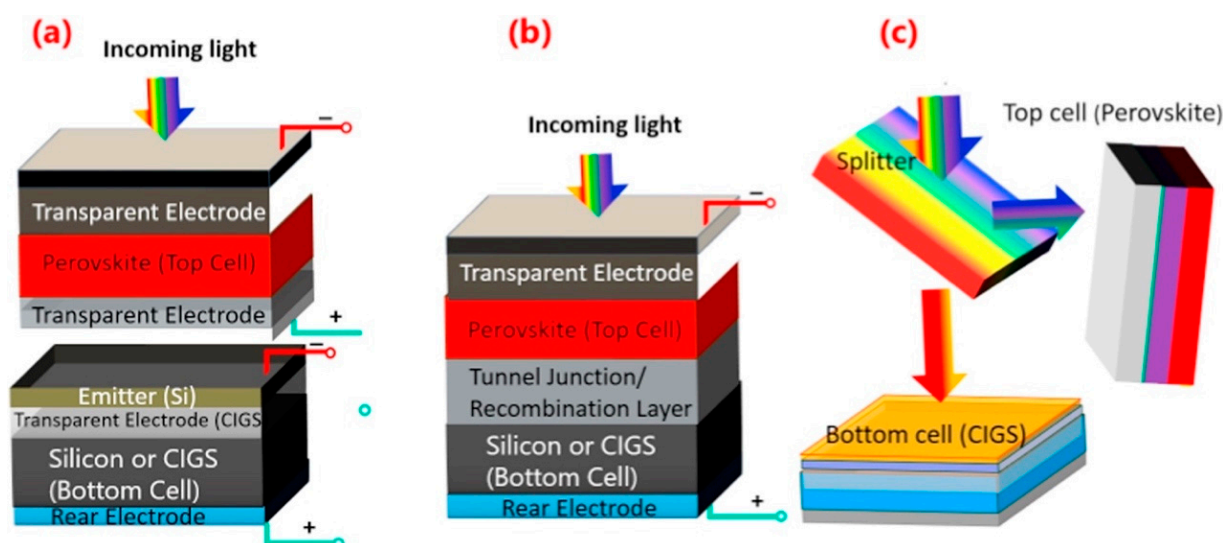


Figure 8. Shows schematic diagram of TSC, (a) mechanically stacked 4T, (b) monolithically integrated 2T, and (c) optical splitting of the solar spectrum [368]. Reproduced with permission from Qamar Wali et al., *Renewable and Sustainable Energy Reviews*, Elsevier, 2018.

PSC/Si-based tandem solar cells have different energy levels and different functional layers, namely the front contact, ETL, perovskite absorber, HTL, and back contact. The front contact, which has a significant impact on the optical and electrical properties of the device, is usually a metal oxide. The perovskite absorber is used for light harvesting, i.e., absorbing photons to generate electrons, whereas the ETL and HTL extract and transmit/transport the electrons and holes generated at the perovskite absorber. To obtain optimized perovskite solar cells, the optimization of the functional layer has to be achieved [369,372].

Polymers are widely used in different third-generation SCs such as DSSC, PSC, and TSC to obtain efficient SCs. Gaiinda et al. [373] in 2022 provide a detailed study of the different polymeric materials being used as different components in third-generation SCs. You et al. [374] reported an efficient low-bandgap polymer, i.e., poly[2,7-(5,5-bis-(3,7-dimethyloctyl)-5H-dithieno[3,2-b:20,30-d]pyran)-alt-4,7-(5,6-difluoro-2,1,3-benzothiazadiazole)], having high mobility and a bandgap of 1.38 eV. By using the reported polymer, the authors obtained a 10.6% efficient solution-processed TSC. OPV cells have numerous advantages, but their performance is inferior to that of other solar cells (SCs) due to the limited charge mobility of organic materials, which limits the active layer thickness and light absorption. To take advantage of OPV cell properties, such as having tunable bandgap, and high diversity, Meng et al. [375] utilized semiempirical model analysis and a tandem cell strategy to obtain a 17.29% efficient two-terminal monolithic solution-processed tandem OPV.

According to the latest updates, PSC/Si-based tandem solar cells have achieved an efficiency of 32.5% [NREL¹]. The performance of the device is greatly influenced by the interface between the ETL and perovskite absorber. Poor band alignment of the ETL with the perovskite absorber can deteriorate the device performance by increasing series, shunt, and recombination resistance. To address these issues, it is important to use materials with high electron mobilities and appropriate band alignment. In the literature, efforts have been made by various research groups using different materials that align with perovskite, and these studies are summarized in Table 12.

Table 12. ETMs used for different configurations of tandem cells.

Top Cell (TC)	Bottom Cell (BC)	ETL	V _{OC} (V)	J _{sc} (mA cm ⁻²)	FF (%)	Area (cm ²)	η (%)	T.C η (%)	B.C η (%)	Refs.
CH ₃ NH ₃ PbI ₃	C-Si	C ₆₀	–	–	–	–	24.6	16.23	8.37	[376]
CsFAMA	n-Si	SnO ₂	–	39.50	–	–	28.2	19.00	24.00	[377]
(MAPb(I _{0.95} Br _{0.05}) ₃)	C-Si	PCBM/ZnO	1.67	18.29	77.00	–	23.50	–	–	[378]
FA _{0.83} Cs _{0.17} Pb(I _{0.80} Br _{0.20}) ₃	C-Si	SnO ₂ -LiCl	1.90	16.90	77.90	0.50	25.40	–	–	[379]
Cs _{0.05} MA _{0.15} FA _{0.8} Pb(I _{0.85} Br _{0.15}) ₃	C-Si	C ₆₀ Anchored /a-NbO _x	1.80	19.50	75.90	–	27	–	–	[380]
CsFAMABrI	C-Si	TiO ₂	1.80	18.81	75.60	1.20	26.30	–	–	[381]
CsMAPbBr	C-Si	C ₆₀	1.82	19.20	74.40	–	26	–	–	[382]
CH ₃ NH ₃ PbI ₃	p-Si	ZnO	1.77	20.19	82.22	–	28.50	–	–	[383]

The most effective method for increasing the ability of a cell to convert solar energy into electrical energy is thought to be the use of multi-junction solar cells. In [383], researchers simulated a monolithic TSC made of perovskite/Si layers having high and low bandgap values. These layers were separated by a recombination layer, a spiro-meOTAD/Si layer, a window layer made of ZnO, a buffer layer of CdS, and a highly doped back surface layer of n++Si to prevent recombination at the back surface. The aforementioned structure was optimized, and its performance was examined for different parameters, including the active layer thickness, bandgap, and dopant concentration. The optimal Voc, Jsc, FF, and efficiency were found to be 1.77 V, 20.19, 82.22%, and 28.50%, respectively.

In [377], the authors use a technique called “boosted solvent extraction” to enhance the thickness of perovskite films while maintaining their smooth shape, obtaining a PCE of 28.2% by stacking the perovskite cell above a Si bottom. Lamanna et al. [381] introduced a mechanically stacked two-terminal perovskite/Si TSC, wherein the sub-cells were optimized separately and connected by connecting the back electrode of the perovskite (top) cell to the front contact of the Si (bottom) cell. The optical losses were lowered by engineering electron and hole selective layers, achieving 26.3% efficiency.

Apart from using an ETL for improving the device performance, HTLs such Spiro-OMeTAD and PTAA can also be used. Various investigations have been conducted using HTLs in different configurations, with prominent examples summarized in Table 13. The materials listed in Tables 12 and 13 are the most commonly used for the ETL and HTL, along with perovskite. All materials listed as ETLs and HTLs have suitable band gaps that align well with the perovskite absorber layer.

Table 13. HTMs utilized for various configurations of tandem cells.

TC	BC	HTL	Configuration	V _{OC} (V)	J _{sc} (mA cm ⁻²)	FF (%)	Area (cm ²)	η (%)	T.C η (%)	B.C η (%)	Refs.
CH ₃ NH ₃ PbI ₃	C-Si	Spiro-OMeTAD	p-i-n	–	–	–	–	23.70	–	–	[384]
(FAPbI ₃) _{0.95} (MAPbBr ₃) _{0.05}	P-Si	PTAA	p-i-n	0.65	13.50	80.10	–	26.0	18.90	7.10	[385]
(Cs _{0.05} (FA _{0.83} MA _{0.17}) _{0.95} Pb(I _{0.83} Br _{0.17}) ₃)	C-Si	Spiro-OMeTAD	n-i-p	–	–	–	–	17.10	11.70	5.40	[386]
Cs _m FAnMA _{1-m-n} PbI _x Br _{3-x}	C-Si	NiO _x /poly-TPD	p-i-n	1.88	19.12	75.30	1	27.00	–	–	[387]

Table 13. Cont.

TC	BC	HTL	Configuration	V _{OC} (V)	J _{sc} (mA cm ⁻²)	FF (%)	Area (cm ²)	η (%)	T.C η (%)	B.C η (%)	Refs.
Cs _{0.05} (FA _{0.83} MA _{0.17}) _{0.95} Pb(I _{0.8} Br _{0.2}) ₃	C-Si	Poly TPD and NPD	p-i-n	1.74	17.93	74.31	–	25.20	–	–	[388]
CH ₃ NH ₃ PbI ₃	C-Si	PEDOT:PSS	n-i-p	1.78	14.70	80.40	–	21	–	–	[389]

By stacking a semitransparent PSC with an efficiency of 18.9% and an unfiltered Si solar cell with an efficiency of 22.9%, Park et al. [385] reported a 26.0% efficient perovskite/Si TSC. A surface treatment method was used to modify the WO_x surface with NbO_y in a typical mp-TiO₂-based n-i-p structure for the semitransparent PSC. The fill factor was greatly enhanced by this buffer method, attaining values that were nearly as high as those of the traditional opaque devices, above 80%. Abbasiyan et al. [384] used a novel quasi-periodic intermediate structure to improve the efficiency of perovskite/Si tandem solar cells. Seven SiO₂ and TiO₂ layers, with a combined thickness of 1150 nm, formed the suggested FC(3,3) intermediate structure. It was shown that this proposed structure improves the conversion efficiency by 5%, reaching 23.70%. Findings obtained using a transfer matrix approach and a finite difference time domain analysis were in good agreement. Moreover, Ag nanoparticles with an optimum radius of 125 nm were used to boost the absorption efficiency of the bottom cell (thin-film Si layer) down to 5 m. Using Ag nanoparticles and the proposed structure, a boost of 88% in the short circuit current density was achieved.

In TSCs with Si, wide-bandgap metal halide perovskites are a promising semiconductor that could help reach the objective PCEs above 30% at a low cost. However, photoinduced low Voc values and phase segregation have been significant roadblocks for wide-bandgap PSCs. In [387], triple-halide alloys (bromine, chlorine, iodine) were used to tune the band gap and stabilize the semiconductor to create 1.67-electron-volt wide-bandgap perovskite top cells. The authors demonstrated that decreasing the lattice parameter by substituting some of the iodine with bromine improves the solubility of chlorine, leading to an increase in photocarrier lifetime and charge-carrier mobility. Semitransparent top cells degraded by less than 4% during 1000 h of maximum power point (MPP) operation at 60 °C. Using Si bottom cells and these top cells in tandem, they were able to achieve a PCE of 27% in two-terminal monolithic tandems of just 1 square centimeter in total.

6. Organic Photovoltaics

Organic photovoltaics (OPVs) are considered a third-generation technology and have received significant attention due to properties such as being able to produce cheap electrical power, their mechanical flexibility, and low weight [390]. PCEs have seen a significant increase in activity as a result of the progress in both novel materials for the donor and acceptor. Recently, bulk heterojunction (BHJ) OPVs have achieved PCEs of more than 18% [391,392], with improvements of 150% over the past decade for mono-layer devices [393]. Although OPVs are a promising technology, they cannot be widely commercialized until PCEs are increased [394,395]. In a standard BHJ OPV device, an electron donor (D) and an electron acceptor (A) are mixed to form a continuous interpenetrating network that serves as the photoactive layer. Light absorbed by the active layer creates an exciton (a bound state of electron–hole pair) that travels towards the D/A interface, where it is dissolved into free charge carriers. The photocurrent is generated when the free electrons and holes move via the D and A phases to the anode and cathode, respectively [396–399].

The infrared (IR) portion of the solar spectrum makes up 52% of what reaches Earth's surface, while the visible light portion accounts for 43% and the ultraviolet (UV) portion makes up the remaining 5% [399,400]. If the donor and acceptor materials have a large enough energy gap (E_g), then more of the sun's spectrum will be available for harvesting by OPVs. In order to be absorbed and produce excitons, a photon must have an energy

greater than that of either the donor or the acceptor. With a smaller band gap, more of the sun's energy can be captured. Existing light-capturing materials in OPVs are limited to absorbing just a small portion of the solar spectrum (mostly the visible range) [400,401]. Additionally, as the thickness of the active layer is increased, more photons are absorbed by the device at a given wavelength. However, the VOC and, hence, the power consumption efficiency (PCE) of the device can be reduced by a small bandgap. In addition, the photo-generated excitons have a short diffusion length (LD) and a short lifetime, which leads to an increase in charge carrier recombination in a thick active layer [402–404]. Therefore, optimal performance requires striking a balance among optical absorption, VOC transfer, and carrier transport [405].

Over the past few decades, numerous methods have been proposed to boost the efficiency of OPVs. Either better materials or methods that enhance the device's structure and engineering can be developed and implemented to boost performance. To increase the PCE of OPVs, advances in low bandgap conjugated donor polymers [406–408] and tunable non-fullerene (NF) acceptors (A) [399] have been made. In 2015, Zhan's team disclosed a new class of NF acceptors they called ITIC, which were built on a seven-ring fused core and capped with 1,1-dicyanomethylene-3-indanone (IC) groups [409]. Following that, several potentially useful ITIC derivatives, such as IT-4F, were produced, and the associated PCEs were raised to 13% [410]. In 2019, Yuan et al. developed a star NFA, Y6, using dithienothiophen[3.2-b]-pyrrolobenzothiadiazole (BTP) as its core and achieved a high PCE of 15.7% [411]. Since then, various high-efficiency Y-series acceptors have been reported [412] based on heteroatomic substitution on the fused-ring core, side-chain tailoring, and end-capped groups modification, and the most recent organic solar cells have achieved over 19% PCE [413,414]. Figure 9 illustrates the structures of OPVs.

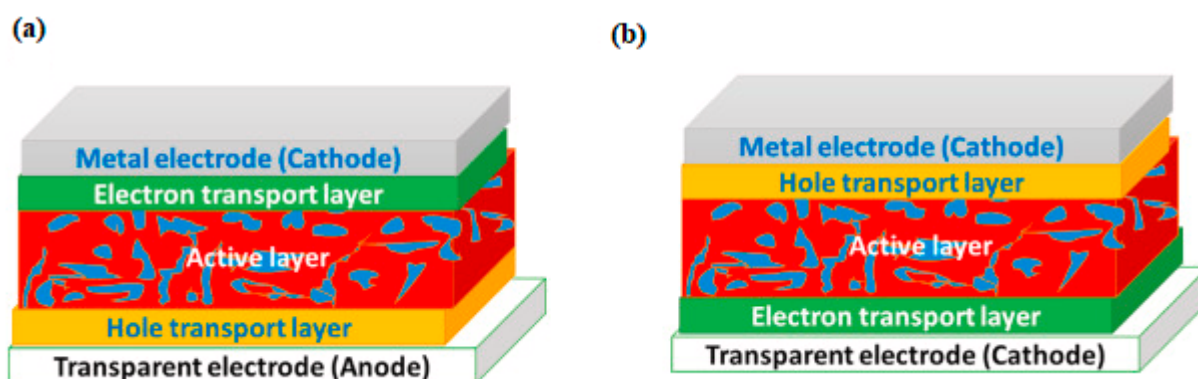


Figure 9. (a) Regular (b) Inverted geometry BHJ structures of OPVs [415]. Reproduced with permission from Kamel et al., Renewable and Sustainable Energy Reviews, Elsevier, 2022.

6.1. Working Mechanisms of an OPV

The PV effect, where a voltage is generated at the interface between two materials due to the absorption of light [416], can be broken down into five distinct steps in OPVs. One of the bonding electrons in the high occupied molecular orbital (HOMO) absorbs a photon with energy greater than or equal to the donor's or acceptor's E_g and is driven to the lowest unoccupied molecular orbital (LUMO), leaving behind an unoccupied state (hole). The strong electrostatic attraction between photo-generated electron–hole pairs and the low dielectric constant of organic semiconductors leads to the formation of bound states known as excitons. Since there is an energy difference between the exciton's LUMO and the electron's LUMO, the exciton can diffuse through LD until it reaches the (D/A) interface, where it dissociates into free charge carriers. Energy transmission between excitons at the D/A interface improves PCEs [417] for other structures such as layer-by-layer (LBL) OPVs by moving electrons from the donor to the acceptor. The photocurrent at the external circuit is generated when the free electrons travel through the acceptor material and the holes travel through the donor [398,399,405].

6.2. D-A Materials

The material composition of the photoactive layer, including D/A materials, has traditionally been a critical aspect in achieving high PCE in OPVs. The D/A materials used in BHJ OPVs should generally have the following characteristics: (i) matching absorption spectrum; (ii) proper alignment of molecular energy levels; (iii) nanoscale phase separation; and (iv) excellent charge carrier mobility [418].

6.2.1. Acceptor Materials

There have been two stages of investigation towards developing acceptor materials. Fullerene derivatives such as PC61BM and PC71BM were the most common OPV acceptors prior to 2015. Better visible-range absorbance, greater electron mobility, and enhanced D/A miscibility were all reported for the NFA ITIC by Lin and colleagues in 2015 [409]. Since then, NFAs have received a great deal of interest, and NFA-based OPVs have achieved remarkable advancements in terms of performance. Here, we cover the NF-based acceptors.

The two most effective NFAs are the imide-based NFAs and the A-D-A type NFAs. Here, we shall discuss the A-D-A type NFAs in detail, being those in which the conjugated “push-pull” structure was actually implemented. The “A” and “D” denote the electron-drawing and electron-donating moieties, respectively, in the A-D-A structure. Conjugation can be lengthened and the bandgap can be lowered by combining electron-rich and electron-deficient moieties [399]. Table 14 lists the performance indicators of OPVs that make use of these effective small molecule NFAs.

Table 14. Features of small molecule NFAs and respective devices performances.

Acceptor	HOMO/LUMO (eV)	Donor	J _{sc} (mA/cm ²)	V _{oc} (V)	FF (%)	PCE (%)	Refs.
ITIC	−5.48/−3.83	PTB7-Th	14.21	0.81	59.1	6.80	[409]
ITIC	−5.51/−3.78	PBDB-T	16.81	0.899	74.2	11.21	[419]
ITIC	−5.48/−3.83	PBDTS-TDZ	17.78	1.10	65.4	12.80	[420]
ITIC-Th	−5.66/−3.93	PDBT-T1	16.24	0.88	67.1	9.6	[421]
IT-M	−5.58/−3.98	PBDB-T	17.44	0.94	73.5	12.05	[422]
IT-4F	−5.66/−4.14	PBDB-T-SF	20.50	0.88	71.9	12.97	[410]
SeTIC4Cl	−5.65/−4.08	PM6	22.92	0.78	75	13.32	[423]
IDIC	−5.7/−3.9	FTAZ	20.8	0.84	71.8	12.5	[424]
IOIC3	−5.38/−3.84	PTB7-Th	22.9	0.762	74.9	13.1	[425]
FOIC	−5.36/−3.92	PTB7-Th	24.0	0.743	67.1	12.0	[426]
Y6	−5.65/−4.10	PM6	25.2	0.82	76.1	15.7	[411]
Y6	−5.7/−4.1	PM6	27.43	0.845	73.8	17.1	[427]
Y6	−5.65/−4.10	D18	27.70	0.859	76.6	18.22	[403]
BTP-4Cl	−5.65/−4.02	PM6	25.4	0.867	75	16.5	[428]
BTP-eC9	−5.64/−4.05	PM6	26.2	0.839	81.1	17.8	[429]
Y6Se	−5.70/−4.15	D18	27.98	0.839	75.3	17.7	[430]
<i>m</i> -BTP-PhC6	−5.51/−3.46	PTQ10	25.3	0.883	79.3	17.7	[431]
L8-BO	−5.68/−3.90	PM6	25.72	0.87	81.5	18.32	[432]
L8-BO	-/-	PM6	26.03	0.893	80.0	18.60	[433]

The PCE of advanced OSCs can be over 18%. However, the significant voltage loss (V_{loss}) of OSCs is a major barrier to their further enhancements. To lower the V_{loss} of PM6:L8-BO devices, diiodomethane (DIM) was used as a solvent additive by Song et al. [433]. Utilizing DIM in place of the typical 1,8-diiodooctane solvent additive in the PM6:L8-BO blend

results in a smaller energy gap between the singlet excited state and the charge transfer state, which in turn results in a lower V_{loss} . As a result, a DIM-processed device achieved an efficiency of 18.20% at a V_{oc} of 0.893 V. To decrease the Urbach energy, which lowers the recombination loss of a high-performance electron acceptor, Y6Se, Zhang et al. [430] proposed a simple method of selenium replacement. Compared to its sulfur-containing counterpart (Y6), Y6Se exhibited a lower Urbach energy (20.4 meV), wider and greater absorption, better electron mobility, and improved photostability. Y6Se-based OSCs exhibited an efficiency of 17.7%.

For the chlorinated non-fullerene acceptor BTP-4Cl-based OPV, Cui et al. [428] reported a PCE of 16.5%. The chlorination process increases optical absorption and contributes to a high JSC of 25.4 mA cm^{-2} . A higher VOC of 0.867 V is reached at a bandgap of 1.400 eV, with a corresponding energy loss of only 0.533 eV, which is unlikely given that BTP-4Cl exhibits a downshifted LUMO level compared to its fluorinated homolog BTP-4F. The rise in VOC can be partially attributed to the fact that the non-radiative energy loss is just 0.206 eV. Using the fused-ring acceptor unit DTBT, Liu et al. [403] produced an improved copolymer donor D18. DTBT provides greater hole mobility to D18 because of its broader molecular plane than DTTP. It was shown that D18:Y6 solar cells have a PCE of 18.22%.

6.2.2. Donor Materials

Donor materials are just as important to the development of OPVs as highly efficient acceptors. Because of their conducting and photoluminescent characteristics, conjugated PPV and its derivatives garnered significant attention from the outset of BHJ-OPVs. In 1995, Yu et al. combined MEH-PPV and PC61BM as the active layer of OPVs, dramatically improving charge separation and collection efficiency [434]. Later, Shaheen and colleagues [435] recorded a PCE of 2.5% using MDMO-PPV as the donor and PC61BM as the acceptor. Due to its high carrier mobility, good solubility, features of crystallinity, and self-assembly, poly(thiophene)-based conjugated polymer, P3HT, has since been widely used as the donor material in OPVs.

For OPVs, LBG polymers are typically required to increase the active layer's light-harvesting range, as fullerene derivatives have a relatively low absorption ability. However, it is possible that NFA-based OPVs cannot make use of most of the donor materials used in fullerene-based OPVs. Light-harvesting ability is one area where NFAs typically outperform fullerene analogues. As a result, high-performance OPVs based on NFAs could be obtained using a wider range of donor materials, from WBG to LBG, than is possible with fullerene acceptors. Table 15 lists the performance indicators of a number of OPVs that make use of these effective small molecule NFAs.

Table 15. Features of small molecule NFAs and respective devices performances.

Donor	HOMO/LUMO (eV)	Acceptor	J_{sc} (mA/cm ²)	V_{oc} (V)	FF (%)	PCE (%)	Refs.
PDBT-T1	−5.36/−3.43	ITIC-Th	16.24	0.88	67.1	9.6	[421]
PBDB-T	−5.33/−2.92	ITIC	16.81	0.899	74.2	11.21	[419]
PBDB-T	−5.39/−3.50	Y1	22.44	0.87	69.1	13.42	[436]
PBDB-T-SF	−5.40/−3.60	IT-4F	20.88	0.88	71.3	13.10	[410]
PBDB-T-2F (PM6)	−5.47/-	IT-4F	20.81	0.84	76	13.2	[437]
PM6	−5.56/−3.50	Y6	25.2	0.82	76.1	15.7	[411]
PM6	−5.47/−3.56	BTP-eC9	26.2	0.839	81.1	17.8	[429]
PBDB-T-2Cl (PM7)	−5.51/-	IT-4F	21.80	0.86	77	14.4	[436]

Table 15. Cont.

Donor	HOMO/LUMO (eV)	Acceptor	J _{sc} (mA/cm ²)	V _{oc} (V)	FF (%)	PCE (%)	Refs.
PM7	−5.52/−3.57	Y6	25.644	0.897	74.0	17.037	[437]
T1	−5.48/−3.63	IT-4F	21.5	0.899	78	15.1	[438]
J61	−5.32/−3.08	ITIC	17.43	0.89	61.48	9.53	[439]
J91	−5.50/−3.02	m-ITIC	18.03	0.984	65.54	11.63	[440]
D16	−5.48/−2.83	Y6	26.61	0.85	73.8	16.72	[441]
D18	−5.51/−2.77	Y6	27.70	0.859	76.6	18.22	[403]
D18	-/-	N3	27.44	0.862	78.5	18.56	[442]

For polymer donors, D18 had the best hole mobility and overall performance. To investigate the capabilities of D18, Jin et al. [442] evaluated a number of non-fullerene acceptors and observed that N3 is a promising partner for D18. With a ITO/PEDOT:PSS/D18:N3/PDIN/Ag solar cell architecture, the authors achieved a PCE of 18.56%, a Voc of 0.862 V, a Jsc of 27.44 mA cm^{−2}, and FF of 78.5% in an organic solar cell. Ma et al. [437] replaced PM6 with PM7 and were able to produce a higher Voc and a better match with Y6 owing to the decreased HOMO enabled by a hot-cast fabrication technique. The PM7:Y6 system achieved an efficiency of 17.0%, a Jsc of 25.644 mA cm^{−2}, a Voc of 0.897 V, and FF of 74.0%.

To maximize the benefits of FRAL copolymers, Xiong et al. [441] synthesized the thiolactone unit 5H-dithieno[3,2-b:2',3'-d]thiopyran-5-one (DTTP) to create the copolymer D16. The substitution of thiolactone for lactone in the transition from L1 to D16 improved π - π stacking and provided increased hole mobility on D16. High PCEs of up to 16.72% were obtained from traditional solar cells using D16 as the donor and Y6 as the acceptor. In [429], impressive photovoltaic characteristics in OPV cells are obtained by optimizing alkyl chains on a chlorinated nonfullerene acceptor (NFA), BTP-4Cl-BO (a Y6 derivative). To improve the order of the intermolecular packing, the n-undecyl at the edge of BTP-eC11 was reduced to n-nonyl and n-heptyl. Hence, BTP-eC9 and BTP-eC7 NFAs were produced. BTP-eC9 has better electron transport properties and a higher solubility than BTP-eC11. As a result of the increased Jsc and FF, the BTPeC9-based single-junction OPV cells achieved a maximum PCE of 17.8%.

6.3. Challenges towards Commercialization

OPV-based devices have many advantages over the traditional Si based devices, such as low weight, huge potential for large scale applications, and flexibility. However, the photoactive layer of these devices is processed from halogenated solvents, such as dichlorobenzene and chlorobenzene. Environmental damage and contamination will result from the emission of these halogenated solvents into the atmosphere. Additionally, their volatilization during the manufacture of the device is harmful and potentially cancer-causing. Moreover, the cost of these halogenated solvents is also high. They are therefore unfit for the industrial manufacture of OPVs on a wide scale and for commercialization. As a result, it is necessary to stop using harmful halogenated solvents in the production of OPVs and replace them with eco-friendly solvents. Additionally, the operational stability of OPV devices needs to be improved to extend the lifetimes of these devices.

7. Other Third-Generation Technologies

7.1. Up-Conversion Devices

In simple terms, photon up-conversion (UC) occurs when two or more photons are sequentially absorbed, followed by the emission of light at a shorter wavelength than the excitation wavelength. In scientific terms, this is an anti-Stokes emission. Light from the infrared spectrum can be made visible. Several methods allow UC to occur in both

organic and inorganic materials. Polycyclic aromatic hydrocarbons are typically the kind of organic molecules that are capable of accomplishing photon UC through the process of triplet–triplet annihilation (PAHs). Ions of d-block or f-block elements, such as Ln^{3+} , Ti^{2+} , Ni^{2+} , Mo^{3+} , Re^{4+} , and Os^{4+} , are commonly found in inorganic materials that may perform photon UC.

Mechanisms behind Photon UC

Inorganic materials have three fundamental methods for photon UC, while organic materials have at least two unique mechanisms. Three mechanisms, energy transfer UC, excited-state absorption (ESA), and photon avalanche, are responsible for photon UC in inorganic materials (PA). These phenomena can be observed in a wide range of materials, from optical fibers to bulk crystals to nanoparticles, as long as they contain at least one of the aforementioned active ions. Energy pooling and sensitive triplet–triplet annihilation (sTTA) allow organic molecules to up-convert photons [443,444].

It is important to distinguish between UC and second-harmonic production and two-photon absorption. Similar to photon UC, these two physical processes also result in the emission of photons with shorter wavelengths than those used for excitation, but their underlying mechanisms are distinct [445]. Bloembergen first proposed the idea in 1959 [446], and Auzel made the first observation of the process in 1966 [447].

Another option is a thermal UC system. This technique relies on the up-converter's ability to absorb low-energy photons, heat them up, and then re-emit higher-energy photons [448,449]. By carefully designing the up-converter's density of optical states, frequency- and angular-selective emission characteristics can be achieved, leading to a more efficient process. A planar thermal up-converting platform can have a front surface that efficiently collects low-energy photons incident within a specific angular range and a back surface that efficiently emits only high-energy photons. Photonic crystal designs allow for the realization of these surface features, and their use in thermophotovoltaics and passive radiative cooling has been proved both theoretically and experimentally [450,451]. When employing the AM1.5D spectrum and the sun as a black body source at 6000 K for a single-junction cell, the PCE from solar radiation to electricity can increase to 73% and 76%, respectively [452].

7.2. Down-Conversion and Down-Shifting Devices

Traditional solar cells are designed to absorb light in the visible spectrum, which is where a significant chunk of the sun's energy is found. The efficiency of solar cells may be improved if we could also utilize the ultraviolet (UV) or/and infrared (IR) regions of the spectrum. After capturing UV rays, some substances can release several visible or near infrared photons. The term "down-conversion" (DC) describes this procedure [453,454]. In 1957 [455], Dexter was the first to consider employing DC to separate a UV photon into two visible photons. By using host lattice states or ions (either alone or in combination) DC can be achieved, which can result in quantum efficiencies greater than unity [453,456–458]. Down-shifting refers to a similar process that takes place in a material with a quantum efficiency less than unity [459].

Even though DC and DS are both related processes, their quantum efficiencies are distinct. Quantum efficiency is less than unity in the DS process, and thermalization losses are not mitigated [460]. However, surface recombination losses can be reduced, leading to higher solar cell efficiency. When compared to DS layers, which can emit no more than one low-energy photon for every high-energy photon absorbed, DC converters emit two low-energy photons for every high-energy photon. In Figure 10, we see a simplified diagram of the DS and DC procedure. When one photon is absorbed, two photons with less energy are produced in DC, provided that the wavelength is similar to that of the solar cell's bandgap. In DS, a similar process takes place, but only one photon is retrieved for every absorbed one.

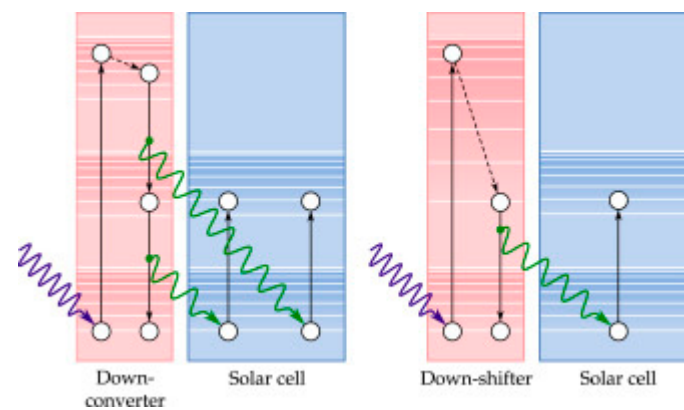


Figure 10. Energy diagram that shows schematically different behaviors among a DC and a DS material used to harvest the efficiency in a solar cell [461]. Reproduced with permission from Mora et al., *Solar Energy Materials and Solar Cells*, Elsevier, 2017.

7.3. Hot Carrier Solar Cells

In order to make photovoltaics an even more appealing technology as a future renewable energy source, numerous approaches have been suggested to circumvent the Shockley–Queisser limit [462]. Most of these efforts are made to boost the device’s current, which is achieved by increasing the number of extracted charges, or “charge carriers,” in some way, such as by converting multiple photons with energies below the band gap into a single photon with an energy above the gap (up-conversion) or by converting a single photon with a high energy into a larger number of charge carriers (multiple exciton generation, singlet exciton fission) [463,464].

By employing multiple junctions, i.e., a cascade of absorber materials with progressively narrower band gaps, it may be possible to decrease losses caused by carrier relaxation, thereby increasing the device voltage. Although the PCE can be greatly improved by using multiple junctions in a single cell, known as “tandem” or “multijunction”, their design is more complicated. The term “hot carrier solar cell” (HCSC) refers to the idea that the extra energy of these photons can be collected by removing charge carriers in single junction solar cells before they relax (HCSC). This concept was first introduced in 1982, and it was claimed that at 1 sun illumination, the maximum PCE could be increased to 66%, and that under maximum solar light concentration, the maximum PCE could increase to nearly 85% [465]. Furthermore, it has been demonstrated that HCSCs are less susceptible to fluctuations in the illumination spectrum compared with tandem devices [466].

Surprisingly, though, experimental efforts to actualize this concept are scant due to two major obstacles. The first step is to identify an appropriate absorber material, one in which the rate of cooling can be slowed down to enable the extraction of carriers with excess energy while still retaining all of the characteristics of a good solar cell material. In order to prevent cooling through the contacts and the leaking of hot carriers, the second task is to design contact materials with a narrow density of states at an adequate energy level [467]. The majority of experimental work in this area addresses either of these obstacles.

7.4. Intermediate Band Photovoltaics

For solar cells to achieve efficiencies higher than the Shockley–Queisser limit, researchers have turned to techniques involving intermediate band photovoltaics. It introduces a new energy level known as the intermediate band (IB) in between valence and conduction bands. According to theory, the presence of an IB makes it possible for two photons with energies below the bandgap to excite one electron from the valence band to the conduction band. As a result, efficiency and induced photocurrent are increased [468].

Using detailed balance, Luque and Marti first produced a theoretical upper bound for an IB device with a single midgap energy level. They used the assumption that the device was fully concentrated and that no carriers had been gathered at the IB [468]. For

a bandgap of 1.95 eV with an IB of 0.71 eV from either the valence or conduction band, they discovered the highest efficiency to be 63.2%. The limiting efficiency at one solar illumination is 47% [469].

Following up on these findings, Green and Brown proceeded to derive the theoretical efficiency threshold for a device having an infinite number of IBs [470]. The number of IBs decides the absorption of solar spectrum, i.e., the higher the number of IBs is, the higher the incident solar spectrum will be absorbed and vice versa. They determined that the maximum efficiency was 77.2% [470], which is less than that of a cell having infinite multijunctions. This is because electrons in an IB device must undergo yet another energy transition before they can be collected in the conduction band, but in a multijunction cell, collection occurs immediately after electrons are excited to a higher energy state [470].

7.5. Multiple Exciton Generation

An exciton is a composite uncharged entity that is formed when an excited electron in the conduction band of a quantum dot solar cell interacts with the hole it leaves behind in the valence band. The carrier multiplication effect in a dot can be understood as creating multiple excitons and is called multiple exciton generation (MEG). Because of the short durations of the multiexcitons, energy extraction from MEG may be challenging, but the potential gains in energy conversion efficiency for nanocrystal-based solar cells warrant further investigation.

Colloidal PbSe quantum dots were used to investigate MEG for the first time in 2004 [471], and subsequent studies have confirmed its presence in various quantum dot compositions, including as PbS, PbTe, CdS, CdSe, InAs, Si [472], and InP [471]. In contrast, the MEG impact was overstated in many preliminary studies of colloidal quantum dots because of undetected photocharging; this problem was eventually identified and fixed by vigorously swirling colloidal samples [466]. Using colloidal PbSe quantum dots, multiple exciton production was first shown in a working solar cell in 2011 [460]. Semiconducting single-walled carbon nanotubes (SWNTs) were shown to generate multiple excitons after absorbing a single photon [473]. Absorption of a single photon with an energy equal to 3 times the SWNT energy gap leads in an exciton generation efficiency of 130% per photon. The threshold for multiple exciton generation in SWNTs can approach the limit set by energy conservation.

Multiple exciton production has also been reported in graphene [474], a material with close ties to nanotubes. In addition, double-exciton production by singlet exciton fission with very high quantum efficiency has been seen in organic pentacene derivatives [475].

7.6. Flexible Thin-Film SCs

Flexible thin-films are another important third-generation technology that aims to produce low-cost efficient SCs. In general, a thin-film solar cell is made by depositing multiple functional layers on a flexible substrate using methods such as vacuum-phase deposition, solution-phase spin-coating, and printing. The entire cell is supported mechanically and protected from the environment by a flexible substrate. The photoelectric charge carriers are collected by two electrodes, which also serve as electrical leads to external circuits. In order for the device to absorb sunlight and convert it into photoelectric charge carriers, it is necessary for one of the electrodes to possess optical transparency. The active materials are crucial components of flexible SCs and are responsible for significantly impacting the PCE. The active materials can be delineated into three distinct groups, namely organic, inorganic, and inorganic–organic hybrid semiconductors. The common inorganic semiconductors include amorphous silicon, cadmium telluride, and copper indium gallium diselenide. Organic semiconductors comprise organic compounds that act as donors and acceptors. These compounds are categorized based on their molecular size, with small organic molecules and polymers being the two primary classifications. Metal halide perovskite is considered to be the most viable material for flexible SCs among inorganic–organic semiconductors [476].

8. Comparison and Future Direction of Third-Generation SC

All the third generation SCs have some advantages and some limitations which are listed in Table 16. As can be seen in in this table, among all the third generation SCs, PSCs have many advantages such as low cost, high efficiency, simple fabrication methods, and low weight but also have stability issues. By improving its stability under high humidity conditions, this technology will enter into a whole new area.

Table 16. Overview and comparison of third generation SCs. The efficiencies are available from The National Renewable Energy Laboratory (NREL) Best research-cell efficiency chart. “<https://www.nrel.gov/pv/cell-efficiency.html> (accessed on 9 January 2023).

Technology	Efficiency	Advantages	Limitations
DSSC	15.2% [24]	Low cost, operate in low light and wider angles, work at lower internal temperature conditions, robustness and long life	Temperature stability issues, toxic and volatile compound
PVSC	25.7% [UNIST] ¹	Cheap and simple in construction, lightweight, flexible, high efficiency, low production cost	Unstable
QDS	18.1% [UNIST]	Low production cost, low power consumption	Highly toxic in nature, degradation
TSC	32.5% [NREL]	High efficiency	Complex, costly
OSC	18.20% [433]	Low processing cost, light weight, flexible, thermally stable	Low efficiency

Improvements in DSSC efficiency are possible with the discovery of novel dyes and inorganic nanomaterials. Additionally, the study of different approaches to enhance dye loading and stability will be of assistance to some extent. Designing a new molecular dye, using two terminal architectures of Si along with DSSC, can result in higher device efficiency. Solar hydrogen production employing DSSCs is an exciting emerging field that holds great promise. Furthermore, the integrated device techniques of DSSCs with PSCs are another promising technology for the development of next-generation devices.

For PSCs, the development of new perovskite structure materials using theoretical and experimental methods is required to advance from the current state. PSCs with tandem architecture appear to be a more promising approach. Within this context, perovskite materials with large bandgaps, as well as small bandgaps, are being investigated for use as top cells. Theoretical predictions suggest that the Si-perovskite tandem architecture has the potential to achieve an efficiency of up to 31% [21], which is a promising development for the commercialization of this product. By using a reliable deposition method, stable layers, novel materials, and new tandem approaches, this technology will enter into a new era.

In the field of QDSSCs, materials, sensitization methods, and improvements in sensitizers, electrolytes, and counter electrodes have captured the interest of researchers, and extensive research is currently underway in various disciplines. Lead chalcogenide nanomaterials have demonstrated remarkable stability in comparison to other types of nanoparticles. Consequently, their potential for long-term utilization has drawn significant attention and is currently under investigation. It is expected that the efficiency of inorganic nanoparticle-based SCs might exceed that of the same materials in bulk thin-film structures by mitigating surface recombination. Furthermore, additional surface engineering methods should be applied to nanocrystalline thin films to improve their photon-absorbing capabilities. Commercialization of organic solar cells remains a difficult task due to stability difficulties, even though they are manufactured using modern processes including roll-to-roll manufacturing and inkjet printing. Combining organic solar cells with emerging SC technologies, such as PSCs, would be advantageous for space and other uses in the future.

9. Conclusions

Third generation SCs have tremendous potential as primary sources to meet energy demands. This review article provides a detailed study of the current status of third-

generation SC, namely DSSC, PSC, QDSSC, TCS, and OPVs. Apart from these cells, other third-generation techniques, such as UC, DC, DS, multi-exciton generation, hot carrier, and intermediate band, are also highlighted. In contrast to traditional SCs, these SCs do not use a p-n junction for the production of electrical energy. This review highlights not only different fabrication techniques used to improve efficiencies but also the challenges of commercializing these third-generation technologies. In theory, they are cheaper than silicon-based solar cells and can achieve efficiencies beyond the Shockley–Queisser limit. However, an extensive amount of research is required to improve the stability of these cells as it is a major hurdle on the path to their commercialization.

The ideas that have been brought forth in discussions about solar cells of the third generation appear to be taking the solar energy market by storm. From the perspective that has been presented, it is very obvious that nanomaterials are a boon to the current research to develop highly efficient SCs at a low cost. A solid platform needs to be established to construct solar cells employing nanomaterials, even though the scientific community may be addressing the issues at hand using a variety of methods. PSCs have shown remarkable efficiency gains in recent years, revealing a viable path for high-efficiency, large-area modules.

Possibly serious measures should be taken to address setbacks caused by the high price of raw materials. The high price of flexible substrates is a barrier to developing cost-effective, next-generation solar cells. To increase potential for commercialization, industrial methods will need to be augmented with novel materials, such as roll-to-roll fabrication and inkjet printing of multiple layers. To further boost efficiency, new materials are needed that can capture light in the near-infrared spectrum. Using a colloidal synthesis approach, such novel materials for high-efficiency SCs can be developed. Functionalizing various inorganic semiconductor nanostructures, organic polymers, and dyes with appropriate molecules, it is still possible to achieve the aim of capturing an immense number of photons.

Author Contributions: Conceptualization, N.S. and A.A.S.; methodology, N.S. and A.A.S.; investigation, N.S., A.A.S. and S.K.; resources, A.A.S., P.K.L., K.S., Q.L. and X.Z.; data curation, N.S., A.A.S., P.K.L., K.S. and S.K.; writing—original draft preparation, N.S. and A.A.S.; writing—review and editing, All authors; supervision, A.A.S.; project administration, A.A.S., P.K.L., Q.L. and X.Z.; funding acquisition, A.A.S., P.K.L., Q.L. and X.Z. All authors have read and agreed to the published version of the manuscript.

Funding: This work was supported by the Creative Research Groups of the National Natural Science Foundation of China (No. 52021004).

Institutional Review Board Statement: Not applicable.

Informed Consent Statement: Not applicable.

Data Availability Statement: No new data were created or analyzed in this study. Data sharing is not applicable to this article.

Conflicts of Interest: The authors declare no conflict of interest.

References

1. Huang, Y.; Kuldashaeva, Z.; Bobojanov, S.; Djalilov, B.; Salahodjaev, R.; Abbas, S. Exploring the links between fossil fuel energy consumption, industrial value-added, and carbon emissions in G20 countries. *Environ. Sci. Pollut. Res.* **2022**, *30*, 10854–10866. [[CrossRef](#)] [[PubMed](#)]
2. Zhang, D.; Zheng, M.; Feng, G.F.; Chang, C.P. Does an environmental policy bring to green innovation in renewable energy? *Renew. Energy* **2022**, *195*, 1113–1124. [[CrossRef](#)]
3. Sadiqa, A.; Gulagi, A.; Bogdanov, D.; Caldera, U.; Breyer, C. Renewable energy in Pakistan: Paving the way towards a fully renewables-based energy system across the power, heat, transport and desalination sectors by 2050. *IET Renew. Power Gener.* **2022**, *16*, 177–197. [[CrossRef](#)]
4. Green, M.A.; Dunlop, E.D.; Hohl-Ebinger, J.; Yoshita, M.; Kopidakis, N.; Hao, X. Solar cell efficiency tables (Version 58). *Prog. Photovolt. Res. Appl.* **2021**, *29*, 657–667. [[CrossRef](#)]
5. Bhattacharya, S.; John, S. Beyond 30% conversion efficiency in silicon solar cells: A numerical demonstration. *Sci. Rep.* **2019**, *9*, 12482–12515. [[CrossRef](#)]

6. Le Donne, A.; Trifiletti, V.; Binetti, S. New earth-abundant thin film solar cells based on chalcogenides. *Front. Chem.* **2019**, *7*, 297. [[CrossRef](#)]
7. Ramanujam, J.; Bishop, D.M.; Todorov, T.K.; Gunawan, O.; Rath, J.; Nekovei, R.; Romeo, A. Flexible CIGS, CdTe and a-Si: H based thin film solar cells: A review. *Prog. Mater. Sci.* **2020**, *110*, 100619. [[CrossRef](#)]
8. Meredith, P.; Armin, A. Scaling of next generation solution processed organic and perovskite solar cells. *Nat. Commun.* **2018**, *9*, 5261. [[CrossRef](#)] [[PubMed](#)]
9. Jayawardena, K.D.G.I.; Silva, S.M.; Misra, R.K. Solution processed perovskite incorporated tandem photovoltaics: Developments, manufacturing, and challenges. *J. Mater. Chem. C* **2020**, *8*, 10641–10675. [[CrossRef](#)]
10. Green, M.A. *Third Generation Photovoltaics*; Springer: New York, NY, USA, 2003.
11. Jiang, W.; Ni, X.; Liu, F. Exotic topological bands and quantum states in metal–organic and covalent–organic frameworks. *Acc. Chem. Res.* **2021**, *54*, 416–426. [[CrossRef](#)] [[PubMed](#)]
12. Zhang, Y.; Park, N.G. A thin film (<200 nm) perovskite solar cell with 18% efficiency. *J. Mater. Chem. A* **2020**, *8*, 17420–17428.
13. Green, M.; Dunlop, E.; Hohl-Ebinger, J.; Yoshita, M.; Kopidakis, N.; Hao, X. Solar cell efficiency tables (version 57). *Prog. Photovolt. Res. Appl.* **2021**, *29*, 3–15. [[CrossRef](#)]
14. Ji, J.M.; Zhou, H.; Eom, Y.K.; Kim, C.H.; Kim, H.K. 14.2% efficiency dye-sensitized solar cells by co-sensitizing novel thieno [3,2-*b*]indole-based organic dyes with a promising porphyrin sensitizer. *Adv. Energy Mater.* **2020**, *10*, 2000124. [[CrossRef](#)]
15. Gao, X.X.; Luo, W.; Zhang, Y.; Hu, R.; Zhang, B.; Züttel, A.; Nazeeruddin, M.K. Stable and high-efficiency methylammonium-free perovskite solar cells. *Adv. Mater.* **2020**, *32*, 1905502. [[CrossRef](#)]
16. Zhang, M.; Wu, F.; Chi, D.; Shi, K.; Huang, S. High-efficiency perovskite solar cells with poly (vinylpyrrolidone)-doped SnO₂ as an electron transport layer. *Mater. Adv.* **2020**, *1*, 617–624. [[CrossRef](#)]
17. Sirtl, M.T.; Hooijer, R.; Armer, M.; Ebadi, F.G.; Mohammadi, M.; Maheu, C.; Bein, T. 2D/3D Hybrid Cs₂AgBiBr₆ Double Perovskite Solar Cells: Improved Energy Level Alignment for Higher Contact-Selectivity and Large Open Circuit Voltage. *Adv. Energy Mater.* **2022**, *12*, 2103215. [[CrossRef](#)]
18. Chiang, Y.H.; Lin, K.Y.; Chen, Y.H.; Waki, K.; Abate, M.A.; Jiang, J.C.; Chang, J.Y. Aqueous solution-processed off-stoichiometric Cu–In–S QDs and their application in quantum dot-sensitized solar cells. *J. Mater. Chem. A* **2018**, *6*, 9629–9641. [[CrossRef](#)]
19. Rasal, A.S.; Yadav, S.; Kashale, A.A.; Altaee, A.; Chang, J.Y. Stability of quantum dot-sensitized solar cells: A review and prospects. *Nano Energy* **2021**, *94*, 106854. [[CrossRef](#)]
20. Kant, N.; Singh, P. Review of next generation photovoltaic solar cell technology and comparative materialistic development. *Mater. Today Proc.* **2022**, *56*, 3460–3470. [[CrossRef](#)]
21. He, Y.; Li, N.; Heumüller, T.; Wortmann, J.; Hanisch, B.; Aubele, A.; Lucas, S.; Feng, G.; Jiang, X.; Li, W.; et al. Industrial viability of single-component organic solar cells. *Joule* **2022**, *6*, 1160–1171. [[CrossRef](#)]
22. Lamkaouane, H.; Ftouhi, H.; Louarn, G.; Mir, Y.; Morsli, M.; Addou, M.; Cattin, L.; Bernède, J.C. Investigation of the different possible energy band structure configurations for planar heterojunction organic solar cells. *Solid-State Electron.* **2022**, *191*, 108254. [[CrossRef](#)]
23. Dash, B.P.; Beriha, S.K.; Naik, B.; Sahoo, P.K. Organic materials based solar cells. *Mater. Today Proc.* **2022**, *67*, 1057–1063. [[CrossRef](#)]
24. Ren, Y.; Zhang, D.; Suo, J.; Cao, Y.; Eickemeyer, F.T.; Vlachopoulos, N.; Grätzel, M. Hydroxamic acid pre-adsorption raises the efficiency of cosensitized solar cells. *Nature* **2023**, *613*, 60–65. [[CrossRef](#)]
25. Kojima, A.; Teshima, K.; Shirai, Y.; Miyasaka, T. Organometal halide perovskites as visible-light sensitizers for photovoltaic cells. *J. Am. Chem. Soc.* **2009**, *131*, 6050–6051. [[CrossRef](#)]
26. He, C.; Pan, Y.; Ouyang, Y.; Shen, Q.; Gao, Y.; Yan, K.; Chen, H. Manipulating the D: A interfacial energetics and intermolecular packing for 19.2% efficiency organic photovoltaics. *Energy Environ. Sci.* **2022**, *15*, 2537–2544. [[CrossRef](#)]
27. Khalid, S.; Sultan, M.; Ahmed, E.; Ahmed, W. Third-generation solar cells. In *Emerging Nanotechnologies for Renewable Energy*; Elsevier: Amsterdam, The Netherlands, 2021; pp. 3–35.
28. Niu, G.; Guo, X.; Wang, L. Review of recent progress in chemical stability of perovskite solar cells. *J. Mater. Chem. A* **2015**, *3*, 8970–8980. [[CrossRef](#)]
29. Sharma, D.; Jha, R.; Kumar, S. Quantum dot sensitized solar cell: Recent advances and future perspectives in photoanode. *Sol. Energy Mater. Sol. Cells* **2016**, *155*, 294–322. [[CrossRef](#)]
30. Li, S.; Zhang, H.; Yue, S.; Yu, X.; Zhou, H. Recent advances in non-fullerene organic photovoltaics enabled by green solvent processing. *Nanotechnology* **2021**, *33*, 072002. [[CrossRef](#)]
31. Tyagi, P.K.; Singh, V. N-type diamane: An effective emitter layer in crystalline Si heterojunction solar cell. *Carbon Trends* **2022**, *9*, 100209.
32. Zouhair, S.; Luo, B.; Bogachuk, D.; Martineau, D.; Wagner, L.; Chahboun, A.; Hinsch, A. Fill Factor Assessment in Hole Selective Layer Free Carbon Electrode-Based Perovskite Solar Cells with 15.5% Certified Power Conversion Efficiency. *Sol. RRL* **2022**, *6*, 2100745. [[CrossRef](#)]
33. Kataria, V.; Mehta, D.S. Multispectral harvesting rare-earth oxysulphide based highly efficient transparent luminescent solar concentrator. *J. Rare Earths* **2022**, *40*, 41–48. [[CrossRef](#)]
34. AbdElAziz, H. Performance Evaluation of Free Hole Transport Layer CsPbI₃ Perovskite Solar cells. *J. Mater. Sci. Mater. Electron.* **2023**, *34*, 470. [[CrossRef](#)]

35. Yin, S.; Wang, J.; Li, Z.; Fang, X. State-of-the-art short-term electricity market operation with solar generation: A review. *Renew. Sustain. Energy Rev.* **2021**, *138*, 110647. [[CrossRef](#)]
36. Agrawal, A.; Siddiqui, S.A.; Soni, A.; Sharma, G.D. Advancements, frontiers and analysis of metal oxide semiconductor, dye, electrolyte and counter electrode of dye sensitized solar cell. *Sol. Energy* **2022**, *233*, 378–407. [[CrossRef](#)]
37. Yang, J.; Siempelkamp, B.D.; Liu, D.; Kelly, T.L. Investigation of $\text{CH}_3\text{NH}_3\text{PbI}_3$ Degradation Rates and Mechanisms in Controlled Humidity Environments Using in Situ Techniques. *ACS Nano* **2015**, *9*, 1955–1963. [[CrossRef](#)]
38. Gorjian, S.; Bousi, E.; Özdemir, Ö.E.; Trommsdorff, M.; Kumar, N.M.; Anand, A.; Chopra, S.S. Progress and challenges of crop production and electricity generation in agrivoltaic systems using semi-transparent photovoltaic technology. *Renew. Sustain. Energy Rev.* **2022**, *158*, 112126. [[CrossRef](#)]
39. Kumar, S.; Muthu, S.; Sekar, S.; Bathula, C.; Kalamurthy, A.K.; Lee, S. Metal chalcogenide-based counter electrodes for dye-sensitized solar cells. *Oxide Free. Nanomater. Energy Storage Convers. Appl.* **2022**, 259–286.
40. Brian, O.; Grätzel, M. A low-cost, high-efficiency solar cell based on dye-sensitized colloidal TiO_2 films. *Nature* **1991**, *353*, 737–740.
41. Aljafari, B.; Vijaya, S.; Takshi, A.; Anandan, S. Copper doped manganese dioxide as counter electrode for dye-sensitized solar cells. *Arab. J. Chem.* **2022**, *15*, 104068. [[CrossRef](#)]
42. Mir, N.; Salavati-Niasari, M. Photovoltaic properties of corresponding dye sensitized solar cells: Effect of active sites of growth controller on TiO_2 nanostructures. *Sol. Energy* **2012**, *86*, 3397–3404. [[CrossRef](#)]
43. Ito, S.; Nazeeruddin, M.K.; Liska, P.; Comte, P.; Charvet, R.; Péchy, P.; Grätzel, M. Photovoltaic characterization of dye-sensitized solar cells: Effect of device masking on conversion efficiency. *Prog. Photovolt. Res. Appl.* **2006**, *14*, 589–601. [[CrossRef](#)]
44. Nazeeruddin, M.K.; Baranoff, E.; Grätzel, M. Dye-sensitized solar cells: A brief overview. *Sol. Energy* **2011**, *85*, 1172–1178. [[CrossRef](#)]
45. Kim, I.D.; Hong, J.M.; Lee, B.H.; Kim, D.Y.; Jeon, E.K.; Choi, D.K.; Yang, D.J. Dye-sensitized solar cells using network structure of electrospun ZnO nanofiber mats. *Appl. Phys. Lett.* **2007**, *91*, 163109. [[CrossRef](#)]
46. Li, H.; Zhang, Y.; Wang, J. ZnO nanosheets derived from surfactant-directed process: Growth mechanism, and application in dye-sensitized solar cells. *J. Am. Ceram. Soc.* **2012**, *95*, 1241–1246. [[CrossRef](#)]
47. Lu, L.; Li, R.; Fan, K.; Peng, T. Effects of annealing conditions on the photoelectrochemical properties of dye-sensitized solar cells made with ZnO nanoparticles. *Sol. Energy* **2010**, *84*, 844–853. [[CrossRef](#)]
48. Giannouli, M.; Spiliopoulou, F. Effects of the morphology of nanostructured ZnO films on the efficiency of dye-sensitized solar cells. *Renew. Energy* **2012**, *41*, 115–122. [[CrossRef](#)]
49. Zhang, Q.; Dandeneau, C.S.; Zhou, X.; Cao, G. ZnO nanostructures for dye-sensitized solar cells. *Adv. Mater.* **2009**, *21*, 4087–4108. [[CrossRef](#)]
50. Luo, J.; Xie, Z.; Zou, J.; Wu, X.; Gong, X.; Li, C.; Xie, Y. Efficient dye-sensitized solar cells based on concerted companion dyes: Systematic optimization of thiophene units in the organic dye components. *Chin. Chem. Lett.* **2022**, *33*, 4313–4316. [[CrossRef](#)]
51. Cortés, E.; Wendisch, F.J.; Sortino, L.; Mancini, A.; Ezendam, S.; Saris, S.; Maier, S.A. Optical metasurfaces for energy conversion. *Chem. Rev.* **2022**, *122*, 15082–15176. [[CrossRef](#)]
52. Cole, J.M.; Pepe, G.; Al Bahri, O.K.; Cooper, C.B. Cosensitization in dye-sensitized solar cells. *Chem. Rev.* **2019**, *119*, 7279–7327. [[CrossRef](#)]
53. Sugathan, V.; John, E.; Sudhakar, K. Recent improvements in dye sensitized solar cells: A review. *Renew. Sustain. Energy Rev.* **2015**, *52*, 54–64. [[CrossRef](#)]
54. Maddah, H.A.; Berry, V.; Behura, S.K. Biomolecular photosensitizers for dye-sensitized solar cells: Recent developments and critical insights. *Renew. Sustain. Energy Rev.* **2020**, *121*, 109678. [[CrossRef](#)]
55. Aslam, A.; Mehmood, U.; Arshad, M.H.; Ishfaq, A.; Zaheer, J.; Khan AU, H.; Sufyan, M. Dye-sensitized solar cells (DSSCs) as a potential photovoltaic technology for the self-powered internet of things (IoTs) applications. *Sol. Energy* **2020**, *207*, 874–892. [[CrossRef](#)]
56. Yan, N.; Zhao, C.; You, S.; Zhang, Y.; Li, W. Recent progress of thin-film photovoltaics for indoor application. *Chin. Chem. Lett.* **2020**, *31*, 643–653. [[CrossRef](#)]
57. Chiba, Y.; Islam, A.; Watanabe, Y.; Komiya, R.; Koide, N.; Han, L. Dye-sensitized solar cells with conversion efficiency of 11.1%. *Jpn. J. Appl. Phys.* **2006**, *45*, L638. [[CrossRef](#)]
58. Ko, S.H.; Lee, D.; Kang, H.W.; Nam, K.H.; Yeo, J.Y.; Hong, S.J.; Sung, H.J. Nanoforest of hydrothermally grown hierarchical ZnO nanowires for a high efficiency dye-sensitized solar cell. *Nano Lett.* **2011**, *11*, 666–671. [[CrossRef](#)]
59. Han, L.; Islam, A.; Chen, H.; Malapaka, C.; Chiranjeevi, B.; Zhang, S.; Yanagida, M. High-efficiency dye-sensitized solar cell with a novel co-adsorbent. *Energy Environ. Sci.* **2012**, *5*, 6057–6060. [[CrossRef](#)]
60. Kakiage, K.; Aoyama, Y.; Yano, T.; Oya, K.; Fujisawa, J.I.; Hanaya, M. Highly-efficient dye-sensitized solar cells with collaborative sensitization by silyl-anchor and carboxy-anchor dyes. *Chem. Commun.* **2015**, *51*, 15894–15897. [[CrossRef](#)]
61. Devadiga, D.; Selvakumar, M.; Shetty, P.; Santosh, M.S. The integration of flexible dye-sensitized solar cells and storage devices towards wearable self-charging power systems: A review. *Renew. Sustain. Energy Rev.* **2022**, *159*, 112252. [[CrossRef](#)]
62. Dwivedi, G.; Munjal, G.; Bhaskarwar, A.N.; Chaudhary, A. Dye-sensitized solar cells with polyaniline: A review. *Inorg. Chem. Commun.* **2022**, *135*, 109087. [[CrossRef](#)]
63. Moharam, M.M.; El Shazly, A.N.; Anand, K.V.; Rayan, D.E.; Mohammed, M.K.; Rashad, M.M.; Shalan, A.E. Semiconductors as effective electrodes for dye sensitized solar cell applications. *Top. Curr. Chem.* **2021**, *379*, 20. [[CrossRef](#)] [[PubMed](#)]

64. Boucle, J.; Ackermann, J. Solid-state dye-sensitized and bulk heterojunction solar cells using TiO₂ and ZnO nanostructures: Recent progress and new concepts at the borderline. *Polym. Int.* **2012**, *61*, 355–373. [CrossRef]
65. Hočevár, M.; Krašovec, U.O.; Bokalič, M.; Topič, M.; Veurman, W.; Brandt, H.; Hinsch, A. Sol-gel based TiO₂ paste applied in screen-printed dye-sensitized solar cells and modules. *J. Ind. Eng. Chem.* **2013**, *19*, 1464–1469. [CrossRef]
66. Fan, K.; Liu, M.; Peng, T.; Ma, L.; Dai, K. Effects of paste components on the properties of screen-printed porous TiO₂ film for dye-sensitized solar cells. *Renew. Energy* **2010**, *35*, 555–561. [CrossRef]
67. Baglio, V.; Girolamo, M.; Antonucci, V.; Aricò, A. Influence of TiO₂ film thickness on the electrochemical behaviour of dye-sensitized solar cells. *Int. J. Electrochem. Sci.* **2011**, *6*, 3375–3384.
68. Zhang, Y.; Wu, L.; Xie, E.; Duan, H.; Han, W.; Zhao, J. A simple method to prepare uniform-size nanoparticle TiO₂ electrodes for dye-sensitized solar cells. *J. Power Sources* **2009**, *189*, 1256–1263. [CrossRef]
69. Luo, P.; Niu, H.; Zheng, G.; Bai, X.; Zhang, M.; Wang, W. Enhancement of photoelectric conversion by high-voltage electric field assisted crystallization of a novel ternary-encapsulated spherical TiO₂ aggregate for solar cells. *Electrochim. Acta* **2010**, *55*, 2697–2705. [CrossRef]
70. Mondal, B.; Usha, K.; Mahata, S.; Kumbhakar, P.; Nandi, M.M. Synthesis and characterization of nanocrystalline TiO₂ thin films for use as photoelectrodes in dye sensitized solar cell application. *Trans. Indian Ceram. Soc.* **2011**, *70*, 173–177. [CrossRef]
71. Roy, A.; Mukhopadhyay, S.; Devi, P.S.; Sundaram, S. Polyaniline-layered rutile TiO₂ nanorods as alternative photoanode in dye-sensitized solar cells. *ACS Omega* **2019**, *4*, 1130–1138. [CrossRef]
72. Yadav, S.K.; Kumari, R.; Gunsaria, R.K. Role of Dye Photosensitizer and Surfactant in Solar Energy: A Review. *J. Adv. Sci. Res.* **2022**, *13*, 12–18. [CrossRef]
73. Kabir, F.; Manir, S.; Bhuiyan, M.M.H.; Aftab, S.; Ghanbari, H.; Hasani, A.; Adachi, M.M. Instability of dye-sensitized solar cells using natural dyes and approaches to improving stability—An overview. *Sustain. Energy Technol. Assess.* **2022**, *52*, 102196. [CrossRef]
74. Hegazy, B.M.; Othman, H.; Hassabo, A.G. Polycation Natural Materials for Improving Textile Dyeability and Functional Performance. *J. Text. Color. Polym. Sci.* **2022**, *19*, 155–178. [CrossRef]
75. Dokoohaki, M.H.; Zolghadr, A.R.; Klein, A. Highly Efficient Dye-Sensitized Solar Cells Based on Electrolyte Solutions Containing Choline Chloride/Ethylene Glycol Deep Eutectic Solvent: Electrolyte Optimization. *Ind. Eng. Chem. Res.* **2022**, *61*, 11464–11473. [CrossRef]
76. Kong, F.T.; Dai, S.Y.; Wang, K.J. Review of recent progress in dye-sensitized solar cells. *Adv. Optoelectron.* **2007**, *2007*, 75384. [CrossRef]
77. Sasi, S.; Sajeev, A.; Sugunan, S.K.; Nair, P.R.; Mathew, S. Dye-Sensitized Solar Cells Based on a New Type of Non-Volatile Co (II)/Co (III) Electrolyte Delivering Higher Power Conversion Efficiency for Indoor Applications. *Micro Nanosyst.* **2022**, *14*, 77–82. [CrossRef]
78. Chang, H.; Chen, T.L.; Huang, K.D.; Chien, S.H.; Hung, K.C. Fabrication of highly efficient flexible dye-sensitized solar cells. *J. Alloys Compd.* **2010**, *504*, S435–S438. [CrossRef]
79. Zheng, H.; Tachibana, Y.; Kalantar-Zadeh, K. Dye-sensitized solar cells based on WO₃. *Langmuir* **2010**, *26*, 19148–19152. [CrossRef]
80. Kumari, J.M.K.W.; Senadeera, G.K.R.; Weerasinghe, A.M.J.S.; Thotawatthage, C.A.; Dissanayake, M.A.K.L. Effect of polyaniline (PANI) on efficiency enhancement of dye-sensitized solar cells fabricated with poly (ethylene oxide)-based gel polymer electrolytes. *J. Solid State Electrochem.* **2021**, *25*, 695–705. [CrossRef]
81. Mozaffari, S.; Nateghi, M.R.; Zarandi, M.B. An overview of the Challenges in the commercialization of dye sensitized solar cells. *Renew. Sustain. Energy Rev.* **2017**, *71*, 675–686. [CrossRef]
82. Aftabuzzaman, M.; Kim, H.K. Porous carbon materials as supreme metal-free counter electrode for dye-sensitized solar cells. In *Emerging Solar Energy Materials*; IntechOpen: London, UK, 2018; Volume 4.
83. Wu, J.; Lan, Z.; Lin, J.; Huang, M.; Huang, Y.; Fan, L.; Wei, Y. Counter electrodes in dye-sensitized solar cells. *Chem. Soc. Rev.* **2017**, *46*, 5975–6023. [CrossRef]
84. Sharma, S.; Siwach, B.; Ghoshal, S.K.; Mohan, D. Dye sensitized solar cells: From genesis to recent drifts. *Renew. Sustain. Energy Rev.* **2017**, *70*, 529–537. [CrossRef]
85. Zhang, H.; Zhou, J.; Zang, X.F.; Hong, Y.P.; Chen, Z.E. An efficient strategy for designing high-performance DSSCs: Using the terminal auxiliary acceptor to improve electronic transitions. *Dye. Pigment.* **2022**, *206*, 110642. [CrossRef]
86. Ma, J.; Li, C.; Yu, F.; Chen, J. 3D Single-Walled Carbon Nanotube/GrapheneAerogels as Pt-Free Transparent Counter Electrodes for High Efficiency Dye-Sensitized Solar Cells. *ChemSusChem* **2014**, *7*, 3304–3311. [CrossRef] [PubMed]
87. Yang, J.; Ganesan, P.; Teuscher, J.; Moehl, T.; Kim, Y.J.; Yi, C.; Grätzel, M. Influence of the donor size in D–π–A organic dyes for dye-sensitized solar cells. *J. Am. Chem. Soc.* **2014**, *136*, 5722–5730. [CrossRef] [PubMed]
88. Noh, Y.; Song, O. Properties of an Au/Pt bilayered counter electrode in dye sensitized solar cells. *Electron. Mater. Lett.* **2014**, *10*, 981–984. [CrossRef]
89. Dayan, S.; Kayaci, N.; Özpozan, N.K. Improved performance with molecular design of Ruthenium (II) complexes bearing diamine-based bidentate ligands as sensitizer for dye-sensitized solar cells (DSSC). *J. Mol. Struct.* **2020**, *1209*, 127920. [CrossRef]
90. Kumar, V.; Gupta, R.; Bansal, A. Role of chenodeoxycholic acid as co-additive in improving the efficiency of DSSCs. *Sol. Energy* **2020**, *196*, 589–596. [CrossRef]

91. Zatirostami, A. Increasing the efficiency of TiO₂-based DSSC by means of a double layer RF- sputtered thin film blocking layer. *Optik* **2020**, *207*, 164419. [[CrossRef](#)]
92. Elmorsy, M.R.; Abdel-Latif, E.; Badawy, S.A.; Fadda, A.A. Molecular geometry, synthesis and photovoltaic performance studies over 2-cyanoacetanilides as sensitizers and effective co-sensitizers for DSSCs loaded with HD-2. *J. Photochem. Photobiol. A Chem.* **2020**, *389*, 112239. [[CrossRef](#)]
93. Pinto, A.L.; Cruz, L.; Gomes, V.; Cruz, H.; Calogero, G.; de Freitas, V.; Pina, F.; Parola, A.J.; Lima, J.C. Catechol versus carboxyl linkage impact on DSSC performance of synthetic pyranoflavylum salts. *Dye. Pigment.* **2019**, *170*, 107577. [[CrossRef](#)]
94. Diantoro, M.; Maftuha, D.; Suprayogi, T.; Iqbal, M.R.; Solehudin; Mufti, N.; Taufiq, A.; Hidayat, A.; Suryana, R.; Hidayat, R. Performance of pterocarpus indicus willd leaf extract as natural dye TiO₂-Dye/ITO DSSC. *Mater. Today Proc.* **2019**, *17*, 1268–1276. [[CrossRef](#)]
95. Raïssi, M.; Pellegrin, Y.; Lefevre, F.X.; Boujtita, M.; Rousseau, D.; Berthelot, T.; Odobel, F. Digital printing of efficient dye-sensitized solar cells (DSSCs). *Sol. Energy* **2020**, *199*, 92–99. [[CrossRef](#)]
96. Jie, J.; Xu, Q.; Yang, G.; Feng, Y.; Zhang, B. Porphyrin sensitizers involving a fluorine-substituted benzothiadiazole as auxiliary acceptor and thiophene as π bridge for use in dye-sensitized solar cells (DSSCs). *Dye. Pigment.* **2020**, *174*, 107984. [[CrossRef](#)]
97. Arslan, B.S.; Güzel, E.; Kaya, T.; Durmaz, V.; Keskin, M.; Avcı, D.; Nebioğlu, M.; Şişman, İ. Novel D- π -A organic dyes for DSSCs based on dibenzo [b, h][1, 6] naphthyridine as a π -bridge. *Dye. Pigment.* **2019**, *164*, 188–197. [[CrossRef](#)]
98. Zhang, H.; Chen, Z.-E.; Tian, H.-R. Molecular engineering of metal-free organic sensitizers with polycyclic benzenoid hydrocarbon donor for DSSC applications: The effect of the conjugate mode. *Sol. Energy* **2020**, *198*, 239–246. [[CrossRef](#)]
99. Gullace, S.; Nastasi, F.; Puntoriero, F.; Trusso, S.; Calogero, G. A platinum-free nanostructured gold counter electrode for DSSCs prepared by pulsed laser ablation. *Appl. Surf. Sci.* **2020**, *506*, 144690. [[CrossRef](#)]
100. Ferreira, F.; Babu, R.S.; Barros, A.; Raja, S.; da Conceição, L.; Mattoso, L. Photoelectric performance evaluation of DSSCs using the dye extracted from different color petals of *Leucanthemum vulgare* flowers as novel sensitizers. *Spectrochim. Acta Part A Mol. Biomol. Spectrosc.* **2020**, *233*, 118198. [[CrossRef](#)]
101. Basumatary, P.; Agarwal, P. A short review on progress in perovskite solar cells. *Mater. Res. Bull.* **2022**, *149*, 111700. [[CrossRef](#)]
102. Sharma, D.; Mehra, R.; Raj, B. Design and comparative analysis of various planar perovskite solar cells through numerical simulation using different HTLs to improve efficiency. *Opt. Mater.* **2022**, *126*, 112221. [[CrossRef](#)]
103. Yang, X.; Zhang, X.; Deng, J.; Chu, Z.; Jiang, Q.; Meng, J.; You, J. Efficient green light-emitting diodes based on quasi-two-dimensional composition and phase engineered perovskite with surface passivation. *Nat. Commun.* **2018**, *9*, 570. [[CrossRef](#)] [[PubMed](#)]
104. Kim, H.; Zhao, L.; Price, J.S.; Grede, A.J.; Roh, K.; Brigeman, A.N.; Giebink, N.C. Hybrid perovskite light emitting diodes under intense electrical excitation. *Nat. Commun.* **2018**, *9*, 4893. [[CrossRef](#)] [[PubMed](#)]
105. Ricciardulli, A.G.; Yang, S.; Smet, J.H.; Saliba, M. Emerging perovskite monolayers. *Nat. Mater.* **2021**, *20*, 1325–1336. [[CrossRef](#)] [[PubMed](#)]
106. Tailor, N.K.; Kar, S.; Mishra, P.; These, A.; Kupfer, C.; Hu, H.; Satapathi, S. Advances in lead-free perovskite single crystals: Fundamentals and applications. *ACS Mater. Lett.* **2021**, *3*, 1025–1080. [[CrossRef](#)]
107. Yan, P.; Yang, D.; Wang, H.; Yang, S.; Ge, Z. Recent advances in dopant-free organic hole-transporting materials for efficient, stable and low-cost perovskite solar cells. *Energy Environ. Sci.* **2022**, *15*, 3630–3669. [[CrossRef](#)]
108. Etgar, L.; Gao, P.; Xue, Z.; Peng, Q.; Chandiran, A.K.; Liu, B.; Grätzel, M. Mesoscopic CH₃NH₃PbI₃/TiO₂ heterojunction solar cells. *J. Am. Chem. Soc.* **2012**, *134*, 17396–17399. [[CrossRef](#)]
109. Jiang, Y.; Green, M.A.; Sheng, R.; Ho-Baillie, A. Room temperature optical properties of organic–inorganic lead halide perovskites. *Sol. Energy Mater. Sol. Cells* **2015**, *137*, 253–257. [[CrossRef](#)]
110. Lin, Q.; Armin, A.; Nagiri RC, R.; Burn, P.L.; Meredith, P. Electro-optics of perovskite solar cells. *Nat. Photonics* **2015**, *9*, 106–112. [[CrossRef](#)]
111. Quarti, C.; Mosconi, E.; Ball, J.M.; D’Innocenzo, V.; Tao, C.; Pathak, S.; De Angelis, F. Structural and optical properties of methylammonium lead iodide across the tetragonal to cubic phase transition: Implications for perovskite solar cells. *Energy Environ. Sci.* **2016**, *9*, 155–163. [[CrossRef](#)]
112. Löper, P.; Stuckelberger, M.; Niesen, B.; Werner, J.; Filipič, M.; Moon, S.J.; Ballif, C. Complex Refractive Index Spectra of CH₃NH₃PbI₃ Perovskite Thin Films Determined by Spectroscopic Ellipsometry and Spectrophotometry. *J. Phys. Chem. Lett.* **2014**, *6*, 66–71. [[CrossRef](#)]
113. Yin, W.J.; Shi, T.; Yan, Y. Unusual defect physics in CH₃NH₃PbI₃ perovskite solar cell absorber. *Appl. Phys. Lett.* **2014**, *104*, 063903. [[CrossRef](#)]
114. Shirayama, M.; Kato, M.; Miyadera, T.; Sugita, T.; Fujiseki, T.; Hara, S.; Fujiwara, H. Degradation mechanism of CH₃NH₃PbI₃ perovskite materials upon exposure to humid air. *J. Appl. Phys.* **2016**, *119*, 115501. [[CrossRef](#)]
115. Nemnes, G.A.; Besleaga, C.; Tomulescu, A.G.; Pintilie, I.; Pintilie, L.; Torfason, K.; Manolescu, A. Dynamic electrical behavior of halide perovskite based solar cells. *Sol. Energy Mater. Sol. Cells* **2017**, *159*, 197–203. [[CrossRef](#)]
116. Hamukwaya, S.L.; Hao, H.; Zhao, Z.; Dong, J.; Zhong, T.; Xing, J.; Mashingaidze, M.M. A Review of Recent Developments in Preparation Methods for Large-Area Perovskite Solar Cells. *Coatings* **2022**, *12*, 252. [[CrossRef](#)]
117. Berger, E.; Bagheri, M.; Asgari, S.; Zhou, J.; Kokkonen, M.; Talebi, P.; Hashmi, S.G. Recent developments in perovskite-based precursor inks for scalable architectures of perovskite solar cell technology. *Sustain. Energy Fuels* **2022**, *6*, 2879–2900. [[CrossRef](#)]

118. Reddy, P.V.; Giri, P.; Tiwari, J.P. Degradation conceptualization of an innovative perovskite solar cell fabricated using SnO₂ and P3HT as electron and hole transport layers. *New J. Chem.* **2022**, *46*, 12751–12766. [[CrossRef](#)]
119. Tonui, P.; Oseni, S.O.; Sharma, G.; Yan, Q.; Mola, G.T. Perovskites photovoltaic solar cells: An overview of current status. *Renew. Sustain. Energy Rev.* **2018**, *91*, 1025–1044. [[CrossRef](#)]
120. Shah, A.A.; Khan, M.A.; Raj, V.; Gupta, A. Intervention of Nanotechnology as a Tool for Enhanced Renewable Energy Application in the Field of Solar Power Harnessing. In *Environmental Security and Sustainable Development*; Discovery Publishing House Pvt. Ltd.: New Delhi, India, 2022.
121. Bhojak, V.; Bhatia, D.; Jain, P.K. Investigation of photocurrent efficiency of Cs₂TiBr₆ double perovskite solar cell. *Mater. Today Proc.* **2022**, *66*, 3692–3697. [[CrossRef](#)]
122. Asghar, M.I.; Zhang, J.; Wang, H.; Lund, P.D. Device stability of perovskite solar cells—A review. *Renew. Sustain. Energy Rev.* **2017**, *77*, 131–146. [[CrossRef](#)]
123. Wang, D.; Wright, M.; Elumalai, N.K.; Uddin, A. Stability of perovskite solar cells. *Sol. Energy Mater. Sol. Cells* **2016**, *147*, 255–275. [[CrossRef](#)]
124. Noh, J.H.; Im, S.H.; Heo, J.H.; Mandal, T.N.; Seok, S.I. Chemical management for colorful, efficient, and stable inorganic–organic hybrid nanostructured solar cells. *Nano Lett.* **2013**, *13*, 1764–1769. [[CrossRef](#)]
125. Yuan, Y.; Xu, R.; Xu, H.T.; Hong, F.; Xu, F.; Wang, L.J. Nature of the band gap of halide perovskites ABX₃ (A = CH₃NH₃⁺, Cs; B = Sn, Pb; X = Cl, Br, I): First-principles calculations. *Chin. Phys. B* **2015**, *24*, 116302. [[CrossRef](#)]
126. Tsai, H.; Nie, W.; Blancon, J.C.; Stoumpos, C.C.; Asadpour, R.; Harutyunyan, B.; Mohite, A.D. High-efficiency two-dimensional Ruddlesden–Popper perovskite solar cells. *Nature* **2016**, *536*, 312–316. [[CrossRef](#)] [[PubMed](#)]
127. Yoo, J.J.; Seo, G.; Chua, M.R.; Park, T.G.; Lu, Y.; Rotermund, F.; Seo, J. Efficient perovskite solar cells via improved carrier management. *Nature* **2021**, *590*, 587–593. [[CrossRef](#)] [[PubMed](#)]
128. Jiang, Q.; Chu, Z.; Wang, P.; Yang, X.; Liu, H.; Wang, Y.; You, J. Planar-structure perovskite solar cells with efficiency beyond 21%. *Adv. Mater.* **2017**, *29*, 1703852. [[CrossRef](#)] [[PubMed](#)]
129. Chen, W.; Li, X.; Li, Y.; Li, Y. A review: Crystal growth for high-performance all-inorganic perovskite solar cells. *Energy Environ. Sci.* **2020**, *13*, 1971–1996. [[CrossRef](#)]
130. Yang, Y.; Peng, H.; Liu, C.; Arain, Z.; Ding, Y.; Ma, S.; Dai, S. Bi-functional additive engineering for high-performance perovskite solar cells with reduced trap density. *J. Mater. Chem. A* **2019**, *7*, 6450–6458. [[CrossRef](#)]
131. Wang, S.; Li, Z.; Zhang, Y.; Liu, X.; Han, J.; Li, X.; Choy, W.C. Water-soluble triazolium ionic-liquid-induced surface self-assembly to enhance the stability and efficiency of perovskite solar cells. *Adv. Funct. Mater.* **2019**, *29*, 1900417. [[CrossRef](#)]
132. Kumar, S.; Choi, Y.; Kang, S.H.; Oh, N.K.; Lee, J.; Seo, J.; Park, H. Multifaceted role of a dibutylhydroxytoluene processing additive in enhancing the efficiency and stability of planar perovskite solar cells. *ACS Appl. Mater. Interfaces* **2019**, *11*, 38828–38837. [[CrossRef](#)]
133. Liu, X.; Wu, J.; Guo, Q.; Yang, Y.; Luo, H.; Liu, Q.; Lan, Z. Pyrrole: An additive for improving the efficiency and stability of perovskite solar cells. *J. Mater. Chem. A* **2019**, *7*, 11764–11770. [[CrossRef](#)]
134. Li, T.; Wang, S.; Yang, J.; Pu, X.; Gao, B.; He, Z.; Li, X. Multiple functional groups synergistically improve the performance of inverted planar perovskite solar cells. *Nano Energy* **2021**, *82*, 105742. [[CrossRef](#)]
135. Zhang, X.; Wu, J.; Wang, S.; Pan, W.; Zhang, M.; Wang, X.; Lin, J. Additive Engineering by 6-Aminoquinoline Monohydrochloride for High-Performance Perovskite Solar Cells. *ACS Appl. Energy Mater.* **2021**, *4*, 7083–7090. [[CrossRef](#)]
136. Xu, T.; Wan, Z.; Tang, H.; Zhao, C.; Lv, S.; Chen, Y.; Huang, W. Carbon quantum dot additive engineering for efficient and stable carbon-based perovskite solar cells. *J. Alloys Compd.* **2021**, *859*, 157784. [[CrossRef](#)]
137. Chang, X.; Fang, J.; Fan, Y.; Luo, T.; Su, H.; Zhang, Y.; Zhao, K. Printable CsPbI₃ perovskite solar cells with PCE of 19% via an additive strategy. *Adv. Mater.* **2020**, *32*, 2001243. [[CrossRef](#)] [[PubMed](#)]
138. Fu, S.; Wang, J.; Liu, X.; Yuan, H.; Xu, Z.; Long, Y.; Zhu, Y. Multifunctional liquid additive strategy for highly efficient and stable CsPbI₂Br all-inorganic perovskite solar cells. *Chem. Eng. J.* **2021**, *422*, 130572. [[CrossRef](#)]
139. Ahmed, D.S.; Mohammed, M.K. Novel mixed solution of ethanol/MACl for improving the crystallinity of air-processed triple cation perovskite solar cells. *Sol. Energy* **2020**, *207*, 1240–1246. [[CrossRef](#)]
140. Akin, S.; Arora, N.; Zakeeruddin, S.M.; Graetzel, M.; Friend, R.H.; Dar, M.I. New strategies for defect passivation in high-efficiency perovskite solar cells. *Adv. Energy Mater.* **2020**, *10*, 1903090. [[CrossRef](#)]
141. Le Corre, V.M.; Stolterfoht, M.; Perdigon Toro, L.; Feuerstein, M.; Wolff, C.; Gil-Escrig, L.; Koster, L.J.A. Charge transport layers limiting the efficiency of perovskite solar cells: How to optimize conductivity, doping, and thickness. *ACS Appl. Energy Mater.* **2019**, *2*, 6280–6287. [[CrossRef](#)]
142. Madhavan, V.E.; Zimmermann, I.; Baloch, A.A.; Manekkathodi, A.; Belaidi, A.; Tabet, N.; Nazeeruddin, M.K. CuSCN as hole transport material with 3D/2D perovskite solar cells. *ACS Appl. Energy Mater.* **2019**, *3*, 114–121. [[CrossRef](#)]
143. Han, F.; Wu, Y.; He, R.; Hui, Y.; Yin, J.; Zheng, L.; Zheng, N. Hyperstable Perovskite Solar Cells Without Ion Migration and Metal Diffusion Based on ZnS Segregated Cubic ZnTiO₃ Electron Transport Layers. *Sol. RRL* **2021**, *5*, 2000654. [[CrossRef](#)]
144. Wang, Y.; Chen, W.; Wang, L.; Tu, B.; Chen, T.; Liu, B.; Guo, X. Dopant-free small-molecule hole-transporting material for inverted perovskite solar cells with efficiency exceeding 21%. *Adv. Mater.* **2019**, *31*, 1902781. [[CrossRef](#)]

145. Pham, H.D.; Jain, S.M.; Li, M.; Wang, Z.K.; Manzhos, S.; Feron, K.; Sonar, P. All-rounder low-cost dopant-free D-A-D hole-transporting materials for efficient indoor and outdoor performance of perovskite solar cells. *Adv. Electron. Mater.* **2020**, *6*, 1900884. [[CrossRef](#)]
146. Zhao, F.; Guo, Y.; Wang, X.; Tao, J.; Jiang, J.; Hu, Z.; Chu, J. Enhanced performance of carbon-based planar CsPbBr₃ perovskite solar cells with room-temperature sputtered Nb₂O₅ electron transport layer. *Sol. Energy* **2019**, *191*, 263–271. [[CrossRef](#)]
147. Kim, J.; Lee, Y.; Gil, B.; Yun, A.J.; Kim, J.; Woo, H.; Park, B. A Cu₂O–CuSCN nanocomposite as a hole-transport material of perovskite solar cells for enhanced carrier transport and suppressed interfacial degradation. *ACS Appl. Energy Mater.* **2020**, *3*, 7572–7579. [[CrossRef](#)]
148. Luo, X.; Ding, J.; Wang, J.; Zhang, J. Electron transport enhancement in perovskite solar cell via the polarized BaTiO₃ thin film. *J. Mater. Res.* **2020**, *35*, 2158–2165. [[CrossRef](#)]
149. Liu, X.; Ma, S.; Mateen, M.; Shi, P.; Liu, C.; Ding, Y.; Dai, S. Molecular engineering of simple carbazole-arylamine hole-transport materials for perovskite solar cells. *Sustain. Energy Fuels* **2020**, *4*, 1875–1882. [[CrossRef](#)]
150. Li, C.; Hu, Q.; Chen, Q.; Yu, W.; Xu, J.; Xu, Z.X. Tetrapropyl-substituted palladium phthalocyanine used as an efficient hole transport material in perovskite solar cells. *Org. Electron.* **2021**, *88*, 106018. [[CrossRef](#)]
151. Zhao, R.; Wang, L.; Huang, J.; Miao, X.; Sun, L.; Hua, Y.; Wang, Y. Amino-capped zinc oxide modified tin oxide electron transport layer for efficient perovskite solar cells. *Cell Rep. Phys. Sci.* **2021**, *2*, 100590. [[CrossRef](#)]
152. Yang, B.; Wang, M.; Hu, X.; Zhou, T.; Zang, Z. Highly efficient semitransparent CsPbI₂Br₂ perovskite solar cells via low-temperature processed In₂S₃ as electron-transport-layer. *Nano Energy* **2019**, *57*, 718–727. [[CrossRef](#)]
153. Kang, D.H.; Park, N.G. On the current–voltage hysteresis in perovskite solar cells: Dependence on perovskite composition and methods to remove hysteresis. *Adv. Mater.* **2019**, *31*, 1805214. [[CrossRef](#)]
154. Fakharuddin, A.; Schmidt-Mende, L.; Garcia-Belmonte, G.; Jose, R.; Mora-Sero, I. Interfaces in perovskite solar cells. *Adv. Energy Mater.* **2017**, *7*, 1700623. [[CrossRef](#)]
155. Zhang, F.; Lu, H.; Larson, B.W.; Xiao, C.; Dunfield, S.P.; Reid, O.G.; Zhu, K. Surface lattice engineering through three-dimensional lead iodide perovskitoid for high-performance perovskite solar cells. *Chem* **2021**, *7*, 774–785. [[CrossRef](#)]
156. Bu, T.; Li, J.; Huang, W.; Mao, W.; Zheng, F.; Bi, P.; Huang, F. Surface modification via self-assembling large cations for improved performance and modulated hysteresis of perovskite solar cells. *J. Mater. Chem. A* **2019**, *7*, 6793–6800. [[CrossRef](#)]
157. Liu, D.; Zheng, H.; Ji, L.; Chen, H.; Wang, Y.; Zhang, P.; Li, S. Improved crystallinity of perovskite via molecularly tailored surface modification of SnO₂. *J. Power Sources* **2019**, *441*, 227161. [[CrossRef](#)]
158. Lian, X.; Chen, J.; Shan, S.; Wu, G.; Chen, H. Polymer Modification on the NiO x Hole Transport Layer Boosts Open-Circuit Voltage to 1.19 V for Perovskite Solar Cells. *ACS Appl. Mater. Interfaces* **2020**, *12*, 46340–46347. [[CrossRef](#)] [[PubMed](#)]
159. Shu, H.; Xia, J.; Yang, H.; Luo, J.; Wan, Z.; Malik, H.A.; Jia, C. Self-assembled hydrophobic molecule-based surface modification: A strategy to improve efficiency and stability of perovskite solar cells. *ACS Sustain. Chem. Eng.* **2020**, *8*, 10859–10869. [[CrossRef](#)]
160. Zhu, X.; Cheng, B.; Li, X.; Zhang, J.; Zhang, L. Enhanced efficiency of perovskite solar cells by PbS quantum dot modification. *Appl. Surf. Sci.* **2019**, *487*, 32–40. [[CrossRef](#)]
161. Wang, G.; Wang, C.; Gao, Y.; Wen, S.; MacKenzie, R.C.; Guo, L.; Ruan, S. Passivation agent with dipole moment for surface modification towards efficient and stable perovskite solar cells. *J. Energy Chem.* **2022**, *64*, 55–61. [[CrossRef](#)]
162. Chen, R.; Long, B.; Wang, S.; Liu, Y.; Bai, J.; Huang, S.; Chen, X. Efficient and Stable Perovskite Solar Cells Using Bathocuproine Bilateral-Modified Perovskite Layers. *ACS Appl. Mater. Interfaces* **2021**, *13*, 24747–24755. [[CrossRef](#)]
163. Seo, J.; Park, S.; Kim, Y.C.; Jeon, N.J.; Noh, J.H.; Yoon, S.C.; Seok, S.I. Benefits of very thin PCBM and LiF layers for solution-processed p–i–n perovskite solar cells. *Energy Environ. Sci.* **2014**, *7*, 2642–2646. [[CrossRef](#)]
164. Jeng, J.Y.; Chiang, Y.F.; Lee, M.H.; Peng, S.R.; Guo, T.F.; Chen, P.; Wen, T.C. CH₃NH₃PbI₃ perovskite/fullerene planar-heterojunction hybrid solar cells. *Adv. Mater.* **2013**, *25*, 3727–3732. [[CrossRef](#)]
165. Zuo, L.; Gu, Z.; Ye, T.; Fu, W.; Wu, G.; Li, H.; Chen, H. Enhanced photovoltaic performance of CH₃NH₃PbI₃ perovskite solar cells through interfacial engineering using self-assembling monolayer. *J. Am. Chem. Soc.* **2015**, *137*, 2674–2679. [[CrossRef](#)]
166. Eperon, G.E.; Burlakov, V.M.; Docampo, P.; Goriely, A.; Snaith, H.J. Morphological control for high performance, solution-processed planar heterojunction perovskite solar cells. *Adv. Funct. Mater.* **2014**, *24*, 151–157. [[CrossRef](#)]
167. Huang, J.; Gu, Z.; Zuo, L.; Ye, T.; Chen, H. Morphology control of planar heterojunction perovskite solar cells with fluorinated PDI films as organic electron transport layer. *Sol. Energy* **2016**, *133*, 331–338. [[CrossRef](#)]
168. Jeon, Y.-J.; Lee, S.; Kang, R.; Kim, J.-E.; Yeo, J.-S.; Lee, S.-H.; Kim, S.-S.; Yun, J.-M.; Kim, D.-Y. Planar heterojunction perovskite solar cells with superior reproducibility. *Sci. Rep.* **2014**, *4*, 6953. [[CrossRef](#)]
169. Ergen, O.; Gilbert, S.M.; Pham, T.; Turner, S.J.; Tan, M.T.Z.; Worsley, M.A.; Zettl, A. Graded bandgap perovskite solar cells. *Nat. Mater.* **2017**, *16*, 522–525. [[CrossRef](#)]
170. Tang, H.; He, S.; Peng, C. A short progress report on high-efficiency perovskite solar cells. *Nanoscale Res. Lett.* **2017**, *12*, 1–8. [[CrossRef](#)]
171. Malinkiewicz, O.; Yella, A.; Lee, Y.H.; Espallargas, G.M.; Graetzel, M.; Nazeeruddin, M.K.; Bolink, H.J. Perovskite solar cells employing organic charge-transport layers. *Nat. Photonics* **2014**, *8*, 128–132. [[CrossRef](#)]
172. Larson, R.G.; Rehg, T.J. Spin coating. In *Liquid Film Coating: Scientific Principles and Their Technological Implications*; Springer: Berlin/Heidelberg, Germany, 1997; pp. 709–734.

173. Tzounis, L.; Stergiopoulos, T.; Zachariadis, A.; Gravalidis, C.; Laskarakis, A.; Logothetidis, S. Perovskite solar cells from small scale spin coating process towards roll-to-roll printing: Optical and morphological studies. *Mater. Today Proc.* **2017**, *4*, 5082–5089. [[CrossRef](#)]
174. Shalan, A.E. Challenges and approaches towards upscaling the assembly of hybrid perovskite solar cells. *Mater. Adv.* **2020**, *1*, 292–309. [[CrossRef](#)]
175. Mathies, F.; Abzieher, T.; Hochstuhl, A.; Glaser, K.; Colsmann, A.; Paetzold, U.W.; Quintilla, A. Multipass inkjet printed planar methylammonium lead iodide perovskite solar cells. *J. Mater. Chem. A* **2016**, *4*, 19207–19213. [[CrossRef](#)]
176. Liang, C.; Li, P.; Gu, H.; Zhang, Y.; Li, F.; Song, Y.; Shao, G.; Mathews, N.; Xing, G. One-step inkjet printed perovskite in air for efficient light harvesting. *Sol. RRL* **2018**, *2*, 1700217. [[CrossRef](#)]
177. Li, P.; Liang, C.; Bao, B.; Li, Y.; Hu, X.; Wang, Y.; Song, Y. Inkjet manipulated homogeneous large size perovskite grains for efficient and large-area perovskite solar cells. *Nano Energy* **2018**, *46*, 203–211. [[CrossRef](#)]
178. Zhao, Y.; Ma, F.; Gao, F.; Yin, Z.; Zhang, X.; You, J. Research progress in large-area perovskite solar cells. *Photonics Res.* **2020**, *8*, A1–A15. [[CrossRef](#)]
179. Tait, J.G.; Manghooli, S.; Qiu, W.; Rakocevic, L.; Kootstra, L.; Jaysankar, M.; Poortmans, J. Rapid composition screening for perovskite photovoltaics via concurrently pumped ultrasonic spray coating. *J. Mater. Chem. A* **2016**, *4*, 3792–3797. [[CrossRef](#)]
180. Ye, F.; Chen, H.; Xie, F.; Tang, W.; Yin, M.; He, J.; Han, L. Soft-cover deposition of scaling-up uniform perovskite thin films for high cost-performance solar cells. *Energy Environ. Sci.* **2016**, *9*, 2295–2301. [[CrossRef](#)]
181. Wu, Y.; Yang, X.; Chen, W.; Yue, Y.; Cai, M.; Xie, F.; Han, L. Perovskite solar cells with 18.21% efficiency and area over 1 cm² fabricated by heterojunction engineering. *Nat. Energy* **2016**, *1*, 16148. [[CrossRef](#)]
182. Wu, Y.; Xie, F.; Chen, H.; Yang, X.; Su, H.; Cai, M.; Han, L. Thermally stable MAPbI₃ perovskite solar cells with efficiency of 19.19% and area over 1 cm² achieved by additive engineering. *Adv. Mater.* **2017**, *29*, 1701073. [[CrossRef](#)] [[PubMed](#)]
183. Di Giacomo, F.; Fakharuddin, A.; Jose, R.; Brown, T.M. Progress, challenges and perspectives in flexible perovskite solar cells. *Energy Environ. Sci.* **2016**, *9*, 3007–3035. [[CrossRef](#)]
184. Cao, K.; Zuo, Z.; Cui, J.; Shen, Y.; Moehl, T.; Zakeeruddin, S.M.; Wang, M. Efficient screen printed perovskite solar cells based on mesoscopic TiO₂/Al₂O₃/NiO/carbon architecture. *Nano Energy* **2015**, *17*, 171–179. [[CrossRef](#)]
185. Li, X.; Yang, J.; Jiang, Q.; Chu, W.; Zhang, D.; Zhou, Z.; Xin, J. Synergistic effect to high-performance perovskite solar cells with reduced hysteresis and improved stability by the introduction of Na-treated TiO₂ and spraying-deposited CuI as transport layers. *ACS Appl. Mater. Interfaces* **2017**, *9*, 41354–41362. [[CrossRef](#)]
186. Deng, Y.; Zheng, X.; Bai, Y.; Wang, Q.; Zhao, J.; Huang, J. Surfactant-controlled ink drying enables high-speed deposition of perovskite films for efficient photovoltaic modules. *Nat. Energy* **2018**, *3*, 560–566. [[CrossRef](#)]
187. Deng, Y.; Wang, Q.; Yuan, Y.; Huang, J. Vividly colorful hybrid perovskite solar cells by doctor-blade coating with perovskite photonic nanostructures. *Mater. Horiz.* **2015**, *2*, 578–583. [[CrossRef](#)]
188. Wu, W.Q.; Yang, Z.; Rudd, P.N.; Shao, Y.; Dai, X.; Wei, H.; Huang, J. Bilateral alkylamine for suppressing charge recombination and improving stability in blade-coated perovskite solar cells. *Sci. Adv.* **2019**, *5*, eaav8925. [[CrossRef](#)]
189. Zhong, Y.; Munir, R.; Li, J.; Tang, M.C.; Niazi, M.R.; Smilgies, D.M.; Amassian, A. Blade-coated hybrid perovskite solar cells with efficiency > 17%: An in situ investigation. *ACS Energy Lett.* **2018**, *3*, 1078–1085. [[CrossRef](#)]
190. Lin, Y.; Ye, X.; Wu, Z.; Zhang, C.; Zhang, Y.; Su, H.; Li, J. Manipulation of the crystallization of perovskite films induced by a rotating magnetic field during blade coating in air. *J. Mater. Chem. A* **2018**, *6*, 3986–3995. [[CrossRef](#)]
191. Li, J.; Munir, R.; Fan, Y.; Niu, T.; Liu, Y.; Zhong, Y.; Liu, S.F. Phase transition control for high-performance blade-coated perovskite solar cells. *Joule* **2018**, *2*, 1313–1330. [[CrossRef](#)]
192. Razza, S.; Di Giacomo, F.; Matteocci, F.; Cina, L.; Palma, A.L.; Casaluci, S.; Di Carlo, A. Perovskite solar cells and large area modules (100 cm²) based on an air flow-assisted PbI₂ blade coating deposition process. *J. Power Sources* **2015**, *277*, 286–291. [[CrossRef](#)]
193. Deng, Y.; Van Brackle, C.H.; Dai, X.; Zhao, J.; Chen, B.; Huang, J. Tailoring solvent coordination for high-speed, room-temperature blading of perovskite photovoltaic films. *Sci. Adv.* **2019**, *5*, eaax7537. [[CrossRef](#)] [[PubMed](#)]
194. Zhang, J.; Bu, T.; Li, J.; Li, H.; Mo, Y.; Wu, Z.; Huang, F. Two-step sequential blade-coating of high quality perovskite layers for efficient solar cells and modules. *J. Mater. Chem. A* **2020**, *8*, 8447–8454. [[CrossRef](#)]
195. Ding, X.; Liu, J.; Harris, T.A. A review of the operating limits in slot die coating processes. *AIChE J.* **2016**, *62*, 2508–2524. [[CrossRef](#)]
196. Whitaker, J.B.; Kim, D.H.; Larson, B.W.; Zhang, F.; Berry, J.J.; van Hest, M.F.; Zhu, K. Scalable slot-die coating of high performance perovskite solar cells. *Sustain. Energy Fuels* **2018**, *2*, 2442–2449. [[CrossRef](#)]
197. Zuo, C.; Vak, D.; Angmo, D.; Ding, L.; Gao, M. One-step roll-to-roll air processed high efficiency perovskite solar cells. *Nano Energy* **2018**, *46*, 185–192. [[CrossRef](#)]
198. Chauhan, J.; Mehto, V.R.; Mehto, A.; Thakur, P. Structural and Optical Study of CdSe Q-dots. *Int. J. Nanomater. Nanostruct.* **2021**, *8*, 25–30.
199. Meng, H.; Zhang, F.; Mo, C.; Xia, Q.; Zhong, M.; Jun, H. Energy transfer in hybrid 0D-CdSe quantum dot/2D-WSe₂ near-infrared photodetectors. *J. Phys. D Appl. Phys.* **2022**, *55*, 444006. [[CrossRef](#)]
200. Markna, J.H.; Rathod, P.K. Review on the efficiency of quantum dot sensitized solar cell: Insights into photoanodes and QD sensitizers. *Dye. Pigment.* **2022**, *199*, 110094. [[CrossRef](#)]

201. Ba, K.; Wang, J. Advances in solution-processed quantum dots based hybrid structures for infrared photodetector. *Mater. Today* **2022**, *58*, 119–134. [[CrossRef](#)]
202. Maiti, S.; Dana, J.; Ghosh, H.N. Correlating Charge-Carrier Dynamics with Efficiency in Quantum-Dot Solar Cells: Can Excitonicity Lead to Highly Efficient Devices? *Chem.—A Eur. J.* **2019**, *25*, 692–702. [[CrossRef](#)] [[PubMed](#)]
203. Fu, S.; du Fossé, I.; Jia, X.; Xu, J.; Yu, X.; Zhang, H.; Wang, H.I. Long-lived charge separation following pump-wavelength-dependent ultrafast charge transfer in graphene/WS₂ heterostructures. *Sci. Adv.* **2021**, *7*, eabd9061. [[CrossRef](#)] [[PubMed](#)]
204. Luther, J.M.; Gao, J.; Lloyd, M.T.; Semonin, O.E.; Beard, M.C.; Nozik, A.J. Stability assessment on a 3% bilayer PbS/ZnO quantum dot heterojunction solar cell. *Adv. Mater.* **2010**, *22*, 3704–3707. [[CrossRef](#)] [[PubMed](#)]
205. Hao, M.; Bai, Y.; Zeiske, S.; Ren, L.; Liu, J.; Yuan, Y.; Wang, L. Ligand-assisted cation-exchange engineering for high-efficiency colloidal Cs_{1-x}FA_xPbI₃ quantum dot solar cells with reduced phase segregation. *Nat. Energy* **2020**, *5*, 79–88. [[CrossRef](#)]
206. Rühle, S. Tabulated values of the Shockley–Queisser limit for single junction solar cells. *Sol. Energy* **2016**, *130*, 139–147. [[CrossRef](#)]
207. Sahu, A.; Ashish, G.; Ambesh, D. A review on quantum dot sensitized solar cells: Past, present and future towards carrier multiplication with a possibility for higher efficiency. *Sol. Energy* **2022**, *203*, 210–239. [[CrossRef](#)]
208. Basit, M.A.; Abbas, M.A.; Jung, E.S.; Bang, J.H.; Park, T.J. Improved light absorbance and quantum-dot loading by macroporous TiO₂ photoanode for PbS quantum-dot-sensitized solar cells. *Mater. Chem. Phys.* **2017**, *196*, 170–176. [[CrossRef](#)]
209. Dong, L.; Wang, S.; Chen, L.; Jin, X. CdS QD-CQD co-sensitized TiO₂ solar cells: Preparation and photoelectrochemical properties. *Mater. Technol.* **2019**, *34*, 59–67. [[CrossRef](#)]
210. Venkatachalam, P.; Rajalakshmi, S. Performance of perovskite and quantum dot sensitized solar cell based on ZnO photoanode structure. *Mater. Today Proc.* **2020**, *22*, 400–403. [[CrossRef](#)]
211. Zhou, X.; Fu, W.; Yang, H.; Li, Y.; Chen, Y.; Sun, M.; Tian, L. CdS quantum dots sensitized SnO₂ photoelectrode for photoelectrochemical application. *Electrochim. Acta* **2013**, *89*, 510–515. [[CrossRef](#)]
212. Park, J.; Sajjad, M.T.; Jouneau, P.H.; Ruseckas, A.; Faure-Vincent, J.; Samuel, I.D.; Aldakov, D. Efficient eco-friendly inverted quantum dot sensitized solar cells. *J. Mater. Chem. A* **2016**, *4*, 827–837. [[CrossRef](#)]
213. Chaudhari, N.; Darvekar, S.; Nasikkar, P.; Kulkarni, A.; Tagad, C. Recent developments on green synthesised nanomaterials and their application in dye-sensitized solar cells. *Int. J. Ambient. Energy* **2022**, *43*, 7133–7149. [[CrossRef](#)]
214. Chen, S.; Wang, Y.; Wu, C.; Li, R.; Lin, J.; Liu, Y.; Zhang, X. Noncorrosive necking treatment of the mesoporous BaSnO₃ photoanode for quantum dot-sensitized solar cells. *Sol. Energy* **2020**, *208*, 527–531. [[CrossRef](#)]
215. Mathpal, M.C.; Kumar, P.; Aragón, F.H.; Soler, M.A.; Swart, H.C. Basic concepts, engineering, and advances in dye-sensitized solar cells. In *Solar Cells*; Springer: Cham, Switzerland, 2020; pp. 185–233.
216. Archana, T.; Vijayakumar, K.; Arivanandhan, M.; Jayavel, R. TiO₂ nanostructures with controlled morphology for improved electrical properties of photoanodes and quantum dot sensitized solar cell characteristics. *Surf. Interfaces* **2019**, *17*, 100350. [[CrossRef](#)]
217. Maiti, S.; Azlan, F.; Jadhav, Y.; Dana, J.; Anand, P.; Haram, S.K.; Ghosh, H.N. Efficient charge transport in surface engineered TiO₂ nanoparticulate photoanodes leading to improved performance in quantum dot sensitized solar cells. *Sol. Energy* **2019**, *181*, 195–202. [[CrossRef](#)]
218. Shen, G.; Du, Z.; Pan, Z.; Du, J.; Zhong, X. Solar paint from TiO₂ particles supported quantum dots for photoanodes in quantum dot-sensitized solar cells. *ACS Omega* **2018**, *3*, 1102–1109. [[CrossRef](#)]
219. Huang, X.; Huang, S.; Zhang, Q.; Guo, X.; Li, D.; Luo, Y.; Meng, Q. A flexible photoelectrode for CdS/CdSe quantum dot-sensitized solar cells (QDSSCs). *Chem. Commun.* **2011**, *47*, 2664–2666. [[CrossRef](#)]
220. Gao, Q.; Wang, L.; Zhang, X.; Duan, L.; Li, X.; Yang, X.; Lü, W. Carbon nanoparticle template assisted formation of mesoporous TiO₂ photoanodes for quantum dot-sensitized solar cells. *New J. Chem.* **2019**, *43*, 5374–5381. [[CrossRef](#)]
221. Zhu, G.; Pan, L.; Xu, T.; Sun, Z. CdS/CdSe-cosensitized TiO₂ photoanode for quantum-dot-sensitized solar cells by a microwave-assisted chemical bath deposition method. *ACS Appl. Mater. Interfaces* **2011**, *3*, 3146–3151. [[CrossRef](#)]
222. Sanehira, E.M.; Marshall, A.R.; Christians, J.A.; Harvey, S.P.; Ciesielski, P.N.; Wheeler, L.M.; Luther, J.M. Enhanced mobility CsPbI₃ quantum dot arrays for record-efficiency, high-voltage photovoltaic cells. *Sci. Adv.* **2017**, *3*, eaao4204. [[CrossRef](#)] [[PubMed](#)]
223. Gao, J.; Perkins, C.L.; Luther, J.M.; Hanna, M.C.; Chen, H.Y.; Semonin, O.E.; Beard, M.C. n-Type transition metal oxide as a hole extraction layer in PbS quantum dot solar cells. *Nano Lett.* **2011**, *11*, 3263–3266. [[CrossRef](#)]
224. Zhang, J.; Gao, J.; Church, C.P.; Miller, E.M.; Luther, J.M.; Klimov, V.I.; Beard, M.C. PbSe quantum dot solar cells with more than 6% efficiency fabricated in ambient atmosphere. *Nano Lett.* **2014**, *14*, 6010–6015. [[CrossRef](#)]
225. Kim, S.; Marshall, A.R.; Kroupa, D.M.; Miller, E.M.; Luther, J.M.; Jeong, S.; Beard, M.C. Air-stable and efficient PbSe quantum-dot solar cells based upon ZnSe to PbSe cation-exchanged quantum dots. *ACS Nano* **2015**, *9*, 8157–8164. [[CrossRef](#)]
226. Santra, P.K.; Kamat, P.V. Mn-doped quantum dot sensitized solar cells: A strategy to boost efficiency over 5%. *J. Am. Chem. Soc.* **2012**, *134*, 2508–2511. [[CrossRef](#)]
227. Zhu, G.; Xu, T.; Lv, T.; Pan, L.; Zhao, Q.; Sun, Z. Graphene-incorporated nanocrystalline TiO₂ films for CdS quantum dot-sensitized solar cells. *J. Electroanal. Chem.* **2011**, *650*, 248–251. [[CrossRef](#)]
228. Singh, N.; Salam, Z.; Subasri, A.; Sivasankar, N.; Subramania, A. Development of porous TiO₂ nanofibers by solvasonication process for high performance quantum dot sensitized solar cell. *Sol. Energy Mater. Sol. Cells* **2018**, *179*, 417–426. [[CrossRef](#)]
229. Singh, N.; Murugadoss, V.; Nemala, S.; Mallick, S.; Angaiah, S. Cu₂ZnSnSe₄ QDs sensitized electrospun porous TiO₂ nanofibers as photoanode for high performance QDSC. *Sol. Energy* **2018**, *171*, 571–579. [[CrossRef](#)]

230. Singh, N.; Murugadoss, V.; Rajavedhanayagam, J.; Angaiah, S. A wide solar spectrum light harvesting Ag₂Se quantum dot-sensitized porous TiO₂ nanofibers as photoanode for high-performance QDSC. *J. Nanopart. Res.* **2019**, *21*, 176. [CrossRef]
231. Ren, Z.; Wang, J.; Pan, Z.; Zhao, K.; Zhang, H.; Li, Y.; Zhong, X. Amorphous TiO₂ buffer layer boosts efficiency of quantum dot sensitized solar cells to over 9%. *Chem. Mater.* **2015**, *27*, 8398–8405. [CrossRef]
232. Zhou, C.; Wang, H.; Huang, T.; Zhang, X.; Shi, Z.; Zhou, L.; Tang, G. High-performance TiO₂/ZnO photoanodes for CdS quantum dot-sensitized solar cells. *J. Electron. Mater.* **2019**, *48*, 7320–7327. [CrossRef]
233. Li, L.; Yang, X.; Zhang, W.; Zhang, H.; Li, X. Boron and sulfur co-doped TiO₂ nanofilm as effective photoanode for high efficiency CdS quantum-dot-sensitized solar cells. *J. Power Sources* **2014**, *272*, 508–512. [CrossRef]
234. Du, Z.; Zhang, H.; Bao, H.; Zhong, X. Optimization of TiO₂ photoanode films for highly efficient quantum dot-sensitized solar cells. *J. Mater. Chem. A* **2014**, *2*, 13033–13040. [CrossRef]
235. Kumar, P.N.; Das, A.; Deepa, M. Nitrogen doping of TiO₂ and annealing treatment of photoanode for enhanced solar cell performance. *J. Alloys Compd.* **2020**, *832*, 154880. [CrossRef]
236. Kottayi, R.; Panneerselvam, P.; Murugadoss, V.; Sittaramane, R.; Angaiah, S. Cu₂AgInSe₄ QDs sensitized electrospun porous TiO₂ nanofibers as an efficient photoanode for quantum dot sensitized solar cells. *Sol. Energy* **2020**, *199*, 317–325. [CrossRef]
237. Meng, K.; Surolia, P.K.; Thampi, K.R. BaTiO₃ photoelectrodes for CdS quantum dot sensitized solar cells. *J. Mater. Chem. A* **2014**, *2*, 10231–10238. [CrossRef]
238. Lan, Z.; Liu, L.; Huang, M.; Wu, J.; Lin, J. Preparation of nano-flower-like SnO₂ particles and their applications in efficient CdS quantum dots sensitized solar cells. *J. Mater. Sci. Mater. Electron.* **2015**, *26*, 7914–7920. [CrossRef]
239. Huang, Q.; Li, F.; Gong, Y.; Luo, J.; Yang, S.; Luo, Y.; Meng, Q. Recombination in SnO₂-based quantum dots sensitized solar cells: The role of surface states. *J. Phys. Chem. C* **2013**, *117*, 10965–10973. [CrossRef]
240. Alvarado, J.A.; Luo, J.; Juarez, H.; Pacio, M.; Cortes-Santiago, A.; Liang, L.; Cao, G. Vacuum-Evaporated ZnO Photoanode, Applied in Quantum Dot-Sensitized Solar Cells (CdS-CdSe). *Phys. Status Solidi* **2018**, *215*, 1800356. [CrossRef]
241. Li, C.; Yang, L.; Xiao, J.; Wu, Y.C.; Søndergaard, M.; Luo, Y.; Iversen, B.B. ZnO nanoparticle based highly efficient CdS/CdSe quantum dot-sensitized solar cells. *Phys. Chem. Chem. Phys.* **2013**, *15*, 8710–8715. [CrossRef]
242. Chuang CH, M.; Brown, P.R.; Bulović, V.; Bawendi, M.G. Improved performance and stability in quantum dot solar cells through band alignment engineering. *Nat. Mater.* **2014**, *13*, 796–801. [CrossRef]
243. Tian, J.; Zhang, Q.; Uchaker, E.; Liang, Z.; Gao, R.; Qu, X.; Cao, G. Constructing ZnO nanorod array photoelectrodes for highly efficient quantum dot sensitized solar cells. *J. Mater. Chem. A* **2013**, *1*, 6770–6775. [CrossRef]
244. Lin, Y.; Lin, Y.; Wu, J.; Tu, Y.; Zhang, X.; Fang, B. Improved performance of quantum dots sensitized solar cells using ZnO hierarchical spheres as photoanodes. *Ceram. Int.* **2015**, *41*, 14501–14507. [CrossRef]
245. Tyagi, J.; Gupta, H.; Purohit, L.P. Cascade Structured ZnO/TiO₂/CdS quantum dot sensitized solar cell. *Solid State Sci.* **2020**, *102*, 106176. [CrossRef]
246. Khodam, F.; Amani-Ghadim, A.R.; Aber, S. Preparation of CdS quantum dot sensitized solar cell based on ZnTi-layered double hydroxide photoanode to enhance photovoltaic properties. *Sol. Energy* **2019**, *181*, 325–332. [CrossRef]
247. Yu, J.; Li, D.; Zhu, L.; Xu, X. Application of ZnTiO₃ in quantum-dot-sensitized solar cells and numerical simulations using first-principles theory. *J. Alloys Compd.* **2016**, *681*, 88–95. [CrossRef]
248. Sundheep, R.; Asok, A.; Prasanth, R. Surface engineering of CdTe quantum dots using ethanol as a co-solvent for enhanced current conversion efficiency in QDSSC. *Sol. Energy* **2019**, *180*, 501–509. [CrossRef]
249. Nozik, A.J. Quantum dot solar cells. *Phys. E Low-Dimens. Syst. Nanostruct.* **2002**, *14*, 115–120. [CrossRef]
250. Hu, L.; Geng, X.; Singh, S.; Shi, J.; Hu, Y.; Li, S.; Wu, T. Synergistic effect of electron transport layer and colloidal quantum dot solid enable PbSe quantum dot solar cell achieving over 10% efficiency. *Nano Energy* **2019**, *64*, 103922. [CrossRef]
251. Zaban AM, O.I.; Mičić, O.I.; Gregg, B.A.; Nozik, A.J. Photosensitization of nanoporous TiO₂ electrodes with InP quantum dots. *Langmuir* **1998**, *14*, 3153–3156. [CrossRef]
252. Saeed, S.; Iqbal, A.; Iqbal, A. Photoinduced charge carrier dynamics in a ZnSe quantum dot-attached CdTe system. *Proc. R. Soc. A* **2020**, *476*, 20190616. [CrossRef] [PubMed]
253. Samadpour, M.; Jun, H.K.; Parand, P.; Najafi, M.N. CdS quantum dots pre-deposition for efficiency enhancement of quantum dot-sensitized solar cells. *Sol. Energy* **2019**, *188*, 825–830. [CrossRef]
254. Blachowicz, T.; Ehrmann, A. Recent developments of solar cells from PbS colloidal quantum dots. *Appl. Sci.* **2020**, *10*, 1743. [CrossRef]
255. Xue, Y.; Yang, F.; Yuan, J.; Zhang, Y.; Gu, M.; Xu, Y.; Ma, W. Toward scalable PbS quantum dot solar cells using a tailored polymeric hole conductor. *ACS Energy Lett.* **2019**, *4*, 2850–2858. [CrossRef]
256. Badawi, A. Effect of the non-toxic Ag₂S quantum dots size on their optical properties for environment-friendly applications. *Phys. E Low-Dimens. Syst. Nanostruct.* **2019**, *109*, 107–113. [CrossRef]
257. Peter, I.J.; Dhinakaran, S.; Ramachandran, K.; Nithiananthi, P. Performance of TiO₂/CdS/Bi₂S₃ heterostructure based semiconductor sensitized solar cell. In *AIP Conference Proceedings*; AIP Publishing LLC.: Melville, NY, USA, 2019; Volume 2115, p. 030557.
258. Fu, B.; Deng, C.; Yang, L. Efficiency enhancement of solid-state CuInS₂ quantum dot-sensitized solar cells by improving the charge recombination. *Nanoscale Res. Lett.* **2019**, *14*, 198. [CrossRef]

259. Yu, P.; Zhu, K.; Norman, A.G.; Ferrere, S.; Frank, A.J.; Nozik, A.J. Nanocrystalline TiO₂ solar cells sensitized with InAs quantum dots. *J. Phys. Chem. B* **2006**, *110*, 25451–25454. [[CrossRef](#)]
260. Suriyawong, N.; Aragaw, B.; Shi, J.B.; Lee, M.W. Ternary CuBiS₂ nanoparticles as a sensitizer for quantum dot solar cells. *J. Colloid Interface Sci.* **2016**, *473*, 60–65. [[CrossRef](#)] [[PubMed](#)]
261. Lu, W.; Song, B.; Li, H.; Zhou, J.; Dong, W.; Zhao, G.; Han, G. Strategy for performance enhancement of Cd_{1-x}Zn_xTe/CdS core/shell quantum dot sensitized solar cells through band adjustment. *J. Alloys Compd.* **2020**, *826*, 154050. [[CrossRef](#)]
262. Mirahmadi, F.S.; Marandi, M.; Karimipour, M.; Molaei, M. Microwave activated synthesis of Ag₂S and Ag₂S@ZnS nanocrystals and their application in well-performing quantum dot sensitized solar cells. *Sol. Energy* **2020**, *202*, 155–163. [[CrossRef](#)]
263. Li, W.; Yang, J.; Jiang, Q.; Luo, Y.; Hou, Y.; Zhou, S.; Zhou, Z. Electrochemical atomic layer deposition of Bi₂S₃/Sb₂S₃ quantum dots co-sensitized TiO₂ nanorods solar cells. *J. Power Sources* **2016**, *307*, 690–696. [[CrossRef](#)]
264. Ca, N.X.; Hien, N.T.; Luyen, N.T.; Lien VT, K.; Thanh, L.D.; Do, P.V.; Pham, T.T. Photoluminescence properties of CdTe/CdTeSe/CdSe core/alloyed/shell type-II quantum dots. *J. Alloys Compd.* **2019**, *787*, 823–830. [[CrossRef](#)]
265. Zheng, X.; Das, S.; Gu, Y.; Liu, S.; Zhao, J. Optimal engineering of CdS/PbS co-sensitized TiO₂ nanotube arrays for enhanced photoelectrochemical performance. *Ceram. Int.* **2020**, *46*, 12050–12058. [[CrossRef](#)]
266. Liu, D.; Liu, J.; Liu, J.; Liu, S.; Wang, C.; Ge, Z.; Xiao, H. The photovoltaic performance of CdS/CdSe quantum dots co-sensitized solar cells based on zinc titanium mixed metal oxides. *Phys. E Low-Dimens. Syst. Nanostruct.* **2020**, *115*, 113669. [[CrossRef](#)]
267. Marandi, M.; Mirahmadi, F.S. Aqueous synthesis of the CdTe NCs and influence of size on photovoltaic performance of the CdS/CdTe co-sensitized solar cells. *J. Alloys Compd.* **2019**, *800*, 140–149. [[CrossRef](#)]
268. Zavaraki, A.J.; Liu, Q.; Ågren, H. Solar cell sensitized with “green” InP-ZnS quantum dots: Effect of ZnS shell deposition. *Nano-Struct. Nano-Objects* **2020**, *22*, 100461. [[CrossRef](#)]
269. Choi, Y.; Seol, M.; Kim, W.; Yong, K. Chemical bath deposition of stoichiometric CdSe quantum dots for efficient quantum-dot-sensitized solar cell application. *J. Phys. Chem. C* **2014**, *118*, 5664–5670. [[CrossRef](#)]
270. Becker, M.A.; Radich, E.J.; Bunker, B.A.; Kamat, P.V. How does a SILAR CdSe film grow? Tuning the deposition steps to suppress interfacial charge recombination in solar cells. *J. Phys. Chem. Lett.* **2014**, *5*, 1575–1582. [[CrossRef](#)]
271. Punnoose, D.; Suh, S.M.; Kim, B.J.; Kumar, C.S.P.; Rao, S.S.; Thulasi-Varma, C.V.; Kim, H.J. The influence of in situ deposition techniques on PbS seeded CdS/CdSe for enhancing the photovoltaic performance of quantum dot sensitized solar cells. *J. Electroanal. Chem.* **2016**, *773*, 27–38. [[CrossRef](#)]
272. Kyaw HM, A.; Noor AF, M.; Kawamura, G.; Matsuda, A.; Yaacob, K.A. Effect of CdSe thickness deposited by electrophoretic deposition for quantum-dot-sensitized solar cell. *Mater. Today Proc.* **2019**, *16*, 196–200. [[CrossRef](#)]
273. Salant, A.; Shalom, M.; Hod, I.; Faust, A.; Zaban, A.; Banin, U. Quantum dot sensitized solar cells with improved efficiency prepared using electrophoretic deposition. *ACS Nano* **2010**, *4*, 5962–5968. [[CrossRef](#)]
274. Wang, W.; Jiang, G.; Yu, J.; Wang, W.; Pan, Z.; Nakazawa, N.; Zhong, X. High efficiency quantum dot sensitized solar cells based on direct adsorption of quantum dots on photoanodes. *ACS Appl. Mater. Interfaces* **2017**, *9*, 22549–22559. [[CrossRef](#)] [[PubMed](#)]
275. Veerathangam, K.; Pandian, M.S.; Ramasamy, P. Incorporation of Co²⁺ in CdS quantum dots for solar cell applications. *Mater. Sci. Semicond. Process.* **2020**, *108*, 104869. [[CrossRef](#)]
276. Ganguly, A.; Nath, S.S. Mn-doped CdS quantum dots as sensitizers in solar cells. *Mater. Sci. Eng. B* **2020**, *255*, 114532. [[CrossRef](#)]
277. Dissanayake, M.A.K.L.; Jaseetharan, T.; Senadeera, G.K.R.; Thotawatthage, C.A. A novel, PbS: Hg quantum dot-sensitized, highly efficient solar cell structure with triple layered TiO₂ photoanode. *Electrochim. Acta* **2018**, *269*, 172–179. [[CrossRef](#)]
278. Tung, H.T.; Van Thuan, D.; Kiat, J.H.; Phuc, D.H. Ag⁺ ion doped on the CdSe quantum dots for quantum-dot-sensitized solar cells’ application. *Appl. Phys. A* **2019**, *125*, 505. [[CrossRef](#)]
279. Li, L.; Zou, X.; Zhou, H.; Teng, G. Cu-doped-CdS/In-doped-CdS cosensitized quantum dot solar cells. *J. Nanomater.* **2014**, *2014*, 314386. [[CrossRef](#)]
280. Lee, W.; Kwak, W.C.; Min, S.K.; Lee, J.C.; Chae, W.S.; Sung, Y.M.; Han, S.H. Spectral broadening in quantum dots-sensitized photoelectrochemical solar cells based on CdSe and Mg-doped CdSe nanocrystals. *Electrochem. Commun.* **2008**, *10*, 1699–1702. [[CrossRef](#)]
281. Marandi, M.; Torabi, N.; Farahani, F.A. Facile fabrication of well-performing CdS/CdSe quantum dot sensitized solar cells through a fast and effective formation of the CdSe nanocrystalline layer. *Sol. Energy* **2020**, *207*, 32–39. [[CrossRef](#)]
282. Deng, Y.; Lu, S.; Xu, Z.; Zhang, J.; Ma, F.; Peng, S. Enhanced performance of CdS/CdSe quantum dot-sensitized solar cells by long-persistence phosphors structural layer. *Sci. China Mater.* **2020**, *63*, 516–523. [[CrossRef](#)]
283. Hu, L.; Huang, S.; Patterson, R.; Halpert, J.E. Enhanced mobility in PbS quantum dot films via PbSe quantum dot mixing for optoelectronic applications. *J. Mater. Chem. C* **2019**, *7*, 4497–4502. [[CrossRef](#)]
284. Ma, C.; Shi, C.; Lv, K.; Ying, C.; Fan, S.; Yang, Y. Gradient-band-gap strategy for efficient solid-state PbS quantum-dot sensitized solar cells. *Nanoscale* **2019**, *11*, 8402–8407. [[CrossRef](#)]
285. Jun, H.K.; Careem, M.A.; Arof, A.K. Quantum dot-sensitized solar cells—Perspective and recent developments: A review of Cd chalcogenide quantum dots as sensitizers. *Renew. Sustain. Energy Rev.* **2013**, *22*, 148–167. [[CrossRef](#)]
286. Zhang, Q.; Jin, Z.; Li, F.; Xia, Z.; Yang, Y.; Xu, L. First application of CoO nanorods as efficient counter electrode for quantum dots-sensitized solar cells. *Sol. Energy Mater. Sol. Cells* **2020**, *206*, 110307. [[CrossRef](#)]
287. Shen, X.; Jia, J.; Lin, Y.; Zhou, X. Enhanced performance of CdTe quantum dot sensitized solar cell via anion exchanges. *J. Power Sources* **2015**, *277*, 215–221. [[CrossRef](#)]

288. Pan, Z.; Mora-Seró, I.; Shen, Q.; Zhang, H.; Li, Y.; Zhao, K.; Bisquert, J. High-efficiency “green” quantum dot solar cells. *J. Am. Chem. Soc.* **2014**, *136*, 9203–9210. [[CrossRef](#)]
289. McDaniel, H.; Fuke, N.; Makarov, N.S.; Pietryga, J.M.; Klimov, V.I. An integrated approach to realizing high-performance liquid-junction quantum dot sensitized solar cells. *Nat. Commun.* **2013**, *4*, 2887. [[CrossRef](#)]
290. Rao, H.; Zhou, M.; Pan, Z.; Zhong, X. Quantum dot materials engineering boosting the quantum dot sensitized solar cell efficiency over 13%. *J. Mater. Chem. A* **2020**, *8*, 10233–10241. [[CrossRef](#)]
291. Peng, W.; Du, J.; Pan, Z.; Nakazawa, N.; Sun, J.; Du, Z.; Zhong, X. Alloying strategy in Cu–In–Ga–Se quantum dots for high efficiency quantum dot sensitized solar cells. *ACS Appl. Mater. Interfaces* **2017**, *9*, 5328–5336. [[CrossRef](#)] [[PubMed](#)]
292. Bai, B.; Kou, D.; Zhou, W.; Zhou, Z.; Wu, S. Application of quaternary Cu₂ZnSnS₄ quantum dot-sensitized solar cells based on the hydrolysis approach. *Green Chem.* **2015**, *17*, 4377–4382. [[CrossRef](#)]
293. Kottayi, R.; Panneerselvam, P.; Singh, N.; Murugadoss, V.; Sittaramane, R.; Angaiah, S. Influence of a bifunctional linker on the loading of Cu₂AgInS₄ QDs onto porous TiO₂ NFs to use as an efficient photoanode to boost the photoconversion efficiency of QDSCs. *New J. Chem.* **2020**, *44*, 13148–13156. [[CrossRef](#)]
294. Song, H.; Lin, Y.; Zhou, M.; Rao, H.; Pan, Z.; Zhong, X. Zn–Cu–In–S–Se Quinary “Green” Alloyed Quantum-Dot-Sensitized Solar Cells with a Certified Efficiency of 14.4%. *Angew. Chem. Int. Ed.* **2021**, *60*, 6137–6144. [[CrossRef](#)] [[PubMed](#)]
295. Huang, P.; Xu, S.; Zhang, M.; Zhong, W.; Xiao, Z.; Luo, Y. Green allium fistulosum derived nitrogen self-doped carbon dots for quantum dot-sensitized solar cells. *Mater. Chem. Phys.* **2020**, *240*, 122158. [[CrossRef](#)]
296. Boyd, C.C.; Cheacharoen, R.; Leijtens, T.; McGehee, M.D. Understanding degradation mechanisms and improving stability of perovskite photovoltaics. *Chem. Rev.* **2018**, *119*, 3418–3451. [[CrossRef](#)]
297. Kari, M.; Saghafi, K. Current-voltage hysteresis reduction of CH₃NH₃PbI₃ planar perovskite solar cell by multi-layer absorber. *Micro Nanostruct.* **2022**, *165*, 207207. [[CrossRef](#)]
298. Lin, Z. Relationship between ion vacancy mobility and hysteresis of perovskite solar cells. *Chem. Phys.* **2022**, *554*, 111422. [[CrossRef](#)]
299. Wu, F.; Pathak, R.; Qiao, Q. Origin and alleviation of JV hysteresis in perovskite solar cells: A short review. *Catal. Today* **2021**, *374*, 86–101. [[CrossRef](#)]
300. Zhou, Y.; Luo, X.; Yang, J.; Qiu, Q.; Xie, T.; Liang, T. Application of quantum dot interface modification layer in perovskite solar cells: Progress and perspectives. *Nanomaterials* **2022**, *12*, 2102. [[CrossRef](#)] [[PubMed](#)]
301. Ye, M.; Biesold, G.M.; Zhang, M.; Wang, W.; Bai, T.; Lin, Z. Multifunctional quantum dot materials for perovskite solar cells: Charge transport, efficiency and stability. *Nano Today* **2021**, *40*, 101286. [[CrossRef](#)]
302. Zheng, F.; Liu, Y.; Ren, W.; Sunli, Z.; Xie, X.; Cui, Y.; Hao, Y. Application of quantum dots in perovskite solar cells. *Nanotechnology* **2021**, *32*, 482003. [[CrossRef](#)] [[PubMed](#)]
303. Jin, J.; Chen, C.; Li, H.; Cheng, Y.; Xu, L.; Dong, B.; Dai, Q. Enhanced performance and photostability of perovskite solar cells by introduction of fluorescent carbon dots. *ACS Appl. Mater. Interfaces* **2017**, *9*, 14518–14524. [[CrossRef](#)]
304. Li, H.; Shi, W.; Huang, W.; Yao, E.P.; Han, J.; Chen, Z.; Yang, Y. Carbon quantum dots/TiO_x electron transport layer boosts efficiency of planar heterojunction perovskite solar cells to 19%. *Nano Lett.* **2017**, *17*, 2328–2335. [[CrossRef](#)]
305. Zhu, X.; Sun, J.; Yuan, S.; Li, N.; Qiu, Z.; Jia, J.; Cao, B. Efficient and stable planar perovskite solar cells with carbon quantum dots-doped PCBM electron transport layer. *New J. Chem.* **2019**, *43*, 7130–7135. [[CrossRef](#)]
306. Chen, J.; Dong, H.; Zhang, L.; Li, J.; Jia, F.; Jiao, B.; Wu, Z. Graphitic carbon nitride doped SnO₂ enabling efficient perovskite solar cells with PCEs exceeding 22%. *J. Mater. Chem. A* **2020**, *8*, 2644–2653. [[CrossRef](#)]
307. Hui, W.; Yang, Y.; Xu, Q.; Gu, H.; Feng, S.; Su, Z.; Huang, W. Red-carbon-quantum-dot-doped SnO₂ composite with enhanced electron mobility for efficient and stable perovskite solar cells. *Adv. Mater.* **2020**, *32*, 1906374. [[CrossRef](#)]
308. Nagaraj, G.; Mohammed, M.K.; Shekargoftar, M.; Sasikumar, P.; Sakthivel, P.; Ravi, G.; Shalan, A.E. High-performance perovskite solar cells using the graphene quantum dot–modified SnO₂/ZnO photoelectrode. *Mater. Today Energy* **2021**, *22*, 100853. [[CrossRef](#)]
309. Xie, J.; Huang, K.; Yu, X.; Yang, Z.; Xiao, K.; Qiang, Y.; Yang, D. Enhanced electronic properties of SnO₂ via electron transfer from graphene quantum dots for efficient perovskite solar cells. *ACS Nano* **2017**, *11*, 9176–9182. [[CrossRef](#)]
310. Lu, C.; Zhang, W.; Jiang, Z.; Zhang, Y.; Ni, C. Graphene quantum dots doping SnO₂ for improving carrier transport of perovskite solar cells. *Ceram. Int.* **2021**, *47*, 29712–29721. [[CrossRef](#)]
311. Ebrahimi, M.; Kermanpur, A.; Atapour, M.; Adhami, S.; Heidari, R.H.; Khorshidi, E.; Rezaie, B. Performance enhancement of mesoscopic perovskite solar cells with GQDs-doped TiO₂ electron transport layer. *Sol. Energy Mater. Sol. Cells* **2020**, *208*, 110407. [[CrossRef](#)]
312. Yang, Z.; Xie, J.; Arivazhagan, V.; Xiao, K.; Qiang, Y.; Huang, K.; Yang, D. Efficient and highly light stable planar perovskite solar cells with graphene quantum dots doped PCBM electron transport layer. *Nano Energy* **2017**, *40*, 345–351. [[CrossRef](#)]
313. Pang, S.; Zhang, C.; Zhang, H.; Dong, H.; Chen, D.; Zhu, W.; Hao, Y. Boosting performance of perovskite solar cells with Graphene quantum dots decorated SnO₂ electron transport layers. *Appl. Surf. Sci.* **2020**, *507*, 145099. [[CrossRef](#)]
314. Shen, D.; Zhang, W.; Xie, F.; Li, Y.; Abate, A.; Wei, M. Graphene quantum dots decorated TiO₂ mesoporous film as an efficient electron transport layer for high-performance perovskite solar cells. *J. Power Sources* **2018**, *402*, 320–326. [[CrossRef](#)]
315. Zhou, Y.; Yang, S.; Yin, X.; Han, J.; Tai, M.; Zhao, X.; Lin, H. Enhancing electron transport via graphene quantum dot/SnO₂ composites for efficient and durable flexible perovskite photovoltaics. *J. Mater. Chem. A* **2019**, *7*, 1878–1888. [[CrossRef](#)]

316. Zeng, X.; Zhou, T.; Leng, C.; Zang, Z.; Wang, M.; Hu, W.; Zhou, M. Performance improvement of perovskite solar cells by employing a CdSe quantum dot/PCBM composite as an electron transport layer. *J. Mater. Chem. A* **2017**, *5*, 17499–17505. [[CrossRef](#)]
317. Ali, S.M.; Ramay, S.M.; Aziz, M.H.; AlGarawi, M.S.; AlGhamd, S.S.; Mahmood, A.; Atiq, S. Efficiency enhancement of perovskite solar cells by incorporation of CdS quantum dot through fast electron injection. *Org. Electron.* **2018**, *62*, 21–25. [[CrossRef](#)]
318. Kumnorkaew, P.; Rattanawichai, N.; Ratanatawanate, C.; Yoriya, S.; Lohawet, K.; Zhao, Y.; Vas-Umnuay, P. Influence of PbS quantum dots-doped TiO₂ nanotubes in TiO₂ film as an electron transport layer for enhanced perovskite solar cell performance. *IEEE J. Photovolt.* **2019**, *10*, 287–295. [[CrossRef](#)]
319. Pang, Z.; Yang, S.; Sun, Y.; He, L.; Wang, F.; Fan, L.; Yang, J. Hydrophobic PbS QDs layer decorated ZnO electron transport layer to boost photovoltaic performance of perovskite solar cells. *Chem. Eng. J.* **2022**, *439*, 135701. [[CrossRef](#)]
320. Zhang, Y.; Xu, L.; Wu, Y.; Zhou, Q.; Shi, Z.; Zhuang, X.; Song, H. Double-layer synergistic optimization by functional black phosphorus quantum dots for high-efficiency and stable planar perovskite solar cells. *Nano Energy* **2021**, *90*, 106610. [[CrossRef](#)]
321. Gu, B.; Du, Y.; Chen, B.; Zhao, R.; Lu, H.; Xu, Q.; Guo, C. Black Phosphorus Quantum Dot-Engineered Tin Oxide Electron Transport Layer for Highly Stable Perovskite Solar Cells with Negligible Hysteresis. *ACS Appl. Mater. Interfaces* **2022**, *14*, 11264–11272. [[CrossRef](#)]
322. Zhou, J.; Lyu, M.; Zhu, J.; Li, G.; Li, Y.; Jin, S.; Zhou, R. SnO₂ Quantum Dot-Modified Mesoporous TiO₂ Electron Transport Layer for Efficient and Stable Perovskite Solar Cells. *ACS Appl. Energy Mater.* **2022**, *5*, 3052–3063. [[CrossRef](#)]
323. Liu, J.; Dong, Q.; Wang, M.; Ma, H.; Pei, M.; Bian, J.; Shi, Y. Efficient Planar Perovskite Solar Cells with Carbon Quantum Dot-Modified Spiro-MeOTAD as a Composite Hole Transport Layer. *ACS Appl. Mater. Interfaces* **2021**, *13*, 56265–56272. [[CrossRef](#)]
324. Benetti, D.; Jokar, E.; Yu, C.H.; Fathi, A.; Zhao, H.; Vomiero, A.; Rosei, F. Hole-extraction and photostability enhancement in highly efficient inverted perovskite solar cells through carbon dot-based hybrid material. *Nano Energy* **2019**, *62*, 781–790. [[CrossRef](#)]
325. Kim, J.K.; Nguyen, D.N.; Lee, J.H.; Kang, S.; Kim, Y.; Kim, S.S.; Kim, H.K. Carbon quantum dot-incorporated nickel oxide for planar pin type perovskite solar cells with enhanced efficiency and stability. *J. Alloys Compd.* **2020**, *818*, 152887. [[CrossRef](#)]
326. Li, W.; Cheng, N.; Cao, Y.; Zhao, Z.; Xiao, Z.; Zi, W.; Sun, Z. Boost the performance of inverted perovskite solar cells with PEDOT: PSS/graphene quantum dots composite hole transporting layer. *Org. Electron.* **2020**, *78*, 105575. [[CrossRef](#)]
327. Wang, Z.; Rong, X.; Wang, L.; Wang, W.; Lin, H.; Li, X. Dual role of amino-functionalized graphene quantum dots in NiO_x films for efficient inverted flexible perovskite solar cells. *ACS Appl. Mater. Interfaces* **2020**, *12*, 8342–8350. [[CrossRef](#)]
328. Zhang, X.; Wang, Q.; Jin, Z.; Chen, Y.; Liu, H.; Wang, J.; Liu, S. Graphdiyne quantum dots for much improved stability and efficiency of perovskite solar cells. *Adv. Mater. Interfaces* **2018**, *5*, 1701117. [[CrossRef](#)]
329. Xiao, J.; Shi, J.; Liu, H.; Xu, Y.; Lv, S.; Luo, Y.; Li, Y. Efficient CH₃NH₃PbI₃ perovskite solar cells based on graphdiyne (GD)-modified P3HT hole-transporting material. *Adv. Energy Mater.* **2015**, *5*, 1401943. [[CrossRef](#)]
330. Zheng, J.; Li, F.; Chen, C.; Du, Q.; Jin, M.; Li, H.; Shen, Z. Perovskite Solar Cells Employing a PbSO₄ (PbO)₄ Quantum Dot-Doped Spiro-OMeTAD Hole Transport Layer with an Efficiency over 22%. *ACS Appl. Mater. Interfaces* **2022**, *14*, 2989–2999. [[CrossRef](#)]
331. Ameen, S.; Akhtar, M.S.; Seo, H.K.; Nazeeruddin, M.K.; Shin, H.S. An insight into atmospheric plasma jet modified ZnO quantum dots thin film for flexible perovskite solar cell: Optoelectronic transient and charge trapping studies. *J. Phys. Chem. C* **2015**, *119*, 10379–10390. [[CrossRef](#)]
332. Tavakoli, M.M.; Tavakoli, R.; Nourbakhsh, Z.; Waleed, A.; Virk, U.S.; Fan, Z. High efficiency and stable perovskite solar cell using ZnO/rGO QDs as an electron transfer layer. *Adv. Mater. Interfaces* **2016**, *3*, 1500790. [[CrossRef](#)]
333. Tu, Y.; Wu, J.; Zheng, M.; Huo, J.; Zhou, P.; Lan, Z.; Huang, M. TiO₂ quantum dots as superb compact block layers for high-performance CH₃NH₃PbI₃ perovskite solar cells with an efficiency of 16.97%. *Nanoscale* **2015**, *7*, 20539–20546. [[CrossRef](#)] [[PubMed](#)]
334. Wang, E.; Chen, P.; Yin, X.; Wu, Y.; Que, W. Novel ethanol vapor annealing treatment of SnO₂ quantum dots film for highly efficient planar heterojunction perovskite solar cells. *Org. Electron.* **2020**, *84*, 105751. [[CrossRef](#)]
335. Liu, H.; Chen, Z.; Wang, H.; Ye, F.; Ma, J.; Zheng, X.; Fang, G. A facile room temperature solution synthesis of SnO₂ quantum dots for perovskite solar cells. *J. Mater. Chem. A* **2019**, *7*, 10636–10643. [[CrossRef](#)]
336. Wang, E.; Chen, P.; Yin, X.; Wu, Y.; Que, W. Tailoring electronic properties of SnO₂ quantum dots via aluminum addition for high-efficiency perovskite solar cells. *Sol. RRL* **2019**, *3*, 1900041. [[CrossRef](#)]
337. Yang, G.; Chen, C.; Yao, F.; Chen, Z.; Zhang, Q.; Zheng, X.; Fang, G. Effective carrier-concentration tuning of SnO₂ quantum dot electron-selective layers for high-performance planar perovskite solar cells. *Adv. Mater.* **2018**, *30*, 1706023. [[CrossRef](#)]
338. Park, S.Y.; Baek, M.Y.; Ju, Y.; Kim, D.H.; Moon, C.S.; Noh, J.H.; Jung, H.S. Simultaneous ligand exchange fabrication of flexible perovskite solar cells using newly synthesized uniform tin oxide quantum dots. *J. Phys. Chem. Lett.* **2018**, *9*, 5460–5467. [[CrossRef](#)]
339. Vijayaraghavan, S.N.; Wall, J.; Li, L.; Xing, G.; Zhang, Q.; Yan, F. Low-temperature processed highly efficient hole transport layer free carbon-based planar perovskite solar cells with SnO₂ quantum dot electron transport layer. *Mater. Today Phys.* **2020**, *13*, 100204. [[CrossRef](#)]
340. Fu, N.; Huang, C.; Lin, P.; Zhu, M.; Li, T.; Ye, M.; Ke, S. Black phosphorus quantum dots as dual-functional electron-selective materials for efficient plastic perovskite solar cells. *J. Mater. Chem. A* **2018**, *6*, 8886–8894. [[CrossRef](#)]
341. Hu, L.; Wang, W.; Liu, H.; Peng, J.; Cao, H.; Shao, G.; Tang, J. PbS colloidal quantum dots as an effective hole transporter for planar heterojunction perovskite solar cells. *J. Mater. Chem. A* **2015**, *3*, 515–518. [[CrossRef](#)]

342. Li, Y.; Zhu, J.; Huang, Y.; Wei, J.; Liu, F.; Shao, Z.; Dai, S. Efficient inorganic solid solar cells composed of perovskite and PbS quantum dots. *Nanoscale* **2015**, *7*, 9902–9907. [[CrossRef](#)] [[PubMed](#)]
343. Paulo, S.; Stoica, G.; Cambarau, W.; Martinez-Ferrero, E.; Palomares, E. Carbon quantum dots as new hole transport material for perovskite solar cells. *Synth. Met.* **2016**, *222*, 17–22. [[CrossRef](#)]
344. Zhao, G.; Cai, Q.; Liu, X.; Li, P.; Zhang, Y.; Shao, G.; Liang, C. PbS QDs as electron blocking layer toward efficient and stable perovskite solar cells. *IEEE J. Photovolt.* **2018**, *9*, 194–199. [[CrossRef](#)]
345. Majdi, M.; Eskandari, M.; Fathi, D. Textured HTM-free perovskite/PbS quantum dot solar cell: Optical and electrical efficiency improvement by light trapping control. *Sol. Energy* **2021**, *230*, 618–627. [[CrossRef](#)]
346. Lv, M.; Zhu, J.; Huang, Y.; Li, Y.; Shao, Z.; Xu, Y.; Dai, S. Colloidal CuInS₂ quantum dots as inorganic hole-transporting material in perovskite solar cells. *ACS Appl. Mater. Interfaces* **2015**, *7*, 17482–17488. [[CrossRef](#)]
347. Kim, J.Y.; Baek, W.; Kim, S.; Kang, G.; Han, I.K.; Hyeon, T.; Park, M. Moisture proof hole transport layers based on CISE quantum dots for highly stable and large active area perovskite solar cells. *Appl. Surf. Sci.* **2019**, *496*, 143610. [[CrossRef](#)]
348. Zhang, Y.; Zhang, Z.; Liu, Y.; Liu, Y.; Gao, H.; Mao, Y. An inorganic hole-transport material of CuInSe₂ for stable and efficient perovskite solar cells. *Org. Electron.* **2019**, *67*, 168–174. [[CrossRef](#)]
349. Li, Y.; Wang, Z.; Ren, D.; Liu, Y.; Zheng, A.; Zakeeruddin, S.M.; Dong, X.; Hagfeldt, A.; Grätzel, M.; Wang, P. SnS quantum dots as hole transporter of perovskite solar cells. *ACS Appl. Energy Mater.* **2019**, *2*, 3822–3829. [[CrossRef](#)]
350. Duan, J.; Dou, D.; Zhao, Y.; Wang, Y.; Yang, X.; Yuan, H.; Tang, Q. Spray-assisted deposition of CsPbBr₃ films in ambient air for large-area inorganic perovskite solar cells. *Mater. Today Energy* **2018**, *10*, 146–152. [[CrossRef](#)]
351. Liu, C.; Zhou, X.; Chen, S.; Zhao, X.; Dai, S.; Xu, B. Hydrophobic Cu₂O Quantum Dots Enabled by Surfactant Modification as Top Hole-Transport Materials for Efficient Perovskite Solar Cells. *Adv. Sci.* **2019**, *6*, 1801169. [[CrossRef](#)]
352. Zhao, Y.; Duan, J.; Yuan, H.; Wang, Y.; Yang, X.; He, B.; Tang, Q. Using SnO₂ QDs and CsMBr₃ (M = Sn, Bi, Cu) QDs as charge-transporting materials for 10.6%-efficiency all-inorganic CsPbBr₃ perovskite solar cells with an ultrahigh open-circuit voltage of 1.610 V. *Sol. RRL* **2019**, *3*, 1800284. [[CrossRef](#)]
353. Li, F.; Wei, J.; Liao, G.; Guo, C.; Huang, Y.; Zhang, Q.; Li, Q. Quaternary quantum dots with gradient valence band for all-inorganic perovskite solar cells. *J. Colloid Interface Sci.* **2019**, *549*, 33–41. [[CrossRef](#)] [[PubMed](#)]
354. Liu, Y.; Chen, Q.; Mei, A.; Hu, B.; Yang, Z.; Chen, W. Bandgap aligned Cu₁₂Sb₄S₁₃ quantum dots as efficient inorganic hole transport materials in planar perovskite solar cells with enhanced stability. *Sustain. Energy Fuels* **2019**, *3*, 831–840. [[CrossRef](#)]
355. Liu, Y.; Zhao, X.; Yang, Z.; Li, Q.; Wei, W.; Hu, B.; Chen, W. Cu₁₂Sb₄S₁₃ quantum dots with ligand exchange as hole transport materials in all-inorganic perovskite CsPbI₃ quantum dot solar cells. *ACS Appl. Energy Mater.* **2020**, *3*, 3521–3529. [[CrossRef](#)]
356. Tamilselvan, M.; Bhattacharyya, A.J. Tetrahedrite (Cu₁₂Sb₄S₁₃) ternary inorganic hole conductor for ambient processed stable Perovskite solar cells. *ACS Appl. Energy Mater.* **2018**, *1*, 4227–4234. [[CrossRef](#)]
357. Wu, Q.; Xue, C.; Li, Y.; Zhou, P.; Liu, W.; Zhu, J.; Yang, S. Kesterite Cu₂ZnSnS₄ as a low-cost inorganic hole-transporting material for high-efficiency perovskite solar cells. *ACS Appl. Mater. Interfaces* **2015**, *7*, 28466–28473. [[CrossRef](#)]
358. Zhou, Z.J.; Deng, Y.Q.; Zhang, P.P.; Kou, D.X.; Zhou, W.H.; Meng, Y.N.; Wu, S.X. Cu₂ZnSnS₄ Quantum Dots as Hole Transport Material for Enhanced Charge Extraction and Stability in All-Inorganic CsPbBr₃ Perovskite Solar Cells. *Sol. RRL* **2019**, *3*, 1800354. [[CrossRef](#)]
359. Khanzada, L.S.; Levchuk, I.; Hou, Y.; Azimi, H.; Osvet, A.; Ahmad, R.; Brabec, C.J. Effective ligand engineering of the Cu₂ZnSnS₄ nanocrystal surface for increasing hole transport efficiency in perovskite solar cells. *Adv. Funct. Mater.* **2016**, *26*, 8300–8306. [[CrossRef](#)]
360. Yuan, M.; Zhang, X.; Kong, J.; Zhou, W.; Zhou, Z.; Tian, Q.; Kou, D. Controlling the band gap to improve open-circuit voltage in metal chalcogenide based perovskite solar cells. *Electrochim. Acta* **2016**, *215*, 374–379. [[CrossRef](#)]
361. Xu, L.; Deng, L.L.; Cao, J.; Wang, X.; Chen, W.Y.; Jiang, Z. Solution-processed Cu (In, Ga)(S, Se)₂ nanocrystal as inorganic hole-transporting material for efficient and stable perovskite solar cells. *Nanoscale Res. Lett.* **2017**, *12*, 159. [[CrossRef](#)] [[PubMed](#)]
362. Xu, H.; Duan, J.; Zhao, Y.; Jiao, Z.; He, B.; Tang, Q. 9.13%-Efficiency and stable inorganic CsPbBr₃ solar cells. Lead-free CsSnBr₃-xI_x quantum dots promote charge extraction. *J. Power Sources* **2018**, *399*, 76–82. [[CrossRef](#)]
363. Im, J.H.; Lee, C.R.; Lee, J.W.; Park, S.W.; Park, N.G. 6.5% efficient perovskite quantum-dot-sensitized solar cell. *Nanoscale* **2011**, *3*, 4088–4093. [[CrossRef](#)]
364. Bang, J.H.; Kamat, P.V. Quantum dot sensitized solar cells. A tale of two semiconductor nanocrystals: CdSe and CdTe. *ACS Nano* **2009**, *3*, 1467–1476. [[CrossRef](#)]
365. González-Pedro, V.; Xu, X.; Mora-Sero, I.; Bisquert, J. Modeling high-efficiency quantum dot sensitized solar cells. *ACS Nano* **2010**, *4*, 5783–5790. [[CrossRef](#)]
366. Yao, Y.; Hang, P.; Li, B.; Hu, Z.; Kan, C.; Xie, J.; Yu, X. Phase-Stable Wide-Bandgap Perovskites for Four-Terminal Perovskite/Silicon Tandem Solar Cells with over 30% Efficiency. *Small* **2022**, *18*, 2203319. [[CrossRef](#)]
367. De Vos, A. Detailed balance limit of the efficiency of tandem solar cells. *J. Phys. D Appl. Phys.* **1980**, *13*, 839. [[CrossRef](#)]
368. Wali, Q.; Elumalai, N.K.; Iqbal, Y.; Uddin, A.; Jose, R. Tandem perovskite solar cells. *Renew. Sustain. Energy Rev.* **2018**, *84*, 89–110. [[CrossRef](#)]
369. Yao, M.; Cong, S.; Arab, S.; Huang, N.; Povinelli, M.L.; Cronin, S.B.; Zhou, C. Tandem solar cells using GaAs nanowires on Si: Design, fabrication, and observation of voltage addition. *Nano Lett.* **2015**, *15*, 7217–7224. [[CrossRef](#)]

370. Saravanan, S.; Kato, R.; Balamurugan, M.; Kaushik, S.; Soga, T. Efficiency improvement in dye sensitized solar cells by the plasmonic effect of green synthesized silver nanoparticles. *J. Sci. Adv. Mater. Devices* **2017**, *2*, 418–424. [[CrossRef](#)]
371. Bedair, S.M.; Lamorte, M.F.; Hauser, J.R. A two-junction cascade solar-cell structure. *Appl. Phys. Lett.* **1979**, *34*, 38–39. [[CrossRef](#)]
372. Gao, Y.; Xu, S.; Liu, Z.; Yu, K.; Wang, C.; Wu, S.; Pan, X. Fluorescence enhanced microfluidic sensor with CsPbI₃ probe for lubricant copper ions on-site rapid detection based on SiO₂ inverse opal photonic crystals. *J. Lumin.* **2021**, *238*, 118276. [[CrossRef](#)]
373. Gnida, P.; Amin, M.F.; Pająk, A.K.; Jarzabek, B. Polymers in High-Efficiency Solar Cells: The Latest Reports. *Polymers* **2022**, *14*, 1946. [[CrossRef](#)]
374. You, J.; Dou, L.; Yoshimura, K.; Kato, T.; Ohya, K.; Moriarty, T.; Yang, Y. A polymer tandem solar cell with 10.6% power conversion efficiency. *Nat. Commun.* **2013**, *4*, 1446. [[CrossRef](#)] [[PubMed](#)]
375. Meng, L.; Zhang, Y.; Wan, X.; Li, C.; Zhang, X.; Wang, Y.; Chen, Y. Organic and solution-processed tandem solar cells with 17.3% efficiency. *Science* **2018**, *361*, 1094–1098. [[CrossRef](#)] [[PubMed](#)]
376. Ying, Z.; Zhu, Y.; Feng, X.; Xiu, J.; Zhang, R.; Ma, X.; He, Z. Sputtered Indium-Zinc Oxide for Buffer Layer Free Semitransparent Perovskite Photovoltaic Devices in Perovskite/Silicon 4T-Tandem Solar Cells. *Adv. Mater. Interfaces* **2021**, *8*, 2001604. [[CrossRef](#)]
377. Chen, B.; Baek, S.W.; Hou, Y.; Aydin, E.; De Bastiani, M.; Scheffel, B.; Sargent, E.H. Enhanced optical path and electron diffusion length enable high-efficiency perovskite tandems. *Nat. Commun.* **2020**, *11*, 1257. [[CrossRef](#)]
378. Park, I.J.; Park, J.H.; Ji, S.G.; Park, M.A.; Jang, J.H.; Kim, J.Y. A three-terminal monolithic perovskite/Si tandem solar cell characterization platform. *Joule* **2019**, *3*, 807–818. [[CrossRef](#)]
379. Chen, B.; Wang, P.; Li, R.; Ren, N.; Chen, Y.; Han, W.; Zhang, X. Composite electron transport layer for efficient nip type monolithic perovskite/silicon tandem solar cells with high open-circuit voltage. *J. Energy Chem.* **2021**, *63*, 461–467. [[CrossRef](#)]
380. Aydin, E.; Liu, J.; Ugur, E.; Azmi, R.; Harrison, G.T.; Hou, Y.; De Wolf, S. Ligand-bridged charge extraction and enhanced quantum efficiency enable efficient n-i-p perovskite/silicon tandem solar cells. *Energy Environ. Sci.* **2021**, *14*, 4377–4390. [[CrossRef](#)]
381. Lamanna, E.; Matteocci, F.; Calabrò, E.; Serenelli, L.; Salza, E.; Martini, L.; di Carlo, A. Mechanically stacked, two-terminal graphene-based perovskite/silicon tandem solar cell with efficiency over 26%. *Joule* **2020**, *4*, 865–881. [[CrossRef](#)]
382. Chen, B.; Zhengshan, J.Y.; Manzoor, S.; Wang, S.; Weigand, W.; Yu, Z.; Huang, J. Blade-coated perovskites on textured silicon for 26%-efficient monolithic perovskite/silicon tandem solar cells. *Joule* **2020**, *4*, 850–864. [[CrossRef](#)]
383. Khan, A.D.; Subhan, F.E.; Khan, A.D.; Khan, S.D.; Ahmad, M.S.; Rehan, M.S.; Noman, M. Optimization of efficient monolithic perovskite/silicon tandem solar cell. *Optik* **2020**, *208*, 164573.
384. Abbasiyan, A.; Noori, M.; Baghban, H. Quasi-periodic selective intermediate structure for perovskite/Si tandem solar cells. *Sol. Energy* **2020**, *198*, 461–468. [[CrossRef](#)]
385. Park, H.H.; Kim, J.; Kim, G.; Jung, H.; Kim, S.; Moon, C.S.; Seo, J. Transparent Electrodes Consisting of a Surface-Treated Buffer Layer Based on Tungsten Oxide for Semitransparent Perovskite Solar Cells and Four-Terminal Tandem Applications. *Small Methods* **2020**, *4*, 2000074. [[CrossRef](#)]
386. Tockhorn, P.; Wagner, P.; Kegelmann, L.; Stang, J.C.; Mews, M.; Albrecht, S.; Korte, L. Three-terminal perovskite/silicon tandem solar cells with top and interdigitated rear contacts. *ACS Appl. Energy Mater.* **2020**, *3*, 1381–1392. [[CrossRef](#)]
387. Xu, J.; Boyd, C.C.; Yu, Z.J.; Palmstrom, A.F.; Witter, D.J.; Larson, B.W.; McGehee, M.D. Triple-halide wide-band gap perovskites with suppressed phase segregation for efficient tandems. *Science* **2020**, *367*, 1097–1104. [[CrossRef](#)]
388. Mazzarella, L.; Lin, Y.H.; Kirner, S.; Morales-Vilches, A.B.; Korte, L.; Albrecht, S.; Schlattmann, R. Infrared light management using a nanocrystalline silicon oxide interlayer in monolithic perovskite/silicon heterojunction tandem solar cells with efficiency above 25%. *Adv. Energy Mater.* **2019**, *9*, 1803241. [[CrossRef](#)]
389. Ramírez Quiroz, C.O.; Spyropoulos, G.D.; Salvador, M.; Roch, L.M.; Berlinghof, M.; Darío Perea, J.; Brabec, C.J. Interface molecular engineering for laminated monolithic perovskite/silicon tandem solar cells with 80.4% fill factor. *Adv. Funct. Mater.* **2019**, *29*, 1901476. [[CrossRef](#)]
390. Sampaio, P.; González, M. A review on organic photovoltaic cell. *Int. J. Energy Res.* **2022**, *46*, 17813–17828. [[CrossRef](#)]
391. Liu, Q.; Jiang, Y.; Jin, K.; Qin, J.; Xu, J.; Li, W.; Ding, L. 18% Efficiency organic solar cells. *Sci. Bull.* **2020**, *65*, 272–275. [[CrossRef](#)] [[PubMed](#)]
392. Li, C.; Zhou, J.; Song, J.; Xu, J.; Zhang, H.; Zhang, X.; Sun, Y. Non-fullerene acceptors with branched side chains and improved molecular packing to exceed 18% efficiency in organic solar cells. *Nat. Energy* **2021**, *6*, 605–613. [[CrossRef](#)]
393. Liang, Y.; Xu, Z.; Xia, J.; Tsai, S.T.; Wu, Y.; Li, G.; Yu, L. For the bright future—Bulk heterojunction polymer solar cells with power conversion efficiency of 7.4%. *Adv. Mater.* **2010**, *22*, E135–E138. [[CrossRef](#)]
394. Rafique, S.; Abdullah, S.M.; Sulaiman, K.; Iwamoto, M. Fundamentals of bulk heterojunction organic solar cells: An overview of stability/degradation issues and strategies for improvement. *Renew. Sustain. Energy Rev.* **2018**, *84*, 43–53. [[CrossRef](#)]
395. Riede, M.; Spoltore, D.; Leo, K. Organic solar cells—The path to commercial success. *Adv. Energy Mater.* **2021**, *11*, 2002653. [[CrossRef](#)]
396. Ahmad, Z.; Najeeb, M.A.; Shakoor, R.A.; Al-Muhtaseb, S.A.; Touati, F. Limits and possible solutions in quantum dot organic solar cells. *Renew. Sustain. Energy Rev.* **2018**, *82*, 1551–1564. [[CrossRef](#)]
397. Kumavat, P.P.; Sonar, P.; Dalal, D.S. An overview on basics of organic and dye sensitized solar cells, their mechanism and recent improvements. *Renew. Sustain. Energy Rev.* **2017**, *78*, 1262–1287. [[CrossRef](#)]
398. Zhao, J.; Li, Y.; Yang, G.; Jiang, K.; Lin, H.; Ade, H.; Yan, H. Efficient organic solar cells processed from hydrocarbon solvents. *Nat. Energy* **2016**, *1*, 15027. [[CrossRef](#)]

399. Zhang, Z.; Yuan, J.; Wei, Q.; Zou, Y. Small-molecule electron acceptors for efficient non-fullerene organic solar cells. *Front. Chem.* **2018**, *6*, 414. [[CrossRef](#)] [[PubMed](#)]
400. Kesavan, A.V.; Kumar, M.P.; Rao, A.D.; Ramamurthy, P.C. Light management through up-conversion and scattering mechanism of rare earth nanoparticle in polymer photovoltaics. *Opt. Mater.* **2019**, *94*, 286–293. [[CrossRef](#)]
401. Yang, C.; Zhao, C.; Sun, Y.; Li, Q.; Islam, M.R.; Liu, K.; Wang, Z. Optical management in organic photovoltaic devices. *Carbon Energy* **2021**, *3*, 4–23. [[CrossRef](#)]
402. Nam, Y.M.; Huh, J.; Jo, W.H. Optimization of thickness and morphology of active layer for high performance of bulk-heterojunction organic solar cells. *Sol. Energy Mater. Sol. Cells* **2010**, *94*, 1118–1124. [[CrossRef](#)]
403. Ulum, M.S.; Sesa, E.; Belcher, W. The effect of active layer thickness on P3HT: PCBM nanoparticulate organic photovoltaic device performance. *J. Phys. Conf. Ser.* **2019**, *1242*, 012025. [[CrossRef](#)]
404. Ho CH, Y.; Kothari, J.; Fu, X.; So, F. Interconnecting layers for tandem organic solar cells. *Mater. Today Energy* **2021**, *21*, 100707.
405. Gusain, A.; Faria, R.M.; Miranda, P.B. Polymer solar cells—Interfacial processes related to performance issues. *Front. Chem.* **2019**, *7*, 61. [[CrossRef](#)]
406. Colladet, K.; Nicolas, M.; Goris, L.; Lutsen, L.; Vanderzande, D. Low-band gap polymers for photovoltaic applications. *Thin Solid Film.* **2004**, *451*, 7–11. [[CrossRef](#)]
407. Dhanabalan, A.; van Duren, J.K.; van Hal, P.A.; van Dongen, J.L.; Janssen, R.A.J. Synthesis and characterization of a low bandgap conjugated polymer for bulk heterojunction photovoltaic cells. *Adv. Funct. Mater.* **2001**, *11*, 255–262. [[CrossRef](#)]
408. Liang, Y.; Wu, Y.; Feng, D.; Tsai, S.T.; Son, H.J.; Li, G.; Yu, L. Development of new semiconducting polymers for high performance solar cells. *J. Am. Chem. Soc.* **2009**, *131*, 56–57. [[CrossRef](#)] [[PubMed](#)]
409. Lin, Y.; Wang, J.; Zhang, Z.G.; Bai, H.; Li, Y.; Zhu, D.; Zhan, X. An electron acceptor challenging fullerenes for efficient polymer solar cells. *Adv. Mater.* **2015**, *27*, 1170–1174. [[CrossRef](#)] [[PubMed](#)]
410. Zhao, W.; Li, S.; Yao, H.; Zhang, S.; Zhang, Y.; Yang, B.; Hou, J. Molecular optimization enables over 13% efficiency in organic solar cells. *J. Am. Chem. Soc.* **2017**, *139*, 7148–7151. [[CrossRef](#)] [[PubMed](#)]
411. Yuan, J.; Zhang, Y.; Zhou, L.; Zhang, G.; Yip, H.L.; Lau, T.K.; Zou, Y. Single-junction organic solar cell with over 15% efficiency using fused-ring acceptor with electron-deficient core. *Joule* **2019**, *3*, 1140–1151. [[CrossRef](#)]
412. Zhang, Y.; Ji, Y.; Zhang, Y.; Zhang, W.; Bai, H.; Du, M.; Zhou, E. Recent Progress of Y6-Derived Asymmetric Fused Ring Electron Acceptors. *Adv. Funct. Mater.* **2022**, *32*, 2205115. [[CrossRef](#)]
413. Sun, R.; Wu, Y.; Yang, X.; Gao, Y.; Chen, Z.; Li, K.; Min, J. Single-Junction Organic Solar Cells with 19.17% Efficiency Enabled by Introducing One Asymmetric Guest Acceptor. *Adv. Mater.* **2022**, *34*, 2110147. [[CrossRef](#)]
414. Chong, K.; Xu, X.; Meng, H.; Xue, J.; Yu, L.; Ma, W.; Peng, Q. Realizing 19.05% efficiency polymer solar cells by progressively improving charge extraction and suppressing charge recombination. *Adv. Mater.* **2022**, *34*, 2109516. [[CrossRef](#)]
415. Kamel, M.S.; Al-Jumaili, A.; Oelgemöller, M.; Jacob, M.V. Inorganic nanoparticles to overcome efficiency inhibitors of organic photovoltaics: An in-depth review. *Renew. Sustain. Energy Rev.* **2022**, *166*, 112661. [[CrossRef](#)]
416. Smets, A.H.; Jäger, K.; Isabella, O.; Swaaij, R.A.; Zeman, M. *Solar Energy: The Physics and Engineering of Photovoltaic Conversion, Technologies and Systems*; UIT Cambridge: Cambridge, UK, 2015.
417. Xu, W.; Li, X.; Jeong, S.Y.; Son, J.H.; Zhou, Z.; Jiang, Q.; Zhang, F. Achieving 17.5% efficiency for polymer solar cells via a donor and acceptor layered optimization strategy. *J. Mater. Chem. C* **2022**, *10*, 5489–5496. [[CrossRef](#)]
418. Xue, R.; Zhang, J.; Li, Y.; Li, Y. Organic solar cell materials toward commercialization. *Small* **2018**, *14*, 1801793. [[CrossRef](#)]
419. Zhao, W.; Qian, D.; Zhang, S.; Li, S.; Inganäs, O.; Gao, F.; Hou, J. Fullerene-free polymer solar cells with over 11% efficiency and excellent thermal stability. *Adv. Mater.* **2016**, *28*, 4734–4739. [[CrossRef](#)] [[PubMed](#)]
420. Xu, X.; Yu, T.; Bi, Z.; Ma, W.; Li, Y.; Peng, Q. Realizing over 13% efficiency in green-solvent-processed nonfullerene organic solar cells enabled by 1,3,4-thiadiazole-based wide-bandgap copolymers. *Adv. Mater.* **2018**, *30*, 1703973. [[CrossRef](#)] [[PubMed](#)]
421. Lin, Y.; Zhao, F.; He, Q.; Huo, L.; Wu, Y.; Parker, T.C.; Zhan, X. High-performance electron acceptor with thienyl side chains for organic photovoltaics. *J. Am. Chem. Soc.* **2016**, *138*, 4955–4961. [[CrossRef](#)] [[PubMed](#)]
422. Li, S.; Ye, L.; Zhao, W.; Zhang, S.; Mukherjee, S.; Ade, H.; Hou, J. Energy-level modulation of small-molecule electron acceptors to achieve over 12% efficiency in polymer solar cells. *Adv. Mater.* **2016**, *28*, 9423–9429. [[CrossRef](#)] [[PubMed](#)]
423. Wang, J.L.; Liu, K.K.; Hong, L.; Ge, G.Y.; Zhang, C.; Hou, J. Selenopheno [3, 2-b] thiophene-based narrow-bandgap nonfullerene acceptor enabling 13.3% efficiency for organic solar cells with thickness-insensitive feature. *ACS Energy Lett.* **2018**, *3*, 2967–2976. [[CrossRef](#)]
424. Lin, Y.; Zhao, F.; Prasad, S.K.; Chen, J.D.; Cai, W.; Zhang, Q.; Zhan, X. Balanced partnership between donor and acceptor components in nonfullerene organic solar cells with > 12% efficiency. *Adv. Mater.* **2018**, *30*, 1706363. [[CrossRef](#)]
425. Zhu, J.; Xiao, Y.; Wang, J.; Liu, K.; Jiang, H.; Lin, Y.; Zhan, X. Alkoxy-induced near-infrared sensitive electron acceptor for high-performance organic solar cells. *Chem. Mater.* **2018**, *30*, 4150–4156. [[CrossRef](#)]
426. Li, T.; Dai, S.; Ke, Z.; Yang, L.; Wang, J.; Yan, C.; Zhan, X. Fused Tris (thienothiophene)-Based Electron Acceptor with Strong Near-Infrared Absorption for High-Performance As-Cast Solar Cells. *Adv. Mater.* **2018**, *30*, 1705969. [[CrossRef](#)]
427. Tran, H.N.; Park, S.; Wibowo FT, A.; Krishna, N.V.; Kang, J.H.; Seo, J.H.; Cho, S. 17% Non-Fullerene Organic Solar Cells with Annealing-Free Aqueous MoO_x. *Adv. Sci.* **2020**, *7*, 2002395. [[CrossRef](#)]
428. Cui, Y.; Yao, H.; Zhang, J.; Zhang, T.; Wang, Y.; Hong, L.; Hou, J. Over 16% efficiency organic photovoltaic cells enabled by a chlorinated acceptor with increased open-circuit voltages. *Nat. Commun.* **2019**, *10*, 2515. [[CrossRef](#)]

429. Cui, Y.; Yao, H.; Zhang, J.; Xian, K.; Zhang, T.; Hong, L.; Hou, J. Single-junction organic photovoltaic cells with approaching 18% efficiency. *Adv. Mater.* **2020**, *32*, 1908205. [[CrossRef](#)] [[PubMed](#)]
430. Zhang, Z.; Li, Y.; Cai, G.; Zhang, Y.; Lu, X.; Lin, Y. Selenium heterocyclic electron acceptor with small Urbach energy for as-cast high-performance organic solar cells. *J. Am. Chem. Soc.* **2020**, *142*, 18741–18745. [[CrossRef](#)] [[PubMed](#)]
431. Chai, G.; Chang, Y.; Zhang, J.; Xu, X.; Yu, L.; Zou, X.; Yan, H. Fine-tuning of side-chain orientations on nonfullerene acceptors enables organic solar cells with 17.7% efficiency. *Energy Environ. Sci.* **2021**, *14*, 3469–3479. [[CrossRef](#)]
432. Yuan, J.; Huang, T.; Cheng, P.; Zou, Y.; Zhang, H.; Yang, J.L.; Yang, Y. Enabling low voltage losses and high photocurrent in fullerene-free organic photovoltaics. *Nat. Commun.* **2019**, *10*, 570. [[CrossRef](#)]
433. Song, J.; Zhu, L.; Li, C.; Xu, J.; Wu, H.; Zhang, X.; Sun, Y. High-efficiency organic solar cells with low voltage loss induced by solvent additive strategy. *Matter* **2021**, *4*, 2542–2552. [[CrossRef](#)]
434. Yu, G.; Gao, J.; Hummelen, J.C.; Wudl, F.; Heeger, A.J. Polymer photovoltaic cells: Enhanced efficiencies via a network of internal donor-acceptor heterojunctions. *Science* **1995**, *270*, 1789–1791. [[CrossRef](#)]
435. Shaheen, S.E.; Brabec, C.J.; Sariciftci, N.S.; Padinger, F.; Fromherz, T.; Hummelen, J.C. 2.5% efficient organic plastic solar cells. *Appl. Phys. Lett.* **2001**, *78*, 841–843. [[CrossRef](#)]
436. Zhang, S.; Qin, Y.; Zhu, J.; Hou, J. Over 14% efficiency in polymer solar cells enabled by a chlorinated polymer donor. *Adv. Mater.* **2018**, *30*, 1800868. [[CrossRef](#)]
437. Ma, R.; Liu, T.; Luo, Z.; Guo, Q.; Xiao, Y.; Chen, Y.; Yan, H. Improving open-circuit voltage by a chlorinated polymer donor endows binary organic solar cells efficiencies over 17%. *Sci. China Chem.* **2020**, *63*, 325–330. [[CrossRef](#)]
438. Cui, Y.; Yao, H.; Hong, L.; Zhang, T.; Xu, Y.; Xian, K.; Hou, J. Achieving over 15% efficiency in organic photovoltaic cells via copolymer design. *Adv. Mater.* **2019**, *31*, 1808356. [[CrossRef](#)]
439. Bin, H.; Zhang, Z.G.; Gao, L.; Chen, S.; Zhong, L.; Xue, L.; Li, Y. Non-fullerene polymer solar cells based on alkylthio and fluorine substituted 2D-conjugated polymers reach 9.5% efficiency. *J. Am. Chem. Soc.* **2016**, *138*, 4657–4664. [[CrossRef](#)] [[PubMed](#)]
440. Xue, L.; Yang, Y.; Xu, J.; Zhang, C.; Bin, H.; Zhang, Z.G.; Li, Y. Side chain engineering on medium bandgap copolymers to suppress triplet formation for high-efficiency polymer solar cells. *Adv. Mater.* **2017**, *29*, 1703344. [[CrossRef](#)] [[PubMed](#)]
441. Xiong, J.; Jin, K.; Jiang, Y.; Qin, J.; Wang, T.; Liu, J.; Ding, L. Thiolactone copolymer donor gifts organic solar cells a 16.72% efficiency. *Sci. Bull.* **2019**, *64*, 1573–1576. [[CrossRef](#)] [[PubMed](#)]
442. Jin, K.; Xiao, Z.; Ding, L. D18, an eximious solar polymer! *J. Semicond.* **2021**, *42*, 010502. [[CrossRef](#)]
443. Singh-Rachford, T.N.; Castellano, F.N. Photon upconversion based on sensitized triplet–triplet annihilation. *Coord. Chem. Rev.* **2010**, *254*, 2560–2573. [[CrossRef](#)]
444. Weingarten, D.H.; LaCount, M.D.; van de Lagemaat, J.; Rumbles, G.; Lusk, M.T.; Shaheen, S.E. Experimental demonstration of photon upconversion via cooperative energy pooling. *Nat. Commun.* **2017**, *8*, 14808. [[CrossRef](#)]
445. Moffatt, J.E.; Tsiminis, G.; Klantsataya, E.; de Prins, T.J.; Ottaway, D.; Spooner, N.A. A practical review of shorter than excitation wavelength light emission processes. *Appl. Spectrosc. Rev.* **2020**, *55*, 327–349. [[CrossRef](#)]
446. Bloembergen, N. Solid state infrared quantum counters. *Phys. Rev. Lett.* **1959**, *2*, 84. [[CrossRef](#)]
447. Auzel, F. Upconversion and anti-stokes processes with f and d ions in solids. *Chem. Rev.* **2004**, *104*, 139–174. [[CrossRef](#)]
448. Ye, H.; Bogdanov, V.; Liu, S.; Vajandar, S.; Osipowicz, T.; Hernandez, I.; Xiong, Q. Bright photon upconversion on composite organic lanthanide molecules through localized thermal radiation. *J. Phys. Chem. Lett.* **2017**, *8*, 5695–5699. [[CrossRef](#)]
449. Wang, J.; Ming, T.; Jin, Z.; Wang, J.; Sun, L.D.; Yan, C.H. Photon energy upconversion through thermal radiation with the power efficiency reaching 16%. *Nat. Commun.* **2014**, *5*, 5669. [[CrossRef](#)] [[PubMed](#)]
450. Raman, A.P.; Anoma, M.A.; Zhu, L.; Rephaeli, E.; Fan, S. Passive radiative cooling below ambient air temperature under direct sunlight. *Nature* **2014**, *515*, 540–544. [[CrossRef](#)]
451. Bünzli, J.C.G.; Chauvin, A.S. Lanthanides in solar energy conversion. In *Handbook on the Physics and Chemistry of Rare Earths*; Elsevier: Amsterdam, The Netherlands, 2014; Volume 44, pp. 169–281.
452. Zhang, Q.Y.; Huang, X.Y. Recent progress in quantum cutting phosphors. *Prog. Mater. Sci.* **2010**, *55*, 353–427. [[CrossRef](#)]
453. Dexter, D.L. Possibility of luminescent quantum yields greater than unity. *Phys. Rev.* **1957**, *108*, 630. [[CrossRef](#)]
454. Timmerman, D.; Izeddin, I.; Stallinga, P.; Yassievich, I.N.; Gregorkiewicz, T. Space-separated quantum cutting with silicon nanocrystals for photovoltaic applications. *Nat. Photonics* **2008**, *2*, 105–109. [[CrossRef](#)]
455. Ronda, C. Luminescent materials with quantum efficiency larger than 1, status and prospects. *J. Lumin.* **2002**, *100*, 301–305. [[CrossRef](#)]
456. Richards, B.S. Luminescent layers for enhanced silicon solar cell performance: Down-conversion. *Sol. Energy Mater. Sol. Cells* **2006**, *90*, 1189–1207. [[CrossRef](#)]
457. Huang, X.; Han, S.; Huang, W.; Liu, X. Enhancing solar cell efficiency: The search for luminescent materials as spectral converters. *Chem. Soc. Rev.* **2013**, *42*, 173–201. [[CrossRef](#)]
458. Ahmed, H.; McCormack, S.J.; Doran, J. External quantum efficiency improvement with luminescent downshifting layers: Experimental and modelling. *Int. J. Spectrosc.* **2016**, *2016*, 8543475. [[CrossRef](#)]
459. Green, M.A.; Bremner, S.P. Energy conversion approaches and materials for high-efficiency photovoltaics. *Nat. Mater.* **2017**, *16*, 23–34. [[CrossRef](#)]
460. Semonin, O.E.; Luther, J.M.; Choi, S.; Chen, H.Y.; Gao, J.; Nozik, A.J.; Beard, M.C. Peak external photocurrent quantum efficiency exceeding 100% via MEG in a quantum dot solar cell. *Science* **2011**, *334*, 1530–1533. [[CrossRef](#)]

461. De la Mora, M.B.; Amelines-Sarria, O.; Monroy, B.M.; Hernández-Pérez, C.D.; Lugo, J.E. Materials for downconversion in solar cells: Perspectives and challenges. *Sol. Energy Mater. Sol. Cells* **2017**, *165*, 59–71. [[CrossRef](#)]
462. Ehrler, B.; Wilson, M.W.; Rao, A.; Friend, R.H.; Greenham, N.C. Singlet exciton fission-sensitized infrared quantum dot solar cells. *Nano Lett.* **2012**, *12*, 1053–1057. [[CrossRef](#)] [[PubMed](#)]
463. Ross, R.T.; Nozik, A.J. Efficiency of hot-carrier solar energy converters. *J. Appl. Phys.* **1982**, *53*, 3813–3818. [[CrossRef](#)]
464. Hirst, L.C.; Lumb, M.P.; Hoheisel, R.; Bailey, C.G.; Philipps, S.P.; Bett, A.W.; Walters, R.J. Spectral sensitivity of hot carrier solar cells. *Sol. Energy Mater. Sol. Cells* **2014**, *120*, 610–615. [[CrossRef](#)]
465. Conibeer, G.; Shrestha, S.; Huang, S.; Patterson, R.; Xia, H.; Feng, Y.; Chung, S. Hot carrier solar cell absorber prerequisites and candidate material systems. *Sol. Energy Mater. Sol. Cells* **2015**, *135*, 124–129. [[CrossRef](#)]
466. Luque, A.; Martí, A. Increasing the efficiency of ideal solar cells by photon induced transitions at intermediate levels. *Phys. Rev. Lett.* **1997**, *78*, 5014. [[CrossRef](#)]
467. Ginley, D.; Okada, Y.; van-Sark, W.; Bett, A.; Glunz, S.; Gessert, T.; Frei, H. *Advanced Concepts in Photovoltaics*; Royal Society of Chemistry: London, UK, 2014.
468. Brown, A.S.; Green, M.A. Impurity photovoltaic effect: Fundamental energy conversion efficiency limits. *J. Appl. Phys.* **2002**, *92*, 1329–1336. [[CrossRef](#)]
469. Schaller, R.D.; Klimov, V.I. High efficiency carrier multiplication in PbSe nanocrystals: Implications for solar energy conversion. *Phys. Rev. Lett.* **2004**, *92*, 186601. [[CrossRef](#)]
470. Beard, M.C.; Knutsen, K.P.; Yu, P.; Luther, J.M.; Song, Q.; Metzger, W.K.; Nozik, A.J. Multiple exciton generation in colloidal silicon nanocrystals. *Nano Lett.* **2007**, *7*, 2506–2512. [[CrossRef](#)]
471. Stubbs, S.K.; Hardman, S.J.; Graham, D.M.; Spencer, B.F.; Flavell, W.R.; Glarvey, P.; Binks, D.J. Efficient carrier multiplication in InP nanoparticles. *Phys. Rev. B* **2010**, *81*, 081303. [[CrossRef](#)]
472. McGuire, J.A.; Sykora, M.; Joo, J.; Pietryga, J.M.; Klimov, V.I. Apparent versus true carrier multiplication yields in semiconductor nanocrystals. *Nano Lett.* **2010**, *10*, 2049–2057. [[CrossRef](#)]
473. Wang, S.; Khafizov, M.; Tu, X.; Zheng, M.; Krauss, T.D. Multiple exciton generation in single-walled carbon nanotubes. *Nano Lett.* **2010**, *10*, 2381–2386. [[CrossRef](#)] [[PubMed](#)]
474. Tielrooij, K.J.; Song, J.C.; Jensen, S.A.; Centeno, A.; Pesquera, A.; Zurutuza Elorza, A.; Koppens, F.H.L. Photoexcitation cascade and multiple hot-carrier generation in graphene. *Nat. Phys.* **2013**, *9*, 248–252. [[CrossRef](#)]
475. Congreve, D.N.; Lee, J.; Thompson, N.J.; Hontz, E.; Yost, S.R.; Reuswig, P.D.; Baldo, M.A. External quantum efficiency above 100% in a singlet-exciton-fission-based organic photovoltaic cell. *Science* **2013**, *340*, 334–337. [[CrossRef](#)] [[PubMed](#)]
476. Li, X.; Li, P.; Wu, Z.; Luo, D.; Yu, H.Y.; Lu, Z.H. Review and perspective of materials for flexible solar cells. *Mater. Rep. Energy* **2021**, *1*, 100001. [[CrossRef](#)]

Disclaimer/Publisher's Note: The statements, opinions and data contained in all publications are solely those of the individual author(s) and contributor(s) and not of MDPI and/or the editor(s). MDPI and/or the editor(s) disclaim responsibility for any injury to people or property resulting from any ideas, methods, instructions or products referred to in the content.